Macromolecule – Substrate Interactions in Directed Self-Assembly

From Tailored Block Copolymers with Polyferrocenylsilanes towards Functional Nanoplatforms

Monique Roerdink

Members of the committee:

Chairman	Prof. dr. J. F. J. Engbersen	Univ. of Twente
Secretary	Prof. dr. ir. A. Bliek	Univ. of Twente
Promotor	Prof. dr. G. J. Vancso	Univ. of Twente
Assistant-promotor	Dr. M. A. Hempenius	Univ. of Twente
Members	Prof. dr. J. Feijen	Univ. of Twente
	Prof. dr. ir. J. Huskens	Univ. of Twente
	Prof. dr. ing. M. Wessling	Univ. of Twente
	Prof. dr. R. P. Sijbesma	Techn. Univ. of Eindh.
	Prof. dr. U. Steiner	Univ. of Cambridge, UK

Macromolecule – Substrate Interactions in Directed Self-Assembly:
From Tailored Block Copolymers with Polyferrocenylsilanes towards
Functional Nanoplatforms

M. Roerdink
Ph. D. thesis
University of Twente, MESA$^+$ Institute for Nanotechnology,
Enschede, The Netherlands

This research was financially supported by the Netherlands Foundation for Chemical Research NWO-CW (project 700.51.021), and by NanoNed (project NI.TCP.6340), a national nanotechnology program coordinated by the Dutch Ministry of Economic Affairs.

ISBN: 978-90-365-2474-2

Printed by PrintPartners Ipskamp, Enschede, 2007.

Macromolecule - Substrate Interactions in Directed Self-Assembly:

From Tailored Block Copolymers with Polyferrocenylsilanes towards Functional Nanoplatforms

Proefschrift

ter verkrijging van de graad van doctor
aan de Universiteit Twente, op gezag van
de rector magnificus, prof. dr. W. H. M. Zijm,
volgens besluit van het College voor Promoties
in het openbaar te verdedigen op
donderdag 5 april 2007
om 15.00 uur

door

Monique Roerdink

geboren op 19 september 1979

te Groningen

Promotor:	Prof. dr. G. J. Vancso
Assistant-Promotor:	Dr. M. A. Hempenius

Vor der Natur gibt es kein Urteil; sie hat immer recht.

Rainer Maria Rilke

C'est véritablement utile puisque c'est joli.
(*It is truly useful, since it is beautiful.*)

From *Le Petit Prince* by Antoine de Saint Exupéry

Voor mijn ouders

Contents

CHAPTER 1

Introduction

Efforts in polymer science are increasingly directed at creating new functionality by design at the molecular level. New topics are emerging in polymer chemistry, such as supramolecular [1] and click chemistry, [2] and the importance of self-assembly in 'hybrid' block copolymers containing synthetic or natural peptide sequences, [3,4] will continue to grow.

The last two decades have seen block copolymers become a popular field of research. Synthetic routes to all sorts of well-defined, monodisperse architectures [5] became available, and simultaneously the theoretical understanding of phase segregation experienced major advances. [6–9] The self-assembling property of block copolymers and the enormous choice in blocks, shapes, lengths and so on have since earned block copolymers a place in nanotechnology, in nanostructure fabrication or patterning. [10–12] The abundance of block copolymers in nowadays 'hot topics' of nano- and bio-related research is illustrative of the potential of functional nanostructures in so-called 'bottom up' approaches.

Bottom-up self-assembly can be considered to be governed by the simple question '*how to get bigger?*'. Building blocks, in the form of atoms, molecules or aggregates of molecules, are available and can be manipulated almost at will at small scale, but one challenge is to extend their ordered assembly to larger dimensions.

The self-assembly on the scale of phase segregation of polymer chains into microdomains is now well-studied and has become a mature field in polymer science. However, if we move one step up the ladder of scale, we find self-assembly not on the molecular level, but on the level of the microdomains, presenting many new questions to be understood on a different scale. Interactions with the surroundings come into play, which are even more pronounced in thin films, and these govern the kinetics and thermodynamics of the mi-

crodomains. Which factors control the self-assembly of microdomains of a few tens of nanometers in size, resulting in the formation of ordered arrays over hundreds of nanometers, or even micrometers?

The work described in this thesis presents an effort to contribute to establishing what governs the order in self-assembled block copolymer systems, and even more important, how we can manipulate self-assembly.

1.1 Block copolymer self-assembly

The interest of scientists in block copolymers is described with an illustrating picture by Helfand and Wasserman: "Like a child contemplating the result of tying the cat's tail to that of a dog, scientists perhaps find a certain mischievous delight in considering the effect of joining two immiscible polymer blocks into one macromolecule. The immiscible units attempt to separate, but by the virtue of their connectivity they can never get very far from each other. The result is that they either segregate into microdomains or remain homogeneously mixed with each other".[13]

Phase-separated block copolymers microdomains have dimensions of 10 to 100 nm, depending on the molar mass of the polymer chains. A variety of shapes can be found, such as spheres, cylinders or lamellae, or micellar structures when prepared from solution. The phase-separated structures self-assemble into ordered arrays that provide a bottom-up approach to spontaneously formed nanometer-sized patterns. Microdomain phase separation is applicable to almost all block copolymers, providing a large choice in monomers and thus properties. Block copolymer self-assembly therefore constitutes a complementary approach to the conventional techniques of 'top-down' fabrication.

When thin films are cast from block copolymer solutions, with thicknesses close to the block copolymer repeat length, the domains order with respect to each other and the surfaces. For example, in a block copolymer with asymmetric volume fractions of the blocks, spherical domains of the minority component in a matrix of the majority block can be obtained. In a thin film these spherical domains will pack hexagonally. Such a film can be used as lithographic template[14–16] or as a nanoporous film or membrane.[17] Combined with the ease of processing polymers into thin films, the phase separated polymers are excellent candidates for producing nanopatterns over large areas in an easy and cost-effective way. Recently, an example of the utilization of self-assembled block copolymers was given by IBM, who used block copolymers to build a nanocrystal FLASH memory device.[18]

However, in order to be utilized in applications such as high-density data storage, the ordering of the domains needs to be controlled over large areas,

which remains one of the major challenges. Another challenge is the transfer of these patterns to a hard material, since most of the polymers consist of organic units, which gives few opportunities to transfer patterns by, for example, etching procedures. Typically, additional steps to 'load' an organic block copolymer with metals are necessary, since there are few examples of polymers containing inorganic elements.

1.2 PFS: A multi-functional polymer

There are many routes for preparing organic polymers with controlled architectures and molecular weights. This is not the case for polymers with inorganic elements in the main chain, although many interesting properties are to be anticipated from such polymers. One of the few examples that exist is poly(ferrocenylsilane) (PFS), which has a backbone consisting of alternating ferrocene and dialkylsilane units. The first example of high molar mass poly-(ferrocenylsilane) by thermal ring-opening polymerization was demonstrated by Manners and coworkers in the early '90s.[19] Upon heating, the highly strained silicon-bridged ferrocene monomers ring-open to form oligomeric and polymeric materials (Figure 1.1).

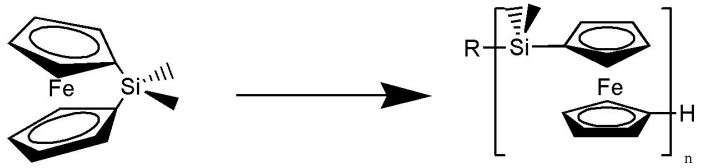

Figure 1.1: Ring-opening polymerization of [1]silaferrocenophane to poly(ferrocenylsilane).[19]

A major advance was made by the discovery that silaferrocenophanes can be polymerized anionically, providing routes to polymers with well-defined molar mass with narrow polydispersity and controlled chain architectures, such as block copolymers.[20,21] The organometallic polymers possess optical,[22] catalytic,[23,24] redox responsive[25,26] and etch resistant properties,[27,28] due to the presence of the early-transition metal in the main chain. Since then, thin films of PFS or block copolymers with PFS have been applied in the fabrication of redox responsive capsules,[29] in the formation of ceramic nanowires through micelle formation[30] and as templates in lithography to form dense arrays of cobalt dots for magnetic data storage.[16] Using PFS block copolymers, directed microdomain assembly has been demonstrated,[31] a feature highly important for use in applications as magnetic data storage.[32]

Thus, due to the organometallic character, PFS block copolymers combine the wide range of block copolymer applications with a diverse set of functionalities, which makes them highly interesting for fundamental studies, with applications near at hand.

1.3 Concept of the thesis

The research described in this thesis is concerned with exploring the controlled fabrication of patterned arrays at the nanoscale using poly(ferrocenylsilane) block copolymers. A fundamental understanding of the factors involved in directed self-assembly is pursued through the study of polymer-substrate interactions. An experimental approach was followed where polymers with properties tuned at specific substrate interactions were synthesized, characterized and applied in thin film studies.

The scope of the work presented in the thesis is given in *Chapter* 1. Some general concepts used throughout the chapters following are discussed in *Chapter* 2. The topics discussed in this chapter are brief on actual polymer concepts, such as phase separation, which are considered to be well-known. The physical background of ordered structures and techniques to probe these ordered structures are more extensively reviewed. The techniques are not new in themselves, but it is the combination of these techniques, which all probe specific aspects of order, that is important and which was found worthwhile to elaborate on.

Chapter 3 describes the synthesis and characterization of amorphous PFS and corresponding polyisoprene block copolymers. The thermal properties are discussed, as well as the bulk morphology and the order-disorder transition of the block copolymers. Block copolymers of polyisoprene and the amorphous PFS demonstrate remarkable ordering in thin films on flat substrates, which is the topic of *Chapter* 4. In addition, an extensive discussion on the wetting properties and the substrate directed morphology in supported films is given. *Chapter* 5 describes attempts to guide the ordering in thin films of these copolymers using 'graphoepitaxy', that is by means of topologically patterned substrates. Examples of two dimensional directed order on the micron scale are discussed, as well as the effect of different groove geometries on the alignment.

In the following *Chapter* 6, a novel block copolymer has been prepared and used in thin film studies, in an attempt to probe the influence of polymer-substrate interactions on ordering. The synthesis as well as the bulk and thin film characteristics of a PFS containing block copolymer with a polylactide block is described, which constitutes a more polar organic block compared to the polyisoprene and polystyrene blocks used throughout the previous chapters. *Chapter* 7 describes a more application-related study of the catalytic

properties of oxidized thin films of PFS block copolymers for the growth of carbon nanotubes with controlled diameters, tuned by the block copolymer domain sizes.

Finally, *Chapter* 8 treats the synthesis of amino-endfunctionalized PFS, which opens the possibility of incorporating specific motifs, such as hydrogen bond forming moieties, at the junction between two blocks. In addition, a more general outlook on the work presented in this thesis is given.

Bibliography

[1] Hazada, A. and Kataoke, K., *Prog. Polym. Sci.*, 2006, 31, 949-982.

[2] Ten Cate, A. T. and Sijbesma, R. P., *Macromol. Rapid Commun.*, 2002, 23, 1094-1112.

[3] *Peptide Hybrid Polymers*, Vol. 202 of *Adv. Polym. Sci.*, Klok, H. -A. and Schlaad, H., Eds., Springer-Verlag Berlin-Heidelberg, 2006.

[4] Gohy, J. -F., In *Block Copolymers II*, Vol. 190 of *Adv. Polym. Sci.*, 2005, 65-136.

[5] Hadjichristidus, N., Pitsikalis, M. and Iatrou, H., In *Block Copolymers I*, Vol. 189 of *Adv. Polym. Sci.*, 2005, 1-124.

[6] Leibler, L., *Macromolecules*, 1980, 13, 1602-1617.

[7] Bates, F. S. and Fredrickson, G. H., *Annu. Rev. Phys. Chem.*, 1990, 41, 525-557.

[8] Bates, F. S., Rosedale, J. H. and Fredrickson, G. H., *J. Chem. Phys.*, 1990, 92, 6255-6270.

[9] Bates, F. S. and Fredrickson, G. H., *Phys. Today*, 1999, 52, 32-38.

[10] Segalman, R. A., *Mater. Sci. Eng.*, 2005, R48, 191-226.

[11] Li, M., Coenjarts, C. A. and Ober, C. K., In *Block Copolymers II*, Vol. 190 of *Adv. Polym. Sci*, 2005, 183-226.

[12] Hillmyer, M. A. In *Block Copolymers II*, Vol. 190 of *Adv. Polym. Sci.*, 2005, 137-181.

[13] Helfand, E. and Wasserman, Z. R., In *Developements in Block Copolymers*, Vol. 1, 1982, 99-125.

[14] Park, M., Harrison, C., Chaikin, P. M., Register, R. A. and Adamson, D. H., *Science*, 1997, 276, 1401-1404.

[15] Li, R., Dapkus, P., Thompson, M., Jeong, W., Harrison, C. K., Chaikin, P. M., Register, R. A. and Adamson, D. H., *Appl. Phys. Lett.*, 2000, 76. 1689-1691.

[16] Cheng, J. Y., Ross, C. A., Chan, V. Z. -H., Thomas, E. L., Lammertink, R. G. H. and Vancso, G. J., *Adv. Mater.*, 2001, 13, 1174-1178.

[17] Thurn-Albrecht, T., Scotter, J., Kästle, G. A., Emley, N., Shibauchi, T., Krusin-Elbaum, L., Guarini, K. W., Black, C. T., Tuominen, M. T. and Russell, T. P., *Science*, 2000, 290, 2126-2129.

[18] http://domino.atson.ibm.com/comm/pr.nsf/pages/rsc.sa-iedm.html.

[19] Foucher, D. A., Tang, B. -Z. and Manners, I., *J. Am. Chem. Soc.*, 1992, 114, 6246-6248.

[20] Rulkens, R., Ni, Y. and Manners, I., *J. Am. Chem. Soc.*, 1994, 116, 12121-12122.

[21] Ni, Y., Rulkens, R. and Manners, I., *J. Am. Chem. Soc.*, 1996, 118, 4102-4114.

[22] Wang, X. S., Winnik, M. A., and Manners, I., In *Metal-containing and Metallosupramolecular Polymers and Materials*, Vol. 928 of *ACS Symp. Ser.*, 2006, 274-291.

[23] Hinderling, C., Keles, Y., Stöckli, T., Knapp, H. F., De los Arcos, T., Oelhafen, P, Korczagin, I., Hempenius, M. A., Vancso, G. J., Pugin, R. and Heinzelmann, H., *Adv. Mater.*, 2004, 16, 876-879.

[24] Lastella, S., Jung, Y. J., Yang, H. C., Vajtaj, R., Ajayan, P. M., Ryu, C. Y., Rider, D. A. and Manners, I., *J. Mater. Chem.*, 2004, 14, 1791-1794.

[25] Nguyen, M. T., Diaz, A. F., Dementev, V. V. and Pannell, K. H., *Chem. Mater.*, 1993, 5, 1389-1394.

[26] Rulkens, R., Lough, A., Manners, I., Lovelace, S., Grant, C. and Geigger, W., *J. Am. Chem. Soc.*, 1996, 118, 12683-12695.

[27] Lammertink, R. G. H., Hempenius, M. A., Chan, V. Z. -H., Thomas, E. L. and Vancso, G. J., *Chem. Mater.*, 2001, 13, 429-434.

[28] Korczagin, I., Lammertink, R. G. H., Hempenius, M. A., Golze, S. and Vancso, G. J. In *Ordered Polymeric Nanostructures at Surfaces*, Vol. 200 of *Adv. Polym. Sci.*, 2006, 91-117.

[29] Ma, Y., Dong, W. -F., Hempenius, M. A., Möwald, H. and Vancso, G. J., *Macromolecules*, 2006, 5, 724-729.

[30] Cao, L., Massey, J. A., Winnik, M. A., Manners, I., Rietmüller, S., Banhart, F., Spatz, J. P. and Möller, M., *Adv. Funct. Mater.*, 2003, 13, 271-276.

[31] Cheng, J. Y., Ross, C. A., Smith, H. I. and Vancso, G. J., *Appl. Phys. Lett.*, 2002, 81, 3657-3659.

[32] Ross, C. A., *Annu. Rev. Mater. Res.*, 2001, 31, 203-235.

CHAPTER 2

Ordered structures in phase separated block copolymers

This chapter gives theoretical background information that is considered useful for the discussions in the later chapters. A brief review of the relevant polymer properties is given, as well as a discussion on microphase separation in diblock copolymers. The main focus of the chapter is on reviewing order in phase separated block copolymers. To this purpose, a number of techniques that are used to probe specific aspects of order are discussed. These include the structure characterization techniques small-angle X-ray scattering and dynamic secondary ion mass spectrometry, as well as image analysis techniques that are used to quantify lateral order. The correlation between the information obtained by these techniques, and the relation between order in block copolymers in bulk and in thin films is addressed.

2.1 Introduction

Block copolymers consist of two or more blocks that are chemically distinct and typically immiscible. If both blocks are sufficiently long, the polymer retains the properties of both types of sequences, as found in the corresponding homopolymers. Block copolymers therefore find widespread application as compatibilizers, mechanical strength or elasticity modifiers, or as solubilizers or thickeners.[1] Owing to the incompatibility the blocks phase separate to form aggregates on microscopic scale. Uniform block lengths lead to regular structures such as lamellae, or spheres or cylinders of one phase in a matrix of the other. The length scales can be tuned by simply varying the molar mass of the individual blocks. Polymers with desired properties can be designed by the choice of the blocks (and accordingly the associated physical properties), and by tuning the block ratios, which determines the microdomain structure. The polymerization method determines the molar mass and the polydispersity index (pdi), which is the ratio between the weight average molar mass (M_w) and the number average molar mass (M_n).[2]

The blocks can have an amorphous or semi-crystalline character, depending on the regularity of the segments. Stereoirregularity leads to packing defects, which impede crystallization. If units are regular, crystallite growth through the formation of crystal unit cells occurs. In block copolymers the crystallization can be either restricted to the separate phases, or take place at larger length scales involving the whole block copolymer sample, depending on the mobility of the phases.[3–6] In semi-crystalline polymers, the temperature T_m associated with the crystal melting depends on the type of polymer, on the molar mass of the polymer, and on the thermal history and crystallization conditions. The equilibrium melting temperature $T_{m,0}$ associated with the melting of crystals with an 'infinite' length cannot be experimentally obtained. Experimental melting temperatures T_m are always lower than $T_{m,0}$ due to the the fact that large crystals are difficult to grow. Crystallization conditions and impurities determine the finite crystal size. By extrapolating the melting temperature of finite crystals at various crystallization temperatures the equilibrium melting temperature can be approached. The rate of crystallization increases at temperatures further away from $T_{m,0}$. The crystallization rate exhibits a maximum depending on the temperature. At the melting temperature, the crystallization rate is zero. With increasing undercooling, the driving force for crystallization increases. On the other hand, the decrease of chain mobility with decreasing temperature as the glass transition is approached inhibits the crystallization. In block copolymers, the phase separation confines the mobility and accordingly the formation of crystals. Crystallization of one phase in a block copolymer is therefore usually slower and the melting

temperature is lower compared to the corresponding homopolymer.

At decreasing temperature, the chain segments can not move cooperatively anymore and the segmental movements of the polymer backbones are impeded. The polymer is in its glassy state, and typically hard and stiff, but not necessarily brittle. Motion is restricted to vibrations and rotations of segments of side-groups or chain ends. The transition from the rubbery to the glassy phase occurs at the glass transition (T_g) temperature. Major changes in the mechanical properties are involved in amorphous polymers, as well as in semi-crystalline polymers where the transition contributes to the overall softening of the polymer.[2,7] The temperature at which the glass-rubber transition, as this transition is hence also termed, occurs is therefore a crucial characteristic of amorphous polymers, and the applications of polymers depend mostly on this parameter. The temperature of the glass transition depends on parameters like the chemical structure of the polymer, the molar mass, tacticity or pressure. Confinement of the polymer, in thin films[8,9] or in block copolymer microdomains, strongly affects the increase or decrease in the segmental mobility locally, depending on the mobility or rigidity of the imposed confinement.

2.2 Phase separation

The interaction between two polymers A and B is expressed by the Flory-Huggings equation (Eq. 2.1),[10–12] which describes the Gibbs free energy upon mixing ΔG_{mix}.[7]

$$\frac{\Delta G_{mix}}{RT} = \frac{\phi_A}{n_A} ln(\phi_A) + \frac{\phi_B}{n_B} ln(\phi_B) + \phi_A \phi_B \chi_{AB} \tag{2.1}$$

The first two terms on the right represent the configurational entropy of the system, governed by the volume fraction of the two polymers (ϕ_i) and the degree of polymerization of the polymers (n_i). The chain length dependence reflects the translational and configurational entropy. The third term on the right represents the enthalpic interaction defined by the composition and the Flory-Huggins segmental interaction parameter (χ_{AB}), reflecting the incompatibility of the two monomers A and B. The temperature-dependence of mixing consists of an enthalpic contribution, expressed as the inverse correlation of χ with temperature. The entropy contribution is mainly associated with an increase in translational entropy upon mixing, which is negligible for polymers with a high molar mass. Simple *van der Waals* forces between the segmental pairs are stronger between equal segments than between unlike pairs, except for rare cases of hydrogen bonding, dipole-dipole forces or spe-

cial donor-acceptor interactions. Therefore, most polymers are incompatible in the limit of large degrees of polymerizations since the enthalpy of mixing is unfavorable.

In block copolymers, the macroscopic phase separation is impeded by the covalent linkage between the two blocks. Phase separation occurs, but is restricted to the microscopic scale, forming aggregates of the phases as far as the block lengths permit the segregation.[13–15]

Additional parameters now need to be considered for the phase separation morphology. Interfacial tension, together with packing frustration due to chain stretching governs the ordered structure of the phases, and will be at a minimum for microdomains possessing interfaces of *constant mean curvature* (CMC).[16–19] The interfacial tension γ describes the increase in free energy per increase of interface area. Therefore, it can be directly related to the interaction parameter χ

$$\gamma = \chi \, kT \, \frac{N_I}{S} \tag{2.2}$$

where N_I represents the number of A-B interactions in the interface of area S. The interface volume equals $S\Delta$, where Δ is half of the interface thickness. The number of segments in the interface therefore equals

$$N_I = \frac{S\Delta}{\nu} \tag{2.3}$$

where ν is the segmental volume. The interfacial thickness depends on the conformations of the polymer molecules in the melt. Assuming random walk statistics and using a DeGennes scaling type analysis for the free energy expression for the interface, the expression for the interfacial thickness becomes

$$\Delta = \frac{a}{\sqrt{6}} \chi^{-0.5} \tag{2.4}$$

with segments of size a. The interfacial tension γ is therefore given by

$$\gamma = \frac{a}{\nu\sqrt{6}} \sqrt{\chi} \, kT \tag{2.5}$$

As one can realize from Eq. 2.4 and Eq. 2.5, a lower value of χ implies a lower surface tension, but also a thicker interface. An increase in interface area results in more unfavorable A-B interactions, but overall the gain in free energy upon a smaller interfacial tension compensates the enthalpic penalty of mixing. On the other hand, a sharper interface necessarily implies a larger loss in conformational entropy of the chains at the interface.

The above discussion emphasizes the importance of the interaction parameter. The relevant parameter describing the strength of phase separation is expressed by χN which is obtained from Eq. 2.1 by using the sum of the degrees of polymerization of blocks A and B (n_A and n_B). Weak segregation occurs for χN close to 10.5, while values of $\chi N \geq 100$ indicate strong segregation.[13–15,20] In between, the phase segregation is intermediate. The morphologies and phase transitions of diblock copolymer melts are typically represented in phase diagrams, in which the temperature dependent segregation strength (χN), expressing the enthalpy-entropy balance, is plotted versus the block copolymer composition (f_i).

Phase boundaries between the different morphologies as well as the boundary between an ordered morphology and the disordered melt depend on χN and the block ratio (see Figure 2.1). For a fixed block composition, an order-disorder transition (ODT) can take place upon increasing temperature. At the ODT, the enthalpic energy penalty is offset by the entropic energy gain of mixing. Order-order transitions from one morphology to another occur for fixed χN and denote the tuning of the morphology by the block ratio.

Theoretically, the existing morphologies at different parameter values can be calculated using the self-consistent field theory.[22] In the strong segregation limit the interfacial region is assumed to be narrow. In this regime the phase boundaries are solely dependent on the copolymer composition and no longer on the temperature. The chain conformations are stretched and domain spacings can be scaled as $\sim N^{2/3}$.[23] The assumption of a narrow interface is no longer valid at temperatures near the ODT ($\chi N < 12$) where mixing of the two blocks already takes place before eventual complete homogeneous mixing.[1] In this weak segregating regime local density fluctuations of the two components are the root of microphase segregation.[13] The fluctuations are the result of a competition between decreasing A-B contacts, thereby lowering the enthalpic term, and the resulting increase in the entropic penalty. In the strong segregation regime these fluctuations are negligible due to the negligible entropic contribution. If the local density fluctuations are positive, the enthalpic effects will eventually dominate the entropic effects upon decreasing the temperature, and the system will cross its spinodal point resulting in microphase separation.[7] This spinodal point is the point in the weak segregation region where the enthalpy is offset by the entropy, upon decreasing the temperature, and vice versa. The point where this spontaneous transition in enthalpy-entropy balance takes place is highly dependent on the composition.[24] In the weak segregation regime the domain spacings can be scaled as $\sim N^{1/2}$.[13]

An approach involving the numerical solution of self consistent field equations,[25] without using approximations such as the narrow interface approx-

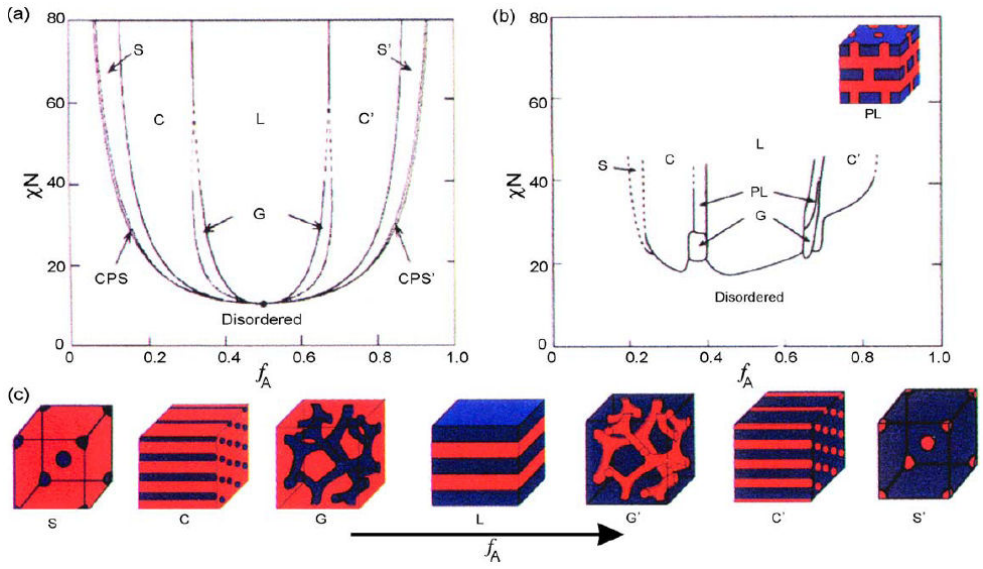

Figure 2.1: Diblock copolymers are predicted to self-assemble into four major equilibrium morphologies according to a phase diagram predicted by self-consistent mean field theory (a) which are proven experimentally (b). A variety of constant mean curvature geometries is observed as a function of relative lengths of the two blocks: spherical (S), cylindrical (C), gyroid (G), and lamellar (L) (c). CPS denotes closed-packed spheres, which are spheres packed in a face-centered cubic lattice. PL are perforated lamellae (inset in (b)). All phase transitions are thermodynamic first order transitions, except for the critical point which is a second order transition and marked by a dot in subfigure (a).[21]

imation, resulted in the possibility to calculate a complete phase diagram, shown in Figure 2.1.[21] More complex morphologies are possible in the case of conformational asymmetry,[16,24,26] such as the metastable perforated lamella,[26] shown in Figure 2.1b. Conformational asymmetry arises from either a difference in bulk density, or in Kuhn lengths, or both, and can stabilize complex morphologies.[24,26]

The intrinsic property of block copolymers to phase separate into nanosized domains that possess long range order opens up many possible applications,[27] for example as precursors for photonic crystals,[28] optical waveguides,[29] and nanoporous materials.[30]

2.3 Ordered structures: From bulk to thin films

The most common morphologies found in block copolymers are spheres in a body-centered cubic (BCC) lattice, hexagonally packed cylinders (HEX) or

lamellae (LAM). Closed packed spheres, organized in a face-centered cubic lattice (FCC), and gyroid structures also exist, but are rare. The microdomain morphology can be probed by several techniques, such as transmission electron microscopy, rheological measurements and small-angle X-ray scattering (SAXS). SAXS has the advantage that both the morphology and the lattice parameters can be determined accurately, macroscopically averaged. Further, only a small amount (about 10 mg) of material is needed, which is advantageous when the polymerizations are labor-intensive. In bulk the spherical domains are typically found to adopt a BCC packing, while in thin films stacked layers of in-plane hexagonally ordered domains are formed.[31–33] The in-plane order is typically short-ranged, extending over a small number of interdomain spacings, after which the directionality of the hexagonal packing is changed, which causes an in-plane overall appearance reminiscent of the grain structure found in metal films. The following sections describe techniques to probe the morphology of block copolymers in different situations, that is in the bulk (SAXS) and in films (by secondary ion mass spectrometry). Further, descriptives for in-plane order are discussed.

2.3.1 Bulk: Small-angle X-ray scattering

X-ray scattering probes the structure of a block copolymer averaged over a macroscopically sized sample. The scattering of X-rays is based upon a sufficient difference in electron density, in case of block copolymers between the different blocks. The X-rays are elastically scattered causing a diffraction pattern, which is the projection of the reciprocal lattice of the probed material. Diffraction from ordered structures is described by Bragg's law

$$\lambda = 2d_{hkl}\sin\theta \tag{2.6}$$

where λ is the wavelength, d_{hkl} is the spacing between allowed reflection planes given by their h, k and l Miller indices, and θ is the *glancing angle*, or half of the *scattering angle* 2θ.[34–36] From Eq. 2.6 it follows that for diffraction from electromagnetic radiation, λ must be smaller than twice the nearest neighbor distance, that is $\lambda \leq 2d_{hkl}$. The wavelength of X-rays is about 1 - 1.5 $\dot{A}$. Since the smallest spacing in block copolymers is typically about 20 - 30 nm, the angle at which the diffraction pattern is scattered is about $2\theta = 0.2°$ and upward, thus small-angle detection is necessary for determining block copolymer morphology.

The scattered data are represented as a function of the reciprocal scattering vector $\boldsymbol{q}$ or its magnitude $q = |\boldsymbol{q}|$

$$q = \frac{2\pi}{d_{hkl}} = \frac{4\pi \sin\theta}{\lambda} \tag{2.7}$$

The peak positions relative to the first Bragg peak unambiguously identify the morphology in the copolymer, since for each morphology there is a specific set of allowed reflections, that in combination with the lattice parameters result in the reciprocal peak positions.

The allowed reflections are determined by the structure factor F_{hkl}, which is the resultant of the scattered waves, differing in phase and scattered by all scattering centers of the unit cell.

$$F_{hkl} = \sum_j f_j \, e^{2\pi i(hx_j + ky_j + lz_j)} \tag{2.8}$$

The fractionate coordinates x_j, y_j and z_j represent the positions of all j atoms (in crystals) or domains (in block copolymers) in the unit cell along the three axes and f_j is the scattering factor of the corresponding scattering center. For example, the fractional coordinates for a BCC unit cell are 000 and $\frac{1}{2}\frac{1}{2}\frac{1}{2}$ and Eq. 2.8 results in

$$\begin{aligned} F_{hkl} &= 2f_j \qquad \text{for (h+k+l) = even} \\ F_{hkl} &= 0 \qquad \text{for (h+k+l) = odd} \end{aligned} \tag{2.9}$$

The allowed reflections for a BCC morphology are therefore (110), (200), (211), (220) and so forth. Figure 2.2 shows three possible diffraction planes (100), (110) and (111) in a BCC unit cell. However, from Eq. 2.9, it follows that the first allowed reflection in scattering is the (110) plane, which gives the d-spacing corresponding to the distance between the depicted planes. Scattering from the (100) and (111) planes shown in Figure 2.2 is not allowed. Similarly, the reflection conditions for an FCC lattice can be obtained from Eq. 2.8 and result in allowed reflections for unmixed h, k and l (*all* even or *all* odd) and extinction for mixed h, k and l. Simple cubic, hexagonal and lamellar morphology do not have forbidden reflections.

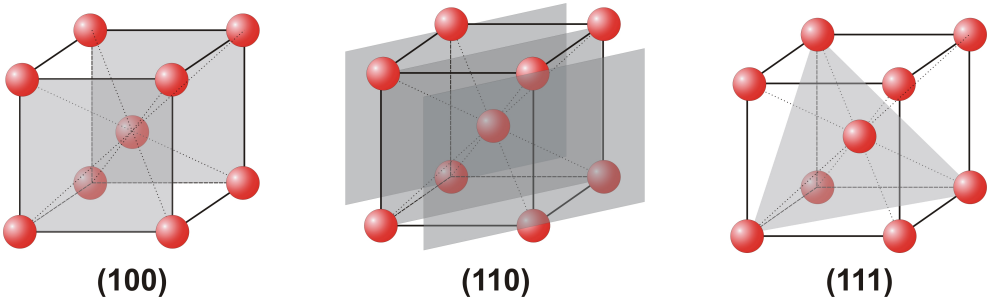

Figure 2.2: The (100), (110) and (111) planes in a BCC structure. The first allowed reflection is by the (110) planes.

The allowed reflections result in a scattering pattern typical of a specific lattice geometry. The distances between the reflecting planes for the three most common block copolymer lattices BCC, HEX and LAM are given by Eq. 2.10, 2.11 and 2.12, respectively.

$$\text{BCC:} \quad \frac{1}{d^2} = \frac{h^2+k^2+l^2}{a^2} \tag{2.10}$$

$$\text{HEX:} \quad \frac{1}{d^2} = \frac{4}{3}\left(\frac{h^2+hk+k^2}{a^2}\right)\frac{l^2}{c^2} \tag{2.11}$$

$$\text{LAM:} \quad \frac{1}{d^2} = \frac{h^2}{a^2} \tag{2.12}$$

Combining the above equations with Bragg's law (Eq. 2.6) results in expressions that relate the integral sum s of the Miller indices to the scattering angle q.

Table 2.1 lists the allowed reflecting planes for cubic, hexagonal and lamellar morphology, as well as s. The relative peak positions pos^* are given by

$$pos^* = \sqrt{\frac{s_{hkl}}{s_{1^{st}\,\text{refl}}}} \tag{2.13}$$

The higher order peak positions in q-space are at relative position to the first allowed reflection ($s_{1^{st}\,\text{refl}}$) and given by Eq. 2.13. The relative peak positions for the most common block copolymer morphologies of spheres in BCC (for comparison the simple cubic (SC) and FCC are given as well), hexagonally packed cylinders and lamellae are listed in Table 2.1. Identification of the bulk morphology in a block copolymer is possible if the discriminating higher order diffraction peaks are present. The d obtained for the first maximum can

Table 2.1: Allowed reflecting planes and the relative peak positions (pos^*) for morphologies of block copolymers. Ref.[34] was used to construct this table.

	Cubic						**HEX**^{b}		**LAM**^{c}	
	SC^a		**FCC**^{a}		**BCC**^{a}					
s	hkl	pos^*	hkl	pos^*	hkl	pos^*	hk	pos^*	h	pos^*
1	100^d	1					10^d	1	1^d	1
2	110	$\sqrt{2}$	-		110^d	1				
3	111	$\sqrt{3}$	111^d	1	-		11	$\sqrt{3}$		
4	200	$\sqrt{4}$	200	$\sqrt{\frac{4}{3}}$	200	$\sqrt{2}$	20	$\sqrt{4}$	2	2
5	210	$\sqrt{5}$								
6	211	$\sqrt{6}$	-		211	$\sqrt{3}$				
7							21	$\sqrt{7}$		
8	220	$\sqrt{8}$	220	$\sqrt{\frac{8}{3}}$	220	$\sqrt{4}$				
9	300, 221	3					30	3	3	3
10	310	$\sqrt{10}$	-		310	$\sqrt{5}$				
11	311	$\sqrt{11}$	311	$\sqrt{\frac{11}{3}}$	-					
12	222	$\sqrt{12}$	222	$\sqrt{4}$	222	$\sqrt{6}$	22	$\sqrt{10}$		
13	320	$\sqrt{13}$					31	$\sqrt{13}$		
14	321	$\sqrt{14}$	-		321	$\sqrt{7}$				
15										
16	400	4	400	$\sqrt{\frac{16}{3}}$	400	$\sqrt{8}$	40	4	4	4

^{a} $s = h^2 + k^2 + l^2$. ^{b} $s = h^2 + hk + k^2$. ^{c} $s = h^2$. ^{d} First allowed reflection. The '-' represents forbidden reflections.

be related to the center-to-center distance p by Eq. 2.6 and the geometrical relations Eq. 2.14.

$$\begin{aligned} \text{BCC:} \quad p &= \frac{1}{2}\sqrt{2}\sqrt{3}\,d \\ \text{HEX:} \quad p &= \frac{2d}{\sqrt{3}} \end{aligned} \tag{2.14}$$

2.3.2 Supported films: Dynamic time-of-flight secondary ion mass spectrometry

Dynamic secondary ion mass spectrometry (SIMS)[37–39] is a surface analysis technique used to gain information on the elemental composition in the depth

of materials. A surface is bombarded with primary ions (typically ions from Ar, Ga, Cs or O_2), causing secondary ions (as atoms, molecules or fragments of molecules) to be emitted by the material. The secondary ions are detected according to their charge-to-mass ratio (m/z) by mass spectrometry. SIMS has a high sensitivity to all elements, and is isotope sensitive, allowing ppm to ppb level detection. Further, the technique has a high depth resolution of less than 1 nm. The emitted ions can have different kinetic energies, which causes ions with the same m/z ratio to have different velocities, resulting in a loss of mass resolution. This natural spread is overcome in time-of-flight SIMS (TOF-SIMS) by the acceleration of the secondary ions to a constant kinetic energy. The time-of-flight of the secondary ion masses is measured. The advantage of TOF mass spectrometry in SIMS is the access to a wide mass range, parallel detection of all masses, and high mass resolution. Figure 2.3 shows a typical TOF-SIMS setup.

TOF-SIMS can be carried out in a static or dynamic mode. In static TOF-SIMS, typically low ion beam intensities are used and the mass spectrum is measured before a significant part of the surface layer has been chemically modified or sputtered away. In dynamic TOF-SIMS, higher primary ion beam intensities are used. The surface is etched away layer by layer, typically rastered over a distance several times the beam focal width, forming a flat bottomed crater. In between the etching steps, analysis of the sputtered area is done in a separate step, by bombarding with a low intensity, non-destructive analysis beam and registering the secondary ions generated, that is by static TOF-SIMS. In this way, a depth profile is created. The analysis is performed typically over a small area in the middle of the crater, to avoid crater-edge contributions. The intensities in TOF-SIMS are influenced by many factors, such as the chemical environment, the concentration of implanted primary ions and sample charging during sputtering. In particular on insulating substrates, such as silicon oxide, charging becomes more pronounced. The instrumentation is therefore equipped with a separate electron gun, to stabilize charges built-up at the surface during the measurement. Typically, in case of electropositive elements, intensity yields can be enhanced by flooding with a low dose of oxygen. TOF-SIMS has been used to study segregation phenomena in metal alloys as well as polymer blends, absorption layers, depth profiling in block copolymer thin films and diffusion studies in polymer films.[40–44]

The microdomains in a phase separated block copolymer are stacked most commonly in a BCC packing.[31] In case of a parallel orientation of an arbitrary plane of the morphology with respect to the two interfaces imposed by the substrate and the free surface, depth profiling with dynamic TOF-SIMS should result in an oscillating signal, provided that there is a composition difference between the two phases. The spacing between the maxima in the dynamic

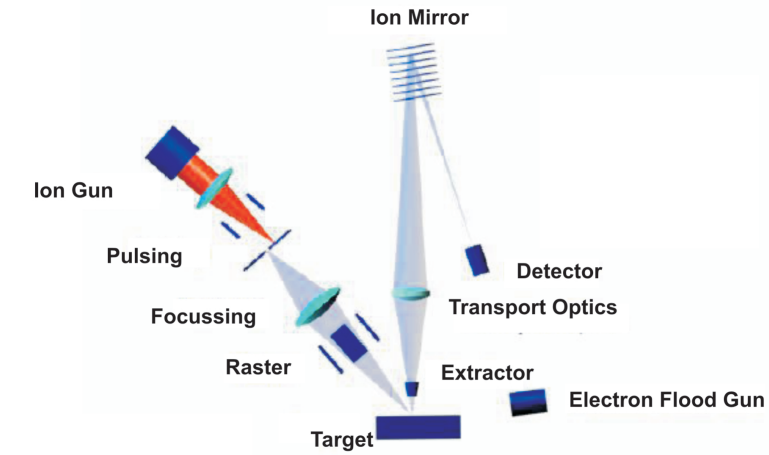

A

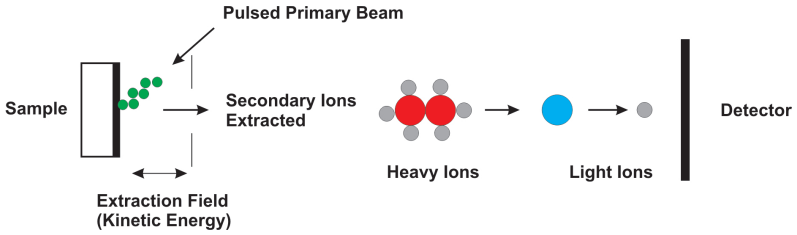

B

Figure 2.3: A) TOF-SIMS setup and B) Schematic representation of the TOF-SIMS principle. Figure A was adopted from ION-TOF GmbH.

TOF-SIMS depth profile relates to the corresponding d_{hkl} spacing of the BCC structure. For instance, if the (110) plane is parallel to the substrate and surface throughout the entire film, the distance between two peaks is the $d_{(110)}$ spacing (see Figure 2.4). In addition, this spacing is the the first allowed reflection peak measured by SAXS.

Thus, applied to block copolymers dynamic TOF-SIMS depth profiling can be used to determine which of the phases is at the air-polymer interface and which is at the polymer-substrate interface. The orientation of the lattice planes with respect to the surfaces can be determined as well.

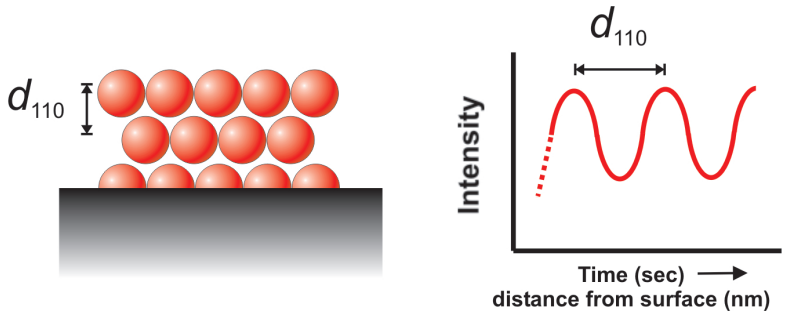

Figure 2.4: Planes of microdomains oriented parallel to the substrate and surface. In this illustration, the (110) plane is oriented in-plane. A corresponding dynamic TOF-SIMS depth profile gives an oscillating intensity signal, from which $d_{(110)}$ can be obtained.

2.3.3 Lateral morphology

Phase-separated block copolymer domains pack in the bulk to form ordered structures, that can be described by lattices, and probed by techniques such as X-ray scattering. In films, the presence of the substrate-polymer and the polymer-surface interfaces (the latter denotes the free interface) imposes constraints to the bulk structure, influencing the morphology. For instance, microdomains generally adopt a BCC packing in the bulk, while in a film of one layer of domains a hexagonal packing is adopted.[31] Obtaining an ordered morphology in block copolymers depends on the extent of the kinetic and thermodynamic equilibrium that has been achieved. This means that thin film morphologies are influenced by annealing time, annealing temperature, the substrate-block copolymer interaction, the block copolymer-air interaction, the strength of phase segregation and the method of film preparation. As the aim of this thesis is to understand and manipulate the organization of block copolymer microdomains in thin films, descriptives to quantify lateral order, based on image analysis, are described in the following section.

Atomic Force Microscopy

Structural studies based on electron microscopy and X-ray scattering were the dominant techniques to study block copolymer morphology, until studies on surface morphology became feasible with the development of two techniques: low-voltage high-resolution scanning electron microscopy (LVHR-SEM)[45] and atomic force microscopy (AFM). In AFM, a sharp stylus tip attached to a cantilever is scanned over a surface, while feedback ensures a constant tip-sample interaction. Lateral changes cause a deflection of the cantilever, which can be

translated into the surface contour. Several modes of operation are possible (friction, constant force, constant probe-surface), depending on the settings of the feedback electronics. In these *static* modes, the cantilever is scanned relative to the sample and typically in direct contact with the material. *Dynamic* oscillatory AFM techniques were introduced in addition to contact mode in AFM to study surfaces and mechanical properties of soft materials, by reducing tip-sample force interactions.[46] In tapping mode AFM (TM-AFM), an oscillating probe makes intermittent contact with a sample, and the associated change in the amplitude of oscillation is used for the feedback control.

In phase mode, the phase lag of the cantilever oscillation, relative to the signal sent to the cantilever piezo driver, is monitored simultaneously with the topographic response. The phase lag is mainly due to the interaction between the sample and the tip. Although the precise origin of the phase difference is unknown, it is demonstrated to depend on the sample properties such as viscoelasticity and stiffness.[46,47] The tip tends to remain longer in contact with softer material, leading to a larger phase lag compared to harder material.[47] In many cases phase images exhibit a higher contrast than height images do, revealing features related to surface composition that are not easily observed in height images.[46] Phase contrast AFM is therefore very suitable for morphology studies in block copolymer films, when there is a contrast in stiffness or viscoelasticity between the two phases.

In block copolymer surface morphology studies, there are still plenty of causes that can frustrate phase imaging by AFM. For instance, there can be little or no difference in energy dissipating properties between the two blocks. The majority phase can cover the surface, which screens the minority phase from the AFM probe. The imaging can be aided by using mild reactive ion etching in conjunction with AFM by etching the covering layer away, or by creating a height difference caused by a difference in etch rate between the block copolymer phases.[48–51]

Voronoi diagrams

Voronoi diagrams give a 2 or 3 dimensional graphical representation of the spatial distribution of any set of points in a defined space. The spatial distribution is represented by the formation of polyhedrons, in which each point is enclosed in such a way that it is closer to the center-of-mass of the polyhedron enclosing it than to any other. A Voronoi construction can therefore be employed to establish the degree of order more quantitatively, and aids in the visualization of packing defects and grain boundaries occurring in for example block copolymer thin films. Voronoi diagrams can be constructed by drawing straight lines between the center of an arbitrarily chosen center-of-mass

and all other nearby center-of-masses and drawing planes bisecting the lines perpendicularly (see Figure 2.5). The convex polyhedrons formed around the spheres are called Voronoi polyhedrons.

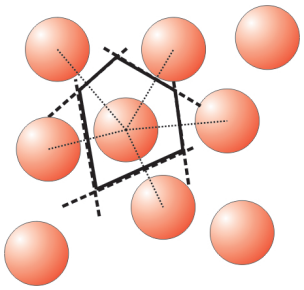

Figure 2.5: Construction of a Voronoi polyhedron. Lines at half distances to the centers between one sphere and its nearest neighbors (dotted lines) are drawn, which are then intersected by perpendicular planes (dashed lines). The set of planes closest to the central sphere form the Voronoi polyhedron (black lines).

The packing of block copolymer spheres in a lateral plane can be evaluated by analyzing the geometry of the set of polyhedra. Spheres surrounded by 6 neighbors appear as hexagons while 5- and 7-fold-coordinated sites are displayed as pentagons and heptagons, respectively. In addition to the number of neighbors, the reciprocal distances influence the shape of the Voronoi diagrams. For instance, drawing Voronoi diagrams of hexagonally packed spheres as in a thin film results in an array of hexagons. Similarly, hexagons will be obtained for a Voronoi analysis of the packing in a BCC (110) plane. However, the packing of domains in the (110) plane is a distorted hexagonal packing, as is illustrated in Figure 2.6, and the Voronoi diagrams will therefore consist of distorted hexagons.

Drawing Voronoi polyhedra aids in visualizing point defects such as vacancies, interstitials or line defects, such as dislocations. Dislocation line defects involve the translation of one part of a crystal (or *pseudo*-crystal in case of block copolymer ordering of microdomains) with respect to another.[52,53] Grain boundaries in (pseudo)-crystal packing are formed by a row of dislocations. Therefore, computational analysis of a plane of spheres, as for instance obtained from microscopy images, can be used to visualize grain boundaries and point defects, by assigning different colors to polyhedra with different coordination numbers. A dislocation core can then easily be observed, since it consists of a bound pentagon-heptagon pair. Additional information on calculating Voronoi diagrams based on image analysis is given in Appendix B.2.

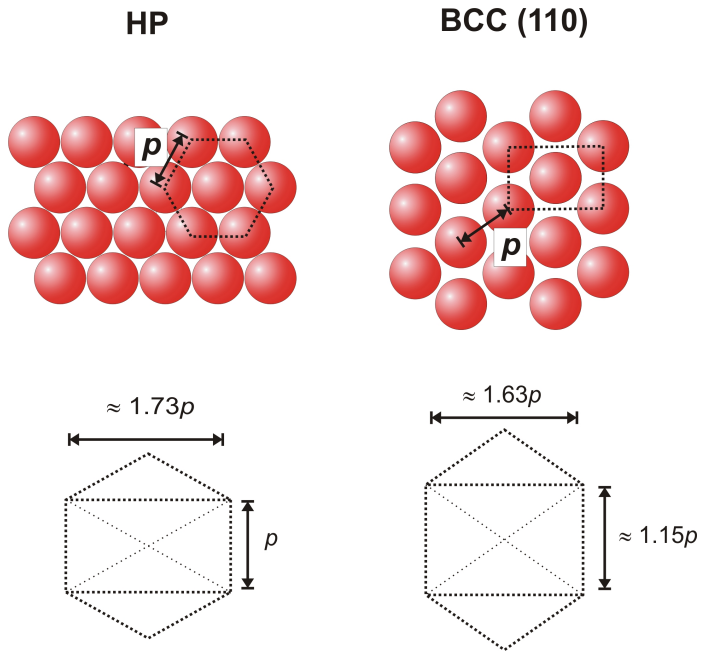

Figure 2.6: Geometrical difference between the in-plane hexagonal packing in a hexagonal packing (HP) and the (110) BCC plane.

Pair distribution function

A useful descriptor for short-range order in glasses and liquids is the dimensionless pair distribution function $g(r)$.[35,52] In the hard sphere model, departure of the local structure from randomness is due to excluded volume, arising from the relatively high packing density. The function $g(r)$, given in Eq. 2.15, addresses the distances between the centers of mass by counting the number of centers of mass dn in a small spherical shell volume ($2\pi r\,dr$ in a two dimensional plane) at each distance r from an arbitrary chosen center of mass. The statistical average for many arbitrary chosen origins is divided by the average particle density ($\langle p \rangle$) and the sampling volume.

$$g(r) = \frac{dn}{\langle p \rangle\, 2\pi r\, dr} \tag{2.15}$$

In case of a uniform radial density of center-of-mass over all sizes of the sampling volume, $dn/2\pi r\,dr$ is equal to the average particle density and $g(r)$ is unity. This is the case for dilute hard-sphere gasses. On the other hand, monoatomic crystals exhibit an infinite series of discrete peaks at the exact values of the interatomic separations. For all liquids and glasses, $g(r)$ will

show several maxima associated with short-range order, before reaching unity at larger values of r. This is schematically illustrated in Figure 2.7. The spatial extent of the short-range order to where order is lost and $g(r)$ asymptotically becomes unity, is the correlation length ξ. ξ describes the distance over which local correlation in the position or nearby center-of-masses is lost, $\xi = 2R_0$ for dilute gasses and ξ is infinite for perfect crystals. The pair distribution function $g(r)$ is 0 for values less than the hard sphere diameter $2\mathrm{R}_0$. Because correlations are strongest at the shortest distances, $g(r)$ is largest at a radial distance somewhat greater than $2\mathrm{R}_0$. The first peak gives the average nearest neighbor distance. The volume integral under this first peak gives the average number of nearest neighbors $\langle NN \rangle$. However, the exact shape of $g(r)$ is strongly influenced by the parameters used for the calculation. Since the resolution is the limiting factor in image analysis, which is based on microscopy techniques, care should be taken in deriving quantitative values from pair distribution functions. Detailed information on calculating $g(r)$ based on image analysis is given in Appendix B.3.

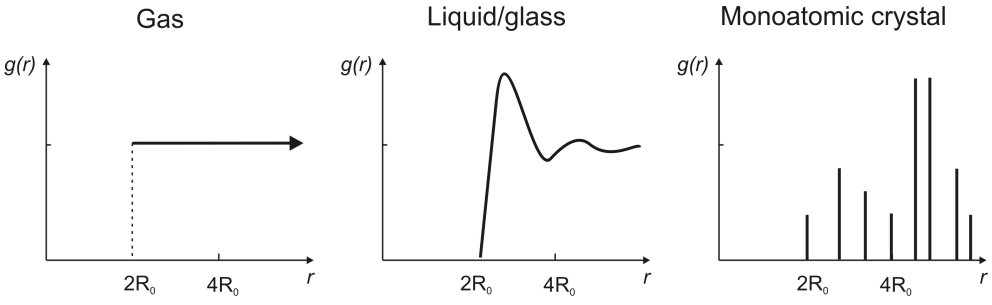

Figure 2.7: Pair-distribution functions for a gas, a liquid/glass and a monoatomic crystal. Adapted from [52].

Bibliography

[1] Hamley, I., *The Physics of Block Copolymers*, Oxford University Press, New York, 1998.

[2] Cowie, J., *Polymers: Chemistry and Physics of Modern Materials*, Chapman and Hall, Glasgow, 2nd ed., 1991.

[3] Loo, Y. -L., Register, R. A. and Ryan, A. J., *Phys. Rev. Lett.*, 2000, 84, 4120-4123.

[4] Loo, Y. -L. and Register, R. A. In *Developements in Block Copolymer Science and Technology*, Hamley, I., Ed., Vol. 114, John Wiley and Sons, 2004, 213-244.

[5] Hamley, I., In *Adv. Polym. Sci.*, 1999, Vol. 114, 113-137.

[6] Reiter, G., Castelein, G., Hoerner, P., Riess, G., Sommer, J. U. and Floudas, G., *Eur. Phys. J. E*, 2000, 2, 319-334.

[7] Strobl, G. R., *The Physics of Polymers*, Springer-Verlag Berlin, 2nd ed., 1997.

[8] Keddie, J. L., Jones, R. A. L. and Cory, R. A., *Faraday Discuss.*, 1994, 98, 219-230.

[9] Keddie, J. L., Jones, R. A. L. and Cory, R. A., *Europhys. Lett.*, 1994, 27, 59-64.

[10] Flory, P., *Principles of Polymer Chemistry*, Cornell University Press, Ithaca and London, 8th ed., 1971.

[11] Huggins, M., *J. Phys. Chem.*, 1942, 46, 151-158.

[12] Huggins, M., *J. Am. Chem. Soc.*, 1942, 64, 2716-2718.

[13] Leibler, L., *Macromolecules*, 1980, 13, 1602-1617.

[14] Helfand, E. and Wasserman, Z. R., In *Developements in Block Copolymers*, Vol. 1, 1982, 99-125.

[15] Fredrickson, G. H. and Helfand, E., *J. Chem. Phys.*, 1987, 87, 697-705.

[16] Matsen, M. W. and Bates, F. S., *Macromolecules*, 1996, 29, 7641-7644.

[17] Likhtman, A. E. and Semenov, A. N., *Europhys. Lett.*, 2000, 51, 307-313.

[18] Thomas, E. L., Anderson, D. M., Henkee, C. S. and Hoffman, D., *Nature*, 1988, 334, 598-601.

[19] Thomas, E. L. and Kascanec, R. L., *Phil. Trans. R. Soc. Lond. A*, 1994, 348, 149-166.

[20] Bates, F. S., Rosedale, J. H. and Fredrickson, G. H., *J. Chem. Phys.*, 1990, 92, 6255-6270.

[21] Bates, F. S. and Fredrickson, G. H., *Phys. Today*, 1999, 52, 32-38.

[22] Helfand, E., *Macromolecules*, 1975, 8, 552-556.

[23] Semenov, A. N., *Macromolecules*, 1993, 26, 6617-6621.

[24] Matsen, M. W. and Schick, M., *Macromolecules*, 1994, 27, 4014-4015.

[25] Matsen, M. W. and Bates, F. S., *Macromolecules*, 1996, 29, 1091-1098.

[26] Matsen, M. W. and Bates, F. S., *J. Pol. Sci., Part B: Polym. Phys.*, 1997, 35, 945-952.

[27] Hamley, I. W., *Nanotechnology*, 14, R39-R54.

[28] Fink, Y., Urbas, A. M., Bawendi, M. G., Joannopoulos, J. D., and Thomas, E. L., *J. Lightwave Technol.*, 1999, 17, 1963-1969.

[29] Yang, P. D., Wirnsberger, G., Huang, H. C., Cordero, S. R., McGehee, M. D., Scott, B., Deng, T., Whitesides, G. M., Chmelka, B. F., Buratto, S. K. and Stucky, G. D., *Science*, 2000, 287, 465-467.

[30] Zhao, D. Y., Feng, J. L., Huo, Q. S., Melosh, N., Fredrickson, G. H., Chmelka, B. F. and Stucky, G. D., *Science*, 1998, 279, 548-552.

[31] Thomas, E. L., Kinning, D. J., Alward, D. B. and Henkee, C. S., *Macromolecules*, 1987, 20, 2934-2939.

[32] Bates, F. S. and Fredrickson, G. H., *Annu. Rev. Phys. Chem.*, 1990, 41, 525-557.

[33] Fasolka, M. J. and Mayes, A. M., *Annu. Rev. Mater. Res.*, 2001, 31, 323-355.

[34] Cullity, B., *Elements of X-ray Diffraction*, Addison-Wesley Publishing Company, Inc., 1956.

[35] Chaikin, P. and Lubensky, T., *Principles of Condensed Matter Physics*, Cambridge University Press, 1995.

[36] Hamley, I. W. and Castelletto, V., *Prog. Polym. Sci.*, 2004, 29, 909-948.

[37] Benninghoven, A., Rudenauer, F., and Werner, H., *Secondary Ion Mass Spectrometry*, Wiley, 1987.

[38] Iltgen, K., Bendel, C., Benninghoven, A. and Niehuis, E., *J. Vacuum Sci. Technol. A*, 1997, 15, 460-464.

[39] Zalm, P. C., *Mikrochim. Acta*, 2000, 132, 243-257.

[40] Schwarz, S., Wilkens, B., Pudensi, M., Rafailovich, M. H., Sokolov, J., Zhao, X., Zhao, W., Zheng, X., Russell, T. P. and Jones, R., *Molec. Phys.*, 1992, 76, 937-950.

[41] Oslanec, R. and Brown, H. R., *Macromolecules*, 2001, 34, 9074-9079.

[42] Coulon, G., Russell, T. P., Deline, V. R. and Green, P. F., *Macromolecules*, 1989, 22, 2581-2589.

[43] Yokoyama, H., Kramer, E. J., Rafailovich, M. H., Sokolov, J. and Schwarz, S. A., *Macromolecules*, 1998, 31, 8826-8830.

[44] Segalman, R. A., Jacobson, A., Kramer, E. J. and Lustig, S. R., *Macromolecules*, 2004, 37, 2613-2617.

[45] Vezie, D. L., Thomas, E. L. and Adams, W. W., *Polymer*, 1995, 36, 1761-1779.

[46] Magonov, S., Cleveland, J., Elings, V., Denley, D. and Whangbo, M. -H., *Surf. Sci.*, 1997, 389, 201-211.

[47] Leclere, P., Lzzaroni, R., Bredas, J. L., Yu, J. M., Dubois, P. and Jerome, R., *Langmuir*, 1996, 12, 4317-4320.

[48] Park, M., Harrison, C., Chaikin, P. M., Register, R. A., and Adamson, D. H., *Science*, 1997, 276, 1401-1404.

[49] Lammertink, R. G. H., Hempenius, M. A. and Vancso, G. J., *Langmuir*, 2000, 16, 6245-6252.

[50] Olayo-Valles, R., Lund, M. S., Leighton, C. and Hillmyer, M. A., *J. Mater. Chem.*, 2004, 14, 2729-2731.

[51] Olayo-Valles, R., Guo, S. W., Lund, M. S., Leighton, C. and Hillmyer, M. A., *Macromolecules*, 2005, 38, 10101-10108.

[52] Allen, S. M. and Thomas, E. L., *The Structure of Materials*, John Wiley and Sons, New York, 1999.

[53] Segalman, R. A., Hexemer, A., Hayward, R. C. and Kramer, E. J., *Macromolecules*, 2003, 36, 3272-3288.

CHAPTER 3

Amorphous poly(ferrocenylsilane)s

Polyisoprene-*b*-polyferrocenyldimethylsilane block copolymer (PI-*b*-PFDMS) thin films do not require annealing to obtain regular, phase-separated patterns as the T_g's of the constituents are below or near room temperature. Over longer periods of time, however, the PFDMS crystallizes at room temperature. Hedrite-like structures form, destroying the microdomain morphology. To obtain stable, well-ordered nanostructures, crystallization of the organometallic constituent must be suppressed. This chapter describes a route to amorphous poly(ferrocenylsilane)s by copolymerizing symmetrically and unsymmetrically substituted, silicon-bridged ferrocenophanes. The thermal behavior of series of amorphous PFS and amorphous, low-T_g organic-organometallic block copolymers with narrow molar mass distributions is described. Small amounts of the comonomer were demonstrated to successfully suppress crystallization, as well as influence the intrinsic polymer characteristics, such as the glass transition, and the strength of phase segregation.

*Parts of this chapter have been published: Roerdink, M., Hempenius, M. A. and Vancso, G. J., *Chem. Mater.*, 2005, 17, 1275-1278.

3.1 Introduction

Block copolymers with poly(ferrocenylsilane) (PFS) blocks have been used to fabricate nanoscale structures in a variety of applications, including nanoperiodic dots and pillars in Si and Si_3N_4 [1,2], magnetic nanodots, [3] core-shell micelles for nanowires, [4] and nanopatterned surfaces for catalytic growth of carbon nanotubes, [5] as has been shown for asymmetric block copolymers composed of polystyrene (PS) and poly(ferrocenyldimethylsilane) (PFDMS) blocks. Polyisoprene (PI)-*b*-PFDMS thin films do not require annealing to obtain regular, phase separated patterns as the T_g's of the constituents are near room temperature. Over longer periods of time, however, PFDMS crystallizes at room temperature. Hedrite-like structures form, [6] destroying the microdomain morphology. To obtain stable, well-ordered nanostructures, crystallization of the organometallic constituent must be suppressed.

This chapter describes a route to amorphous poly(ferrocenylsilane)s, via the copolymerization of symmetrically and unsymmetrically substituted, silicon-bridged ferrocenophanes. The use of small amounts of monomers that impart irregularity to the chains has been applied for decades in industry for the tuning of crystallinity. Particularly, copolymerizations involving vinyl esters or polypropylenes have been widely studied for the effect of the number and length of branches on the polymer properties. [7–11] Copolymerization with branched units does not only introduce chain irregularity, but also segmental mobility to the chains. For example, the effect of the amount and the length of branches in copolymerizations with metallocene catalyzed polypropylene has been studied for over thirty years [7,8] and is still an active field of research. Particularly, linear correlations of the glass transition and thus segmental volume and flexibility with branching have been described. [9–11]

In the first section of this chapter, a route to amorphous PFS by copolymerization is explored. The synthesis of amorphous PFS copolymers will be described and the influence of the amount of comonomer on the degree of crystallization and on the glass transition is investigated. Since we are primarily interested in amorphous PI-*b*-PFS block copolymers, the study on crystallinity is extended to the corresponding block copolymers. The next section focusses on a study of the morphology of these block copolymers and on an important thermal transition, the order-disorder transition, a highly relevant block copolymer property for utilization in thin film applications.

3.2 Statistical copolymers of PFS

3.2.1 Suppressing crystallization

Amorphous poly(ferrocenylsilane)s are in principle obtained by polymerization of unsymmetrically substituted, silicon-bridged ferrocenophanes.[12] Another route to amorphous PFS may be via the addition of small amounts of unsymmetrically substituted monomer during polymerization to suppress crystallization. This method was explored for dimethyl[1]silaferrocenophane, copolymerized with various amounts of ethylmethyl[1]silaferrocenophane, which resulted in well-defined statistical PFS copolymers with narrow molar mass distributions (see Figure 3.1).

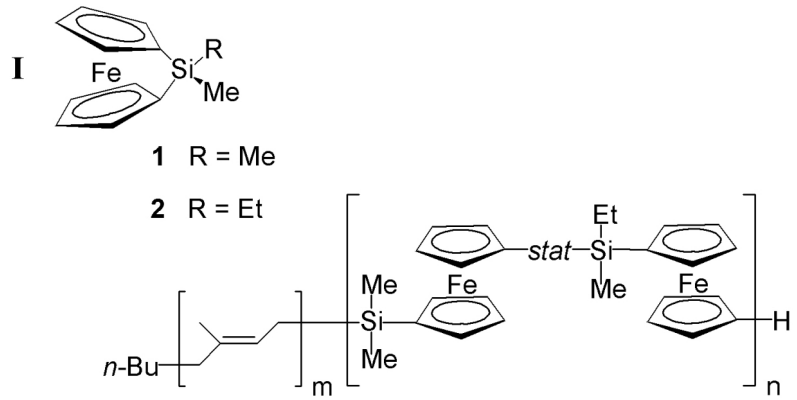

Figure 3.1: PI-*b*-PFS block copolymer featuring a predominantly amorphous organometallic block.

The characteristics of some of the statistical PFS copolymers and corresponding block copolymers used for the study of the thermal properties are listed in Table 3.1. To assess the degree of suppression of crystallization, isothermal crystallization at 95 °C was allowed for two hours for the polymers listed in Table 3.1. At this temperature, the rate of crystallization of PFDMS was found to be the highest.[13] DSC heating scans were recorded immediately after isothermal crystallizations. Figure 3.2 shows the heating scans for the PFS homopolymers (left) and block copolymers (right).

For F15, trace A, two endothermic peaks associated with the melting-recrystallization of PFDMS were observed.[13] Upon introducing ethylmethylsilylferrocenyl (EM) units in the chains, the melting transitions shift to lower

Table 3.1: Characteristics of PFS statistical copolymers and PI-*b*-PFS block copolymers used in the crystallization study.

	M_n[a] [kg/mol]	M_w[a] [kg/mol]	M_w/M_n[a]	EM[b] [mol%]	PFS[b] [vol%]
F15	15	17	1.10	0	
F13EM5	13	14	1.05	5	
F16EM12	16	18	1.11	12	
F15EM23	15	17	1.09	23	
IF58/22	80	83	1.04	0	22
IF54/18EM6	72	74	1.03	6	19
IF52/20EM7	72	75	1.04	7	22
IF55/22EM23	77	81	1.05	23	23

[a]Measured by GPC in THF, relative to polystyrene standards. [b]Measured by ^{1}H NMR.
The notation used to identify the polymers includes the corresponding molar masses (M_n, in 10^3 g/mol), and if applicable the mol% of incorporated EM units. For example, F13EM5 is a 13000 g/mol PFS polymer with 5 mol% EM units incorporated, and IF54/18EM6 is a 54000 g/mol polyisoprene-*b*-18000 g/mol poly(ferrocenylsilane) diblock copolymer, with 6 mol% EM in the PFS block.

temperatures as anticipated for statistical copolymers.[14] At 12 mol% EM the high-temperature melting transition disappeared. Melting transitions were no longer observed upon increasing the EM percentage to 23%. A similar trend of decreasing, and subsequently disappearing, melting transitions was found for the corresponding PI-*b*-PFS block copolymers (Figure 3.2, bottom). Thin films of PI-*b*-PFS containing 11 mol% of EM showed no sign of crystallization after being kept at room temperature for one to two days. At higher incorporated EM contents (23 mol% or more), crystallization was suppressed for a longer period of time.

3.2.2 Glass transitions in amorphous PFS

As discussed in Section 3.1, numerous examples of a linear depression of the glass transition with the amount of branched comonomer units exist. Therefore, a depression of the glass transition temperature for amorphous PFSs is expected compared to PFDMS, which has a T_g of 33.5 °C in the extrapolation

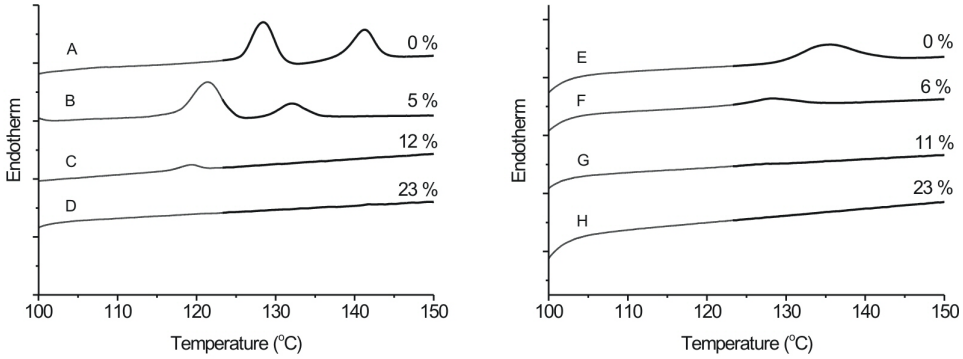

Figure 3.2: DSC heating scans of PFS copolymers (left) with increasing amounts of EM: A) PFDMS, B) F13EM5, C) F16EM12 and D) F15EM23. DSC heating scans of PI-*b*-PFS block copolymers (right) with increasing amounts of EM: E) IF58/22, F) IF54/18EM6, G) IF52/20EM11 and H) IF56/21EM23. All samples were kept at 95 °C for 2 h, prior to heating.

to infinite molar mass $T_{g,\infty}$.[13] Besides a possible effect of the amount of EM units, there are several other factors that influence the temperature range of the actual glass transition, among which the most important are the molar mass and the molar mass distribution. The molar mass dependence of the T_g can be accounted for by employing the empirical O'Driscoll relation

$$T_g = T_{g,\infty} - \frac{K}{{M_n}^{2/3}} \tag{3.1}$$

where K is related to the excess free volume at the chain ends. Figure 3.3 shows the result for all PFS polymers with various amounts of EM (see Table 3.2) in an O'Driscoll plot.

It is difficult to compare the plotted data in Figure 3.3, since the amount of EM differs from 0 to 100%. Dividing the data roughly in two groups of less than and more than 30 mol% EM aids in visualizing the general trend, which is a lowering of the glass transition upon incorporation of ethylmethyl[1]silaferrocenophane, as expected. The large scattering in the values is understandable, considering the randomness of the incorporation of the comonomer. We expect to have a relatively homogeneous distribution of the comonomer over the polymer chains, since mostly narrow molar mass distributions were obtained. Still, small variations in the block lengths of EM (E) and DM (D), for example —DDEEEDD— compared to —DEDEDED— will lead to differences in the bulk properties. Such variations are expected only for larger

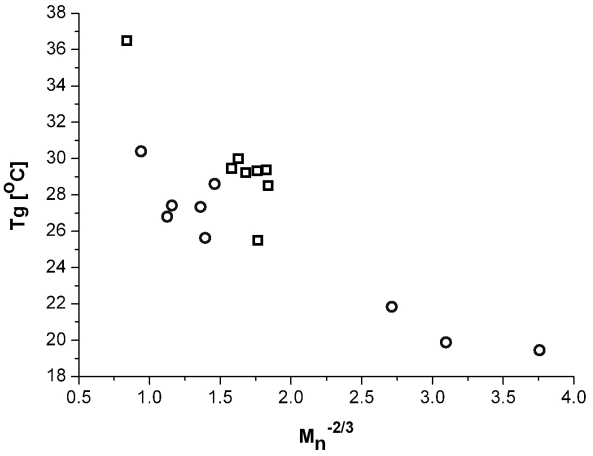

Figure 3.3: T_g versus $M_n^{-\frac{2}{3}}$ for PFS polymers with various amounts of ethylmethyl-[1]silaferrocenophane (□ EM $\leq$ 30%, O 30 $<$ EM $\leq$100).

amounts of incorporated EM units. In addition, the distribution in molar mass affects the glass transition, which is not accounted for in Eq. 3.1.

Despite the considerations on the scatter in depression of the T_g, the overall lowering is clear, and consistent with other reports on polymer T_gs.[15] The EM units in the PFS backbone increase the free volume, which enhances skeletal conformational motions, resulting in the observed decrease in the glass transition temperature.[16]

3.3 Amorphous PI-*b*-PFS

3.3.1 Bulk morphology

Small angle X-ray scattering (SAXS) measurements on PI-*b*-PFS were carried out to establish the bulk morphology by determining the relative peak positions in the scattering profiles for a large number of PI-*b*-PFS polymers (see Table A in the appendix). Typical scattering intensity profiles and the corresponding azimuthally averaged data are shown in Figure 3.4. The relative peak positions of the two examples shown indicate a BCC and a HEX morphology of these polymers. For the block copolymer studied, BCC morphology was found at PFS volume fractions up to 21 vol%. At higher volume fractions a HEX morphology occurred.

Figure 3.5 shows the *d*-spacing determined by SAXS as a function of molar mass for the block copolymers listed in Table A. A linear fit describes

Table 3.2: Molar mass and glass transition temperatures of statistical PFS copolymers.

	M_n [a] [kg/mol]	M_w [a] [kg/mol]	M_w/M_n [a]	EM [b] [mol%]	T_g [c] [°C]
F14	14	14	1.05	0	25.5
F15	15	21	1.43	0	29.2
F15	15	17	1.10	0	30.0
F13EM5	13	14	1.06	5	29.4
F41EM6	41	61	1.48	6	36.5
F13EM10	13	13	1.06	10	28.5
F14EM11	14	14	1.03	11	29.3
F15EM23	15	17	1.10	23	18.7
F16EM12	16	18	1.12	12	29.5
F35EM31	35	46	1.32	31	30.4
F18EM50	18	21	1.19	50	28.6
F7EM53	7	7	1.05	53	21.8
F4EM88	4	5	1.18	88	19.5
PFEMS-6[d]	6	6	1.06	100	19.9
PFEMS-19	19	32	1.65	100	25.6
PFEMS-20	20	22	1.12	100	27.3
PFEMS-25	25	37	1.52	100	27.4
PFEMS-27	27	48	1.81	100	26.8

[a]Measured by GPC in THF, relative to polystyrene standards. [b]Measured by ^{1}H NMR. [c]Measured by DSC heating curves. [d]The notation PFEMS is used for poly(ferrocenylethylmethylsilane) homopolymers, and includes the molar mass.

the dependence of the d-spacing on the degree of polymerization well, when normalized for variations in PFS volume fraction. The linear dependence also corresponds well with the theoretical analysis as formulated by Meier and Helfand for lamellar block copolymers,[17,18] based on Gibbs free energy considerations. When adapted for spherical and hexagonal morphologies, this results in slopes of 0.82 and 0.78, respectively.[19] From the measured d-spacings, the interdomain distances p for the block copolymer can be calculated and are shown in Figure 3.6.

The values for the d-space are in reasonably good agreement with the molar mass dependence. However, the probed polymers have an additional parameter, which is the amount of EM units incorporated. The deviations

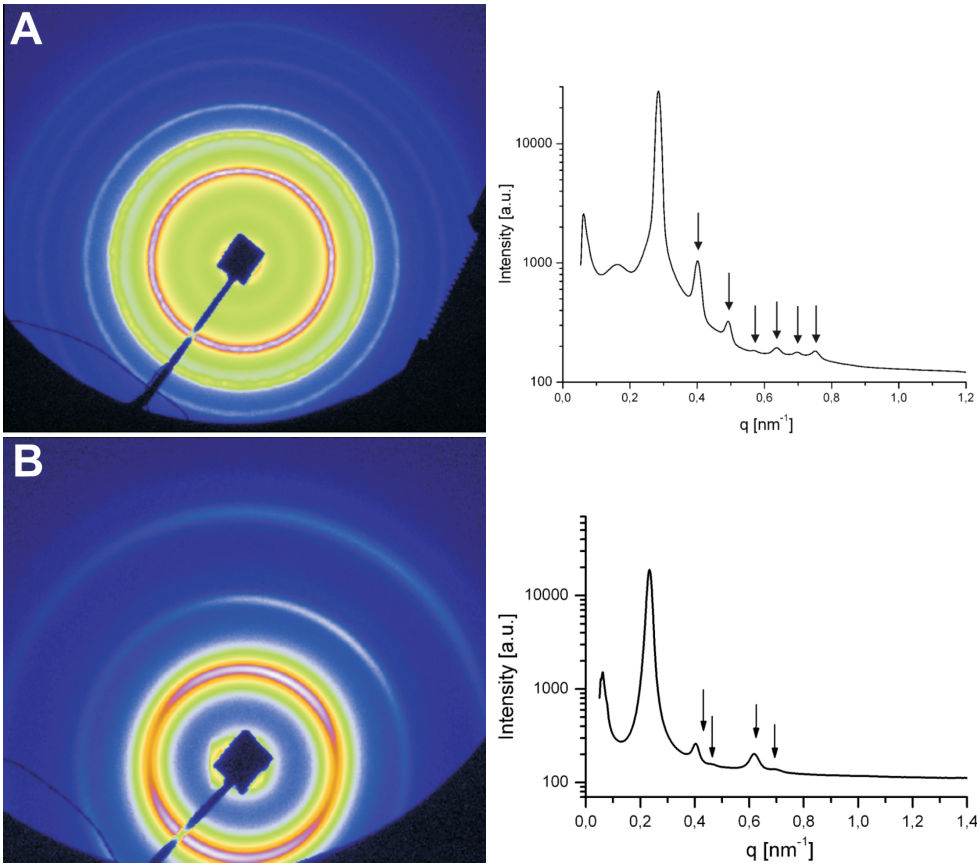

Figure 3.4: SAXS intensity scattering profile and the azimuthally averaged 2D plot of IF35/11EM11 with relative peak positions at $\sqrt{2}, \sqrt{3}, \sqrt{4}, \sqrt{5}, \sqrt{6}$ and $\sqrt{7}$, denoting a BCC lattice (A), and of IF31/19EM12 with relative peak positions at $\sqrt{3}, \sqrt{4}, \sqrt{7}$ and $\sqrt{9}$, denoting a HEX lattice (B).

in Figures 3.5 and 3.6 from linearity are therefore worth to examine in more detail. The *d*-spacing for two series of block copolymers with similar molar mass and PFS volume fraction were plotted as a function of the amount of EM (see Figure 3.7). The *d*-space increases with an increase in the amount of incorporated EM and this trend was found for all block copolymers. The change in *d*-spacing in the examples of Figure 3.7 is about 3 nm, which is too large to be fully attributed to inaccuracy in the SAXS measurements or in the polymer characteristics. Rather, the increase in *d*-spacing can tentatively be ascribed to a weaker phase separation.

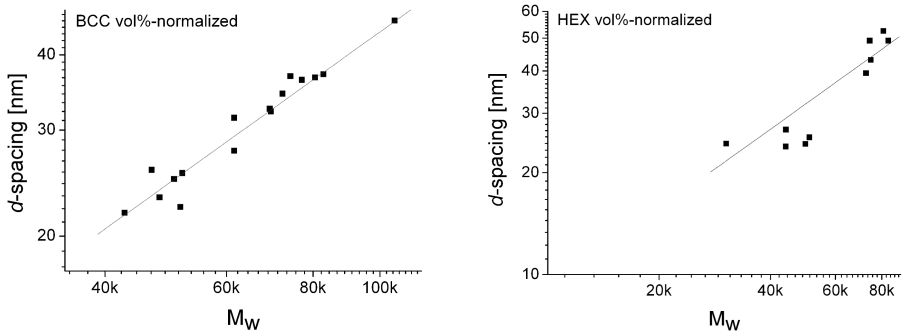

Figure 3.5: Dependence of the *d*-spacing (determined by SAXS) on the molar mass of PI-*b*-PFS polymers for spherical BCC and cylindrical HEX morphologies. The slope of the linear fit in the double logarithmic plots equals 0.82 and 0.76 for BCC and HEX, respectively.

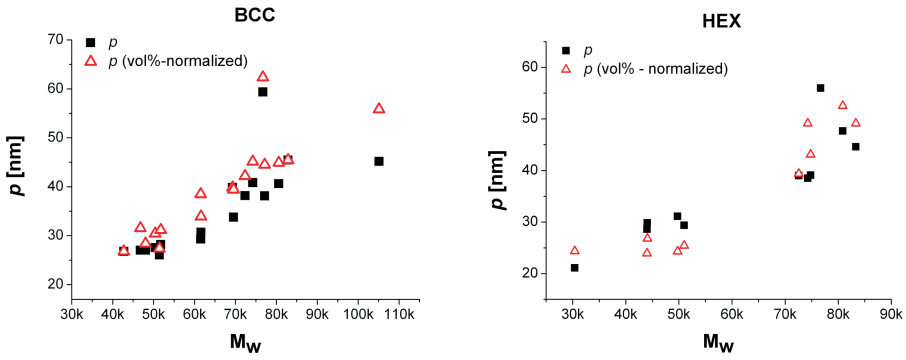

Figure 3.6: Dependence of the interdomain distance *p* (determined by SAXS) on the degree of polymerization of PI-*b*-PFS polymers for spherical BCC and cylindrical HEX morphologies.

3.3.2 Order-disorder transitions

The order-disorder transition (ODT) temperatures for PI-*b*-PFS with different molar masses and amounts of incorporated EM were determined using rheology and SAXS.

Determination of ODTs by rheology was based upon dynamic mechanical measurements, where the energy lost or stored per cycle is related to the flow behavior.[20–23] In the ordered state, the microdomains act as physical crosslinks resulting in rubbery behavior, while in the disordered state the material exhibits normal flow as for homopolymer melts. The storage modulus (G') is related to the elastically stored energy and is typically much higher

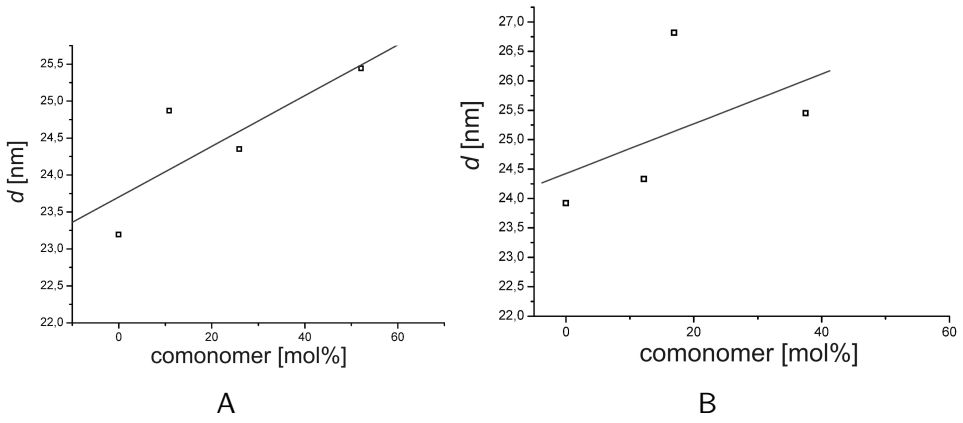

Figure 3.7: Plots of d-spacing versus the amount of incorporated EM for two series of PFS homopolymers with similar molar mass and microphase morphology, *i.e.* BCC morphology (A) and HEX mophology (B).

(about 10^5 Pa for rubbery polymers) than the loss modulus (G''), which is related to the dissipated energy. The storage and loss moduli can be used to determine order-disorder transitions by observing a sharp drop in the storage modulus (and a smaller drop in the loss modulus) when going from an ordered to a disordered phase. However, distinguishing between rubbery behavior caused by a phase-separated morphology or by the presence of small crystalline areas is not possible, with the result that an ODT cannot be discerned from a drop in moduli if both transitions are around similar temperatures.

Figure 3.8A shows SAXS patterns of IF at 200 °C, recorded for a time period of 10 minutes. No changes in morphology were observed, suggesting that during the time interval of 10 min, degradation or crosslinking is not of consequence for the determination of the ODT. Several heating and cooling cycles were performed with each sample and examined for indications of crosslinking or degradation. The absence of higher order, the presence of order in conjunction with the complete absence of a transition to a disordered phase, or a considerable change of the ODT temperature, due to the lack of large scale diffusion, were considered indications of chemical degradation. After a heating and cooling run the typical morphological scattering pattern was regained and lost again upon another heating run, and crosslinking was therefore assumed to be negligible. In addition to our own experimental observations, many examples have been reported of block copolymers that were chemically stable at high temperatures and where PI constituted one of the phases. Order-disorder temperatures for PS-*b*-PI and PS-*b*-PI-*b*-PS have been reported from 90 °C up to 300 °C, depending on the molar mass.[23–26]

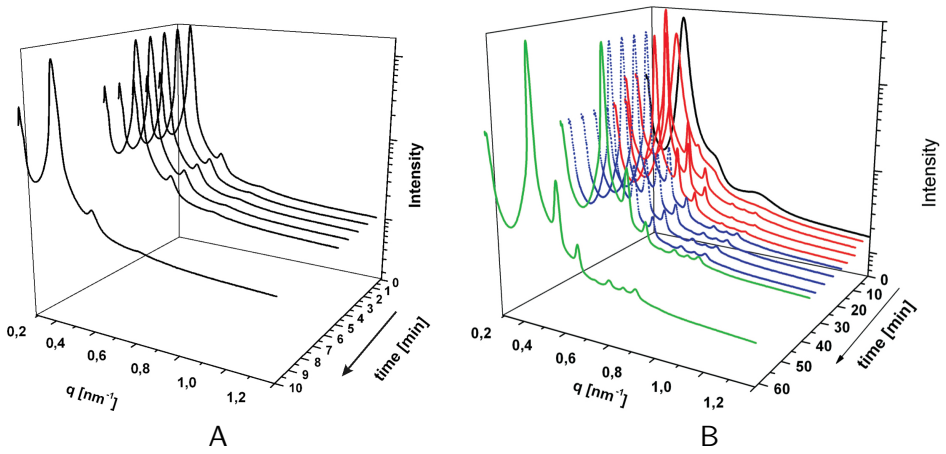

Figure 3.8: Time-resolved SAXS patterns of IF30/15EM38 at 200 °C (A) and time-resolved SAXS patterns of IF34/11EM52 in an annealing cycle: unannealed (black, solid line), 130 °C (red, solid lines), cooling down to 60 °C in 3.5 min (blue, dotted lines) and room temperature (green, solid lines)(B). See also Figure C.1.

Observation of the speed of the development of sharp scattering profiles at different temperatures enabled the determination of an optimal annealing strategy for the bulk polymer samples. Figure 3.8B demonstrates time-resolved SAXS patterns of IF34/11EM52 in an annealing procedure, in which a sample of IF was kept at 130 °C for 10 min, to ensure that crystalline microdomains are absent (since T_m is 120 °C in PI-*b*-PFS, see section 3.2.1). After a few minutes of heat treatment a BCC pattern developed. The sample was quenched to 60 °C in order to allow the chains to equilibrate, while the chains retained sufficient mobility to rearrange.

The order-disorder transitions were taken from the heating curves at the temperature where the higher order diffraction peaks are lost. Figure 3.9 shows SAXS patterns of typical heating and cooling cycles, in this case for IF34/11EM52. No time was allowed for the material to equilibrate between capturing the cooling curves, and thus a full recovery of the SAXS pattern during the cooling process was not observed for most of the polymers.

Often, the loss of microphase separated morphology is accompanied by a profound drop in the intensity of the first diffraction peak. In Figure 3.10 the maximal intensity of the first diffraction peak at each temperature, $I_{\max,1}$, corresponding to the SAXS patterns of Figure 3.9, is shown. The order-disorder transition is located at 200 °C upon heating, and upon cooling at 125 °C, where this last value was determined through $I_{\max,2}$ (not shown). This hysteresis in the ODT temperature upon cooling can be ascribed to a combination

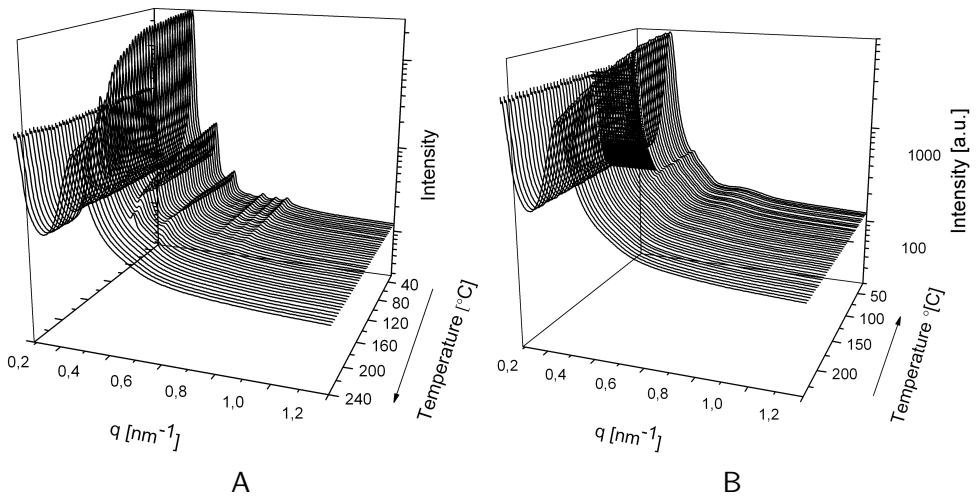

Figure 3.9: Heating run (A) and cooling run (B) temperature-resolved SAXS patterns of IF34/11EM52.

of a considerably decrease in mobility, which causes equilibration of the structures during cooling at 10 °C/min to be strongly hampered,[27] as well as to spinodal fluctuations near the order-disorder transition.

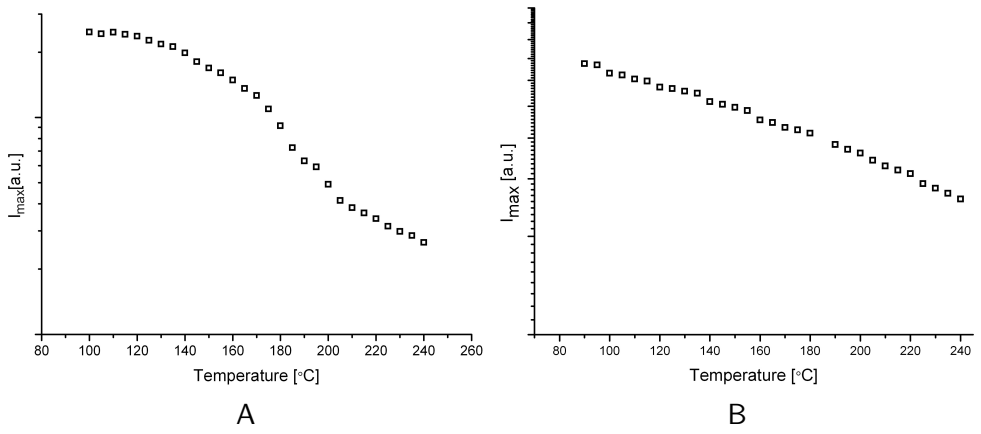

Figure 3.10: Maximal intensity of the first diffraction peak ($I_{\max,1}$) of the heating run (A) and cooling run (B) temperature–resolved SAXS patterns of IF34/11EM52.

Order-disorder temperatures for polymers with close-packed spheres and hexagonally packed cylinders, both sets of similar molar mass but with various amounts of comonomer, were determined using SAXS. Figure 3.11 shows $I_{\max,1}$

as a function of temperature for three polymers, IF33/11, IF37/12EM26 and IF38/13EM100. The characteristics and the ODTs of these block copolymers and a few more are listed in Table 3.3. ODTs determined by means of dynamic mechanical measurements (not shown) agreed with the SAXS results and were typically found to be 5 - 15 °C lower.

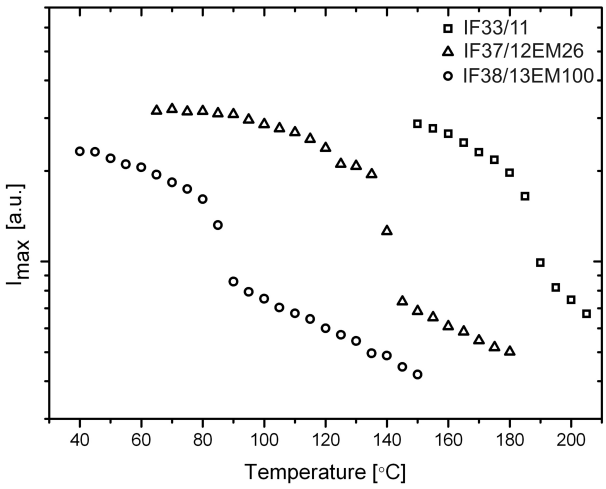

Figure 3.11: Maximal intensity of the first diffraction peak ($I_{\max,1}$) of heating runs of three PI-*b*-PFSs with varying amounts of EM incorporated.

The obtained values for the ODTs show a significant decrease of more than 100 °C with increasing comonomer content. This strong dependence on the concentration of EM units is on first hand in contrast with the rather small effects on the T_g and d-spacing in the bulk morphology. The decrease in ODT temperature denotes a lower value for the Flory-Huggins χ parameter for higher EM contents. As discussed in Chapter 2, a lower χ parameter denotes a weaker phase segregation at a given chain length, but also corresponds to a thicker interfacial area between the two blocks (Equation 2.4). Considering the chemical structures of both polyisoprene and poly(ferrocenylsilane), the EM comonomer increases the similarity of PFS and PI, which has affects on the phase separation, while exerting only a small influence on the bulk morphology and glass transition.

Table 3.3: ODTs for two series of amorphous PI-*b*-PFSs with similar molar mass and morphology.

polymer	M_n [kg/mol]	M_w [kg/mol]	M_w/M_n	PFS [vol%]	EM [mol%]	ODT [°C]
		$M_w \sim$ 50k, BCC				
IF33/11	45	51	1.13	20	0	205
IF35/11EM11	45	47	1.04	18	11	140
IF37/12EM26	49	50	1.04	19	26	145
IF37/13EM100	51	51	1.03	20	100	85
		$M_w \sim$ 50k, HEX				
IF30/18EM12	48	50	1.04	31	12	320
IF27/15EM16	43	49	1.14	29	16	305
IF30/16EM38	46	51	1.11	28	38	200

3.4 Conclusions

The synthesis of amorphous PI-*b*-PFS was established through copolymerization of dimethyl[1]silaferrocenophane with unsymmetrically substituted ethylmethyl[1]silaferrocenophane comonomer. Small amounts of the comonomer were demonstrated to successfully suppress crystallization, as well as influence the intrinsic polymer characteristics through changes in PFS skeletal mobility. A slight depression in the glass transition temperature of the amorphous poly(ferrocenylsilane) homopolymers was shown with increasing comonomer content, denoting a higher chain flexibility. Through SAXS measurements, the morphology and corresponding block copolymer repeat lengths of a large number of block copolymers could be determined. The repeat lengths increased slightly with the amount of comonomer in the polymer chains, suggesting a weaker phase segregation. This was corroborated by a considerable decrease in the order-disorder transition temperatures. Therefore, the order-disorder transition temperature can be tuned for these block copolymers by incorporating asymmetrically substituted monomer during polymerization, while retaining the glass-rubbery transition, as well as the length scales associated with the microdomain morphology. As knowledge of the ODT temperature is crucial for equilibrating the microphase separated morphology, this is an interesting result in designing PI-*b*-PFSs for applications where well-equilibrated structures are required.

3.5 Experimental

Materials and Polymerizations Ferrocene, *N,N,N',N'*-tetramethylethylenediamine (TMEDA), dichlorosilanes (dimethyl- and ethylmethyl-), and *n*-butyllithium were purchased from Aldrich. Dimethyl[1]silaferrocenophane **1** and ethylmethyl[1]silaferrocenophane **2** were prepared and purified as described earlier.[12] Anionic polymerizations[28,29] were carried out in THF in a MBraun Labmaster 130 glove box under an atmosphere of prepurified nitrogen (<0.1 ppm H_2O). Statistical copolymers of PFS, poly(ferrocenyldimethylsilane-*stat*-ferrocenylethylmethylsilane) (Figure 3.1), were precipitated in methanol and dried under vacuum. Poly(isoprene-*b*-ferrocenylsilane)s (PI-*b*-PFS)s were synthesized by sequential anionic polymerization. Isoprene polymerizations in ethylbenzene were initiated by *n*-butyllithium. After completion of the isoprene block, **1** and **2** were added, followed by THF, for the formation of the PFS block. Degassed methanol was added after 1 h. The polymers were precipitated in methanol and dried under vacuum. Small amounts (< 0.1 wt%) of the block copolymers to be used in SAXS were redissolved in THF containing stabilizer (2,6-di-*tert*-butyl-4-methylphenol), the THF was evaporated and the polymer samples were dried under vacuum.

Instrumentation ^{1}H NMR spectra were recorded in $CDCl_3$ on a Varian Unity Inova (300 MHz) instrument at 300.3 MHz and on a Varian Unity 400 spectrometer at 399.9 MHz. A solvent chemical shift of $\delta = 7.26$ ppm was used as a reference. Systematic errors in the determination of the PFS volume fraction and the amount of EM units calculated from ^{1}H NMR were estimated to be ± 1 vol% and ± 5 mol%, respectively. Gel permeation chromatography (GPC) measurements were carried out in THF at 25°C, using microstyragel columns with pore sizes of 10^5, 10^4, 10^3 and 10^6 $\dot{A}$ (Waters) and a dual detection system consisting of a differential refractometer (Waters model 410) and a differential viscometer (Viscotek model H502). Molar masses were determined relative to polystyrene standards. Systematic errors in the obtained molar masses were estimated to be < 5%. Differential scanning calorimetry (DSC) measurements were performed on a Perkin-Elmer DSC-7 and a Perkin-Elmer Pyris 1 instrument. The T_g was taken at the half C_p extrapolated value (heating rate 10 °C). Rheological measurements were performed on a Physica UDS 200 rheometer using a parallel plate configuration. The gap between the plates was 0.5 mm. A constant strain of 1 % was applied at an angular frequency of 1 Hz, while the temperature was ramped from 40 °C to higher temperatures (200-300 °C) with 0.25 °C/min.

Small-angle X-ray scattering[1] Small angle x–ray scattering (SAXS)

[1]The SAXS work was conducted at the Cornell High Energy Synchrotron Source (CHESS) which is supported by the National Science Foundation and the National Institutes of Health/National Institute of General Medical Sciences under award DMR-0225180.

patterns were obtained at the Cornell High Energy Synchrotron Source (station G1) at Cornell University, Ithaca (New York), using a Filicam detector (69.78 μm/pixel) (see Figure 3.12). Beam: 10 kV, $\lambda = 1.2390 - 1.2495\,\dot{A}$, 0.5 x 0.5 mm. The sample-detector distance was 2080 - 2184 mm. Temperature-dependent measurements were performed using a hot stage, type Mettler FP82HT. Heating rates were typically 10 °C/min. Variations in the heating rate did not influence the temperature found for the order-disorder transition. In a typical experiment, 10-20 mg of a block copolymer was enclosed between kapton foil under an nitrogen atmosphere and annealed in the hot stage at 150 °C during 10 min, and subsequently cooled down to 60 °C for another 10 min. The systematic error in the d-spacings measured was estimated to be $<$ 1 nm.

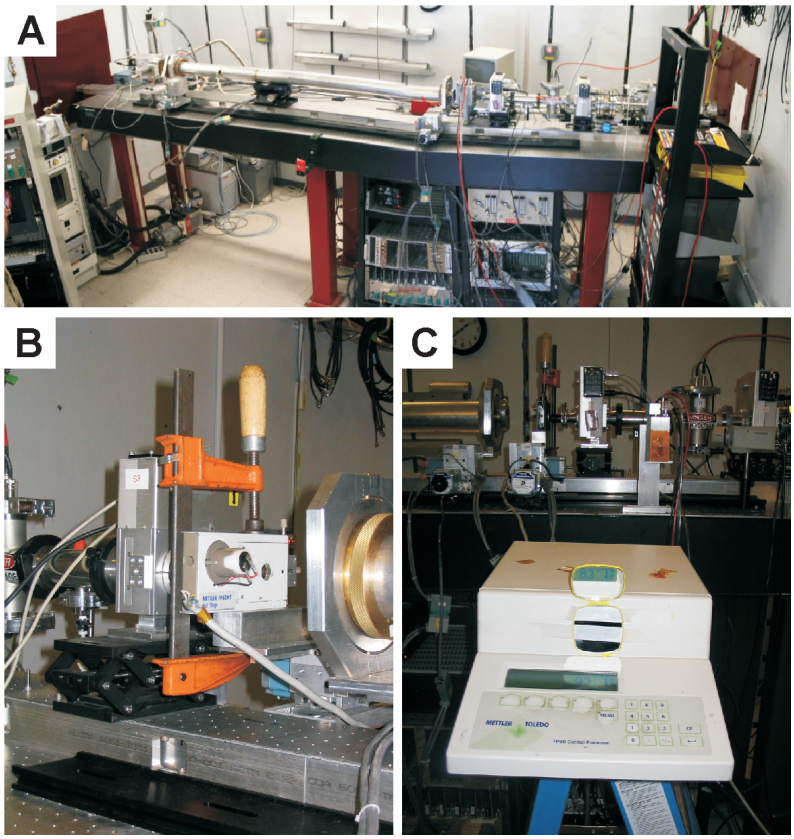

Figure 3.12: G1 Line at the Cornell High Energy Synchrotron Source, used for SAXS measurements. A) Table setup. B,C) The hot stage setup used for temperature dependent measurements (See also Figure C.2).

Bibliography

[1] Lammertink, R. G. H., Hempenius, M. A., van den Enk, J. E., Chan, V. Z. -H., Thomas, E. L. and Vancso, G. J., *Adv. Mater.*, 2000, 12, 98-102.

[2] Cheng, J. Y., Ross, C. A., Smith, H. I. and Vancso, G. J., *Appl. Phys. Lett.*, 2002, 81, 3657-3659.

[3] Cheng, J. Y., Ross, C. A., Chan, V. Z. -H., Thomas, E. L., Lammertink, R. G. H. and Vancso, G. J., *Adv. Mater.*, 2001, 13, 1174-1178.

[4] Cao, L., Massey, J. A., Winnik, M. A., Manners, I., Rietmüller, S., Banhart, F., Spatz, J. P. and Möller, M., *Adv. Funct. Mater.*, 2003, 13, 271-276.

[5] Hinderling, C., Keles, Y., Stöckli, T., Knapp, H. F., De los Arcos, T., Oelhafen, P, Korczagin, I., Hempenius, M. A., Vancso, G. J., Pugin, R. and Heinzelmann, H., *Adv. Mater.*, 2004, 16, 876-879.

[6] Lammertink, R. G. H., Hempenius, M. A. and Vancso, G. J., *Langmuir*, 2000, 16, 6245-6252.

[7] Karasz, F. and MacKnight, W., *Macromolecules*, 1968, 1, 537-540.

[8] Van Hoorn, H., *Rheol. Acta*, 1971, 10, 208-212.

[9] Mader, D., Heinemann, J., Walter, P. and Mulhaupt, R., *Macromolecules*, 2000, 33, 1254-1261.

[10] Lovisi, H., Tavares, M. I. B, Da Silva, N. M., De Menezes, S. M., De Santa Maria, L. C. and Coutinho, F. M., *Polymer*, 2001, 42, 9791-9799.

[11] Dlubek, G., Bamford, D., Rodriguez-Gonzaleza, A., Bornemann, S., Stejny, J., Schade, B., Alam, M. and Arnold, M., *J. Pol. Sci., Part B: Polym. Phys.*, 2002, 40, 434-453.

[12] Foucher, D., Ziembinski, R., Peterson, R., Pudelski, J., Edwards, M., Ni, Y., Massey, J. A., Jaeger, C. R., Vancso, G. J. and Manners, I., *Macromolecules*, 1994, 27, 3992-3999.

[13] Lammertink, R. G. H., Hempenius, M. A., Manners, I. and Vancso, G. J., *Macromolecules*, 1998, 31, 795-800.

[14] Flory, P., *Statistical Mechanics of Chain Molecules*, London: Interscience, 1969.

[15] Rider, D. A., Cavicchi, K. A., Power-Billard, K. N., Russell, T. P. and Manners, I., *Macromolecules*, 2005, 38, 6931-6938.

[16] Gómez-Elipe, P., Resendes, R., MacDonald, P. M. and Manners, I., *J. Am. Chem. Soc.*, 1998, 120, 8348-8356.

[17] Helfand, E. and Wasserman, Z. R., In *Developements in Block Copolymers*, Vol. 1, Goodman, I., Ed., Applied Science, London, 1982, 99-125.

[18] Helfand, E., *Macromolecules*, 1992, 25, 492-493.

[19] Strobl, G. R., *The Physics of Polymers*, Springer-Verlag Berlin, 2nd ed., 1997.

[20] Fredrickson, G. H. and Helfand, E., *J. Chem. Phys.*, 1988, 89, 5890-5897.

[21] Bates, F. S., Rosedale, J. H. and Fredrickson, G. H., *J. Chem. Phys.*, 1990, 92, 6255-6270.

[22] Rosedale, J.H. and Bates, F. S., *Macromolecules*, 1990, 23, 2329-2338.

[23] Khandpur, A. K., Forster, S., Bates, F. S., Hamely, I. W., Ryan, A. J., Bras, W., Almdal, K. and Mortensen, K., *Macromolecules*, 1995, 28, 8796-8806.

[24] Abetz, V. and Simon, P. F. W., In *Block Copolymers I*, Vol. 189 of *Adv. Polym. Sci.*, 2005, p125-212.

[25] Sakamoto, N., Hashimoto, T., Han, C., Kim, D. and Vaidya, N., *Macromolecules*, 1997, 30, 1621-1632.

[26] Hashimoto, T., Ogawa, T., Sakamoto, N., Ichiniya, M., Kim, J. and Han, C., *Polymer*, 1997, 39, 1573-1581.

[27] Bondzic, S., De Wit, J, Polushkin, E., Schouten, A. J., Ten Brinke, G., Ruokolainen, J., Ikkala, O., Dolbnya, I. and Bras, W., *Macromolecules*, 2004, 37, 9517-9524.

[28] Rulkens, R., Ni, Y., and Manners, I., *J. Am. Chem. Soc.*, 1994, 116, 12121-12122.

[29] Ni, Y., Rulkens, R., and Manners, I., *J. Am. Chem. Soc.*, 1996, 118, 4102-4114.

CHAPTER 4

Thin films of PI-*b*-PFS

The substrate wetting of an amorphous, low glass transition spherical poly(isoprene-*b*-ferrocenylsilane) (PI-*b*-PFS) block copolymer was studied. A dynamic time-of-flight secondary ion mass spectrometry (TOF-SIMS) study indicated the presence of both PI and PFS directly at the film - substrate interface on silicon and silica substrates. The dynamic TOF-SIMS depth profiling study indicated a transition in the packing morphology of the domains between the 2D monolayer and 3D thicker layers. In a monolayer of domains, a hexagonal packing was adopted. In films of two or three layers, the hexagonal packing reorganized towards a BCC packing by the extension of the copolymer chains in the direction normal to the substrate, as indicated by an increase in spacing between layers and an increase in domain size. For thicker layers, a BCC morphology with the (110) plane parallel to the substrate was found that extended from the free surface down to the substrate. The copolymer exhibited long-range ordering on the micron scale on flat silicon substrates without high-temperature annealing.

*Parts of this chapter are accepted for publication in *Small* as: Roerdink, M., Hempenius, M. A., Gunst, U., Arlinghaus, H. F. and Vancso, G. J., *Substrate wetting and topologically induced ordering of amorphous PI-b-PFS block copolymer domains.*

4.1 Introduction

Block copolymers have the ability to form regular arrays of microdomains. The self-assembled structures provide a convenient and cost-effective method of fabricating nanostructures of 10 – 100 nm,[1] a length scale not addressable by traditional lithographic techniques. This can be exploited in bulk materials with applications such as nanoporous materials, nanochannels, optical waveguides or photonic crystals.[2–7] In thin films two dimensional patterns are formed, which can be used as nanoporous membranes, to fabricate magnetic or nanoelectrode arrays or as lithographic masks, transferring the block copolymer pattern to underlying substrates.[8–12]

Preferential segregation of one of the blocks on the surface or substrate imposes constraints to the film thickness, and in addition can influence orientation of the microdomains or even the microdomain morphology. The wetting behavior of symmetric block copolymers has been studied extensively both theoretically and experimentally.[13,14] A block with higher affinity for the substrate will form a preferential wetting layer, resulting typically in a parallel orientation of the microdomains. A free surface (such as air, vacuum or an inert gas) will in turn be enriched by the block with the lower surface free energy.[15,16] Preferential wetting of the block with the lowest surface tension at the free surface is observed regardless of the morphology (spherical, cylindrical or lamellar). Cylinders and lamellae typically orient parallel to the substrate, while spherical domains arrange in hexagonally packed 2D arrays. In case of asymmetric block copolymers, stacked layers of domains, cylindrical or spherical, are arranged in such a way that the domains are located over the inter-domain region of the adjacent layers.[17] In case of a strong interaction of one block with the substrate, a transition of cylindrical morphology to a lamellar one directly near the substrate was observed.[18,19]

As the thickness approaches few multiples of the microdomain spacing L_0, commensurability of the film thickness with the domain spacing becomes increasingly important. Deviations from the ideal film thickness that is dictated by preferential wetting constraints and the block copolymers intrinsic periodicity (L_0), have to be distributed over a smaller number of stacked layers of domains.[20] In confined and free-standing films the block copolymer may respond to incommensurate thicknesses with a transition in orientation of cylindrical domains from a parallel to a perpendicular one. This has been theoretically discussed in terms of the difference in free energy between the lattice period in the block copolymer thin film in parallel or perpendicular orientation compared to bulk morphology.[21] When the film thickness is less than the natural film thickness for one layer of domains, the parallel orientation would require too much elastic energy of the polymer chains. In this

case, perpendicular oriented domains ensure maintaining the equilibrium repeat distance, although the blocks do not comply with the preferential segregation dictated by the interfacial tensions. Further, a transition from a bulk packing of cylinders to a 'thin film' packing, or even a transition to spherical domains, and the contraction and expansion of the microdomain spacing, have been observed for film thicknesses incommensurate with multiples of L_0, despite the entropic penalties inherent in these structures.[22–24] A theoretical study in confined thin block copolymer films described similar transitions between lamellar and cylindrical microdomains, oriented either perpendicular or parallel, depending solely on the film thickness and the energetic preference of the surface for one of the blocks.[25]

In substrate supported films (with one free surface, such as air, inert gas or vacuum), in addition to a morphological transition, the formation of islands and holes is typically observed for decreasing film thickness, which enables the flow of material from one part of the film to form the commensurate film thickness in other areas of the film.[20,26,27]

As the preferential segregation of one or both blocks at the substrate and surface are of importance for the thin film morphology, a study of the wetting layers is highly valuable for understanding thin film morphology. Information on the wetting behavior of block copolymers can be gathered from techniques such as cross-sectional transmission electron microscopy (TEM),[17] X-ray or neutron reflectivity measurements or secondary ion mass spectrometry (SIMS).[18]

In case of PS-*b*-PFS a PFS brush layer is assumed to form at silicon substrates. An extensive study of substrate wetting in the case of PI-*b*-PFS has not been presented so far, but since we expect the polyisoprene block in our block copolymer to be more apolar, it is of interest to know if a similar case of a PFS brush layer on the substrate exists or if a different situation such as symmetric wetting by both blocks or asymmetric wetting by one of the blocks occurs.

In this chapter, the thin film morphology of asymmetric, sphere-forming PI-*b*-PFS block copolymers is discussed. The effect of substrate modifications is evaluated as a possible tool in manipulating the degree of order of the self-assembled microdomains. To complete the picture established from the thin film investigation, a detailed dynamic TOF-SIMS study of the substrate wetting layer in both PS-*b*-PFS and PI-*b*-PFS is discussed.

4.2 Thin film morphology

Long-range order

Thin films of the amorphous block copolymers on silicon (with a native oxide layer) were imaged by tapping mode AFM, showing a relatively well-ordered monolayer of PFS spheres, as shown in Figure 4.1. The figure shows a 1 μm^2 area of the film, where the methods to characterize the order, described in section 2.3.3, were employed. Both the Voronoi diagram representation (Figure 4.1C) and the pair-distribution function (Figure 4.1D) constructed from the AFM image confirm the good ordering quality and the relatively large single grain size. In comparison, the average grain size found in PS-*b*-PFDMS diblock copolymer thin films is typically around 280 nm.[28] Similar correlation length values were observed for PI-*b*-PFDMS diblock copolymers. PS-*b*-P2VP diblock copolymer thin films on flat silicon substrates showed single grain sizes of about 400 nm.[29] The increased correlation length for the amorphous PI-*b*-PFS block copolymer monolayers is likely a result of the high molecular mobility, allowing for the removal of point defects and grain boundaries by sphere rearrangement. The high molecular mobility might be due to the low glass transition temperature of the polyisoprene block and to a lowered glass transition temperature of the PFS block combined with the suppression of crystallization of the PFS domains. Figure 4.2 shows a well-ordered monolayer of organometallic spheres, with a single hexagonal grain extending over a large part of the scanned area of 2 μm.

The AFM images in Figure 4.1 and Figure 4.2 were taken at room temperature. The film surface was directly probed in the tapping mode. As discussed in section 3.2.2 the glass transition of the PFS block is lowered with increasing amounts of incorporated EM units. In block copolymers, the glass transition temperature of each block shifts towards the glass transition temperature of the other block: in case of PI-*b*-PFS the T_g of the PI shifts to higher temperature, while the T_g of the PFS shifts towards lower temperature. Both effects lower the effective glass transition temperature of the PFS block copolymer, resulting in a shift from a block copolymer with one rubbery block and one glassy block to a block copolymer with two rubbery blocks with increasing content of EM units. The contrast in the AFM height and phase images[30,31] therefore decreases significantly, frustrating direct imaging of the block copolymer film. In addition, due to the low glass transitions, the polymer film sticks easily to the AFM tips. To circumvent the decrease in imaging contrast, the films were exposed to an O_2–RIE treatment described by Lammertink *et al.*[32] Exposure to a mild O_2–RIE easily removed the organic PI phase by the bombardment of the oxygen species, while an iron oxide cap is formed at

Table 4.1: Characteristics of the polymers used in the thin film study and dynamic TOF-SIMS depth profiling measurements in this chapter.

	M_n [a]	M_w [a]	M_w/M_n [a]	PFS [b]	EM [c]	d [d]
	[kg/mol]	[kg/mol]		[vol%]	[mol%]	[nm]
IF35/11EM11	45	47	1.04	18	11	22.7
IF44/15EM14 [e]	58	62	1.06	20	14	25.1
IF47/13EM45	60	62	1.02	16	45	23.9
IF37/13EM100	50	51	1.03	20	100	21.3
SF65/20 [f]	84	89	1.07	20		39.2

[a]Measured by GPC, relative to polystyrene standards. [b]Calculated from ferrocenyl and polyisoprene ^{1}H NMR integrals. [c]Calculated from ethylmethyl and dimethyl ^{1}H NMR integrals. [d]First Bragg reflection peak measured by SAXS. The error is ± 0.1 nm. [e]Notation for PI-*b*-PFS, with the indication of the M_n of the PI and the PFS block, respectively, and EM mol%. [f]Notation for PS-*b*-PFS, with the indication of the M_n of the PS and the PFS block, respectively.

the surface of the PFS domains, protecting the material underneath. Thus, only oxidized PFS remains at the surface, which can be easily imaged as both height and phase images. The presence of iron enables one to use scanning electron microscopy (SEM) as direct imaging tool, since the electron density of the iron present from the PFS creates a scattering contrast.[33,34]

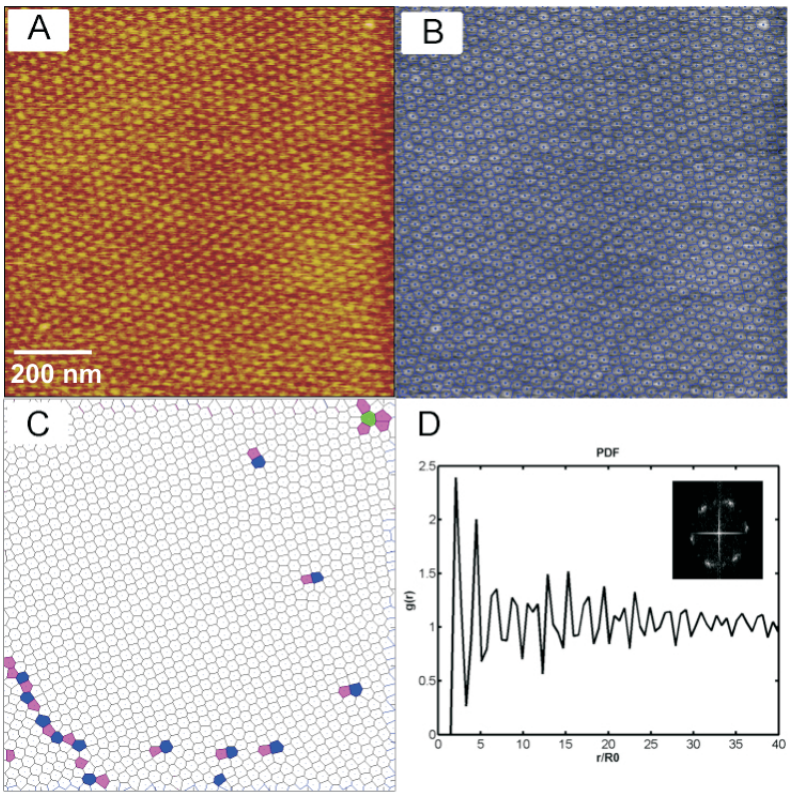

Figure 4.1: AFM-TM height image (z-range is 10 nm) of a 35 nm film of IF35/11EM11 (A). A sphere-finding algorithm was used to construct a representation with Voronoi diagrams (B,C) and a pair-distribution function (D). See also Figure C.3.

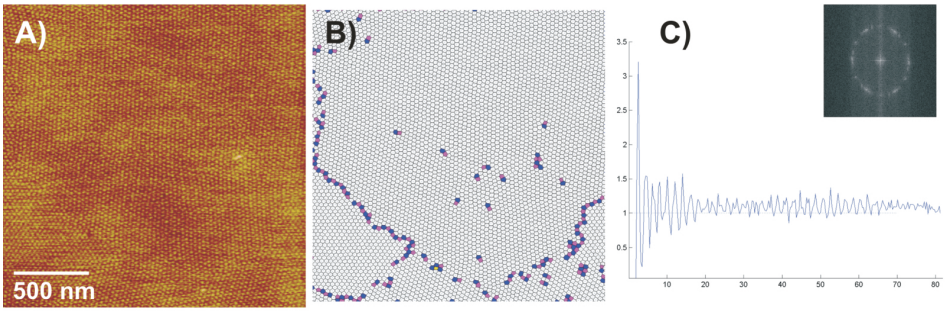

Figure 4.2: A) AFM-TM height image (z-range is 10 nm) of a film of IF35/11EM11 (thickness 35 nm), its Voronoi representation (B) and pair-distribution function, with the FFT shown in the inset (C). The film was annealed overnight at room temperature. See also Figure C.4.

Annealing strategy

Figure 4.3 shows a PI-*b*-PFS film after annealing at room temperature during 5 hours and during 24 hours, respectively, followed by O_2–RIE. Clearly, the order improves quite significantly when the domains have more time to equilibrate. Yet, the ordering kinetics is quite fast, having obtained considerable areas of ordered arrays within a few hours after spincoating. The degree of order after 24 hours is remarkably good, demonstrating almost one single grain over the 2 μm^2 scanned area.

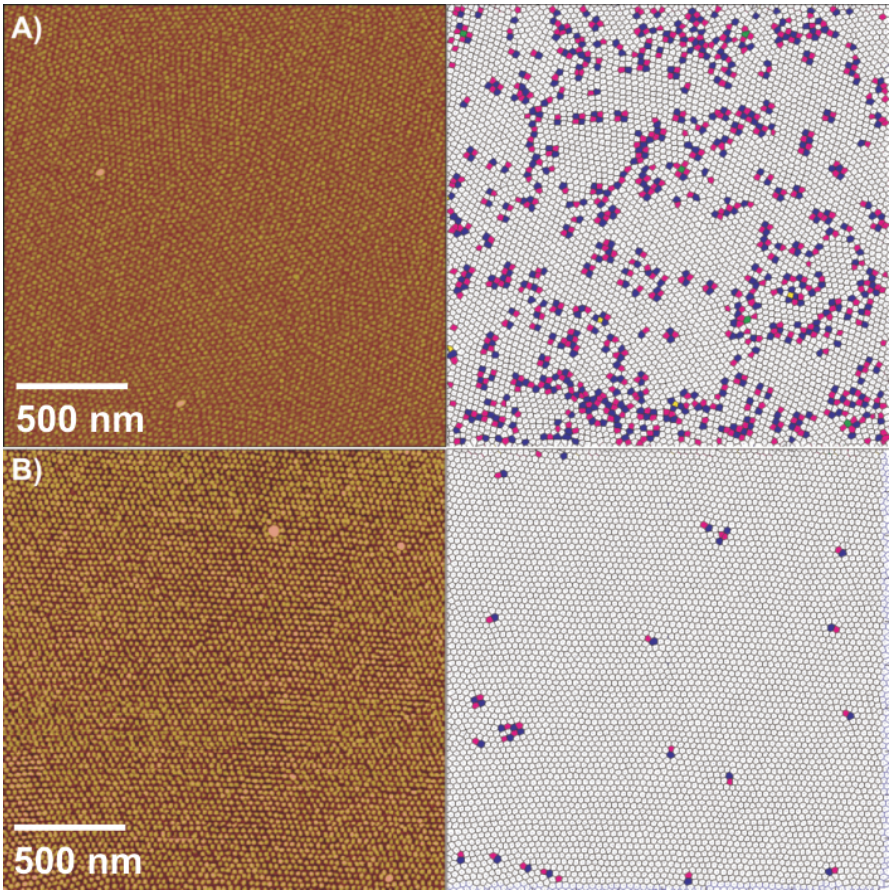

Figure 4.3: AFM-TM height image (*z*-range is 10 nm) of a thin film of IF35/11EM11 after O_2-RIE exposure and their Voronoi diagram representations, annealed for 5 hours (A), and annealed for 24 hours (B). See also Figure C.5.

An annealing time of 24 hours was found to be sufficient for establishing a high degree of order. Moreover, in this polymer, which contained 11

mol% of EM units, hardly any signs of crystallization were observed within this period, which was in agreement with the differential heat calorimetry experiments described in section 3.2.1. PI-*b*-PFSs with higher amounts of EM units were prepared to prevent any possible crystallization. Figure 4.4 shows such a film of PI-*b*-PFS, where the PFS block consists fully of EM units. This polymer, with similar molar mass and PFS volume fraction, displayed a very poor degree of order. Therefore, the long-range order observed for IF35/11EM11 cannot be accounted for solely by the increased mobility in the polymer. Thermodynamic considerations, such as the segregation strength, or surface wetting, are apparently of importance as well. The order-disorder temperature of IF37/13EM100 was found to be considerably lower compared to IF35/11EM11, which denotes that the segregation strength of the latter is higher. Therefore, the degree of order found in these thin films is governed by the segregation strength and the kinetic mobility of the copolymer chains.

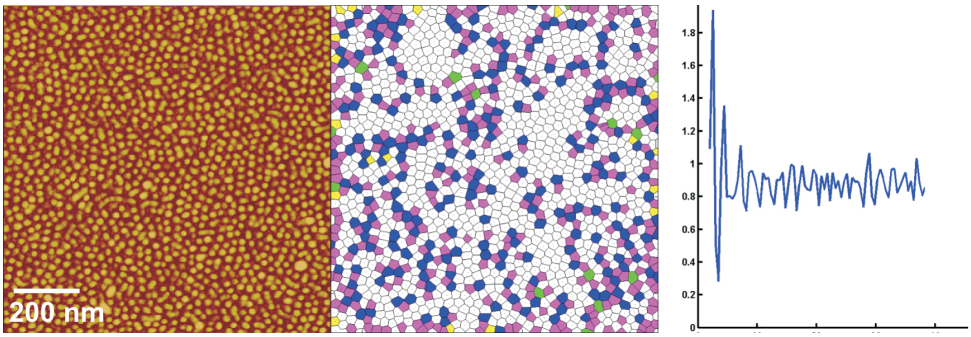

Figure 4.4: AFM-TM height image (*z*-range is 10 nm) of a IF37/13EM100 film with an initial film thickness of 29 nm (A), its Voronoi diagram representation (B), and the associated pair-distribution function (C). The degree of order is significantly lower compared to films of IF35/11EM11.

In section 3.3.2 an annealing strategy for bulk copolymer was discussed, which involved a brief heating above the melting temperature of PFS, followed by annealing for a short while at a temperature below the melting transition, but significantly above the glass transition. The same annealing procedure was applied to thin films, but instead of an increased order, as in case of the bulk sample followed with SAXS, the order was poor, even less well-defined than immediately after spincoating, as can be seen in Figure 4.5. Both spherical and wormlike microdomains were found in a 33 nm film of IF47/13EM45, which gives well-ordered spheres on annealing at room temperature. The presence of the substrate strongly slows down the diffusion of polymer chains.

The influence of substrate modifications on the wetting behavior of the block copolymer, and therefore possibly on the thin film morphology, was

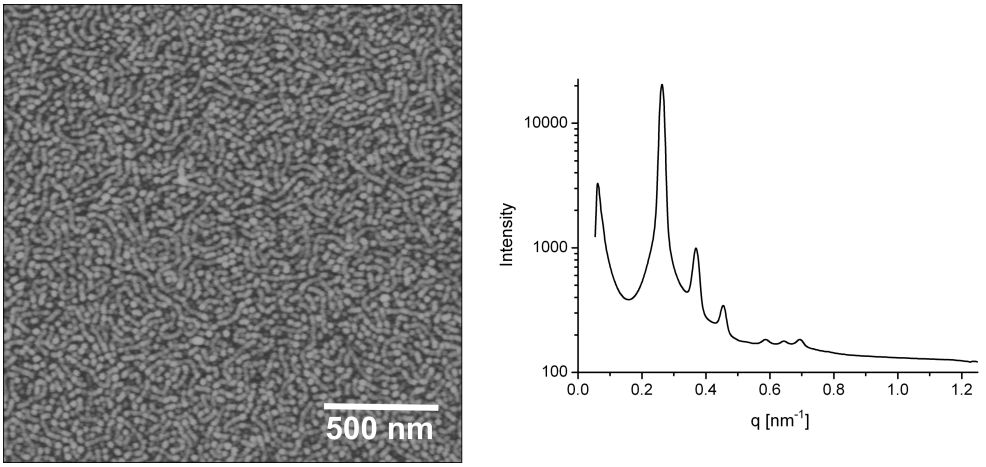

Figure 4.5: AFM-TM height image (*z*-range is 8 nm) of a thin film of IF47/13EM45 with an initial film thickness of 33 nm, after O_2–RIE exposure (left), and SAXS scattering profile of the bulk of IF47/13EM45, after annealing at 150 °C for 10 min and at 60 °C for 10 min (right).

explored. Films on passivated silicon showed no phase separated block copolymer morphology at all, but rather structures reminiscent of dewetting. On mica and alkyl modified substrates the block copolymer films did not dewet, but showed no or little order. The morphology on substrates with a thick oxide layer (> 180 nm) was similar compared to silicon with a native oxide layer, but the films were generally more susceptible to dewetting, and morphology transitions (from spheres to cylinders) were often observed.

4.3 Substrate wetting in PI-*b*-PFS and PS-*b*-PFS

Dynamic TOF-SIMS depth profiling measurements were performed on flat thin films of PS-*b*-PFS (SF65/20) and PI-*b*-PFS (IF45/15EM14) (see Table 4.1, the PFS was the minority phase and formed spherical domains arranged in a body centered cubic (BCC) phase in the bulk) on both silica and silicon (with a few nanometer thick native oxide layer) substrates. The thickness of the silica layer can influence the stability of a non-polar liquid on a solid substrate, as was demonstrated for PS on silicon with oxide layers of various thickness.[35] The interplay of both short- and long-range interfacial forces may influence the film stability in case of our non-polar block copolymer, and may also affect the substrate wetting.

In dynamic TOF-SIMS, bombardment-induced erosion from a sample sur-

face downwards occurs and one or more mass-over-charge intensities are recorded as a function of time, which can be converted to a concentration-depth profile.[36,38] By detecting the Fe ions that are present in PFS, the compositional depth profile in thin block copolymer films was obtained in terms of PFS volume fraction (ϕ_{PFS}), using Equation 4.1

$$\phi_{PFS}(z) = h f_{PFS} I(z) / \int_0^h I(z) dz \tag{4.1}$$

where h is the film thickness, f_{PFS} is the bulk volume fraction of PFS in the polymer, and $I(z)$ is the current of Fe ions incident onto the detector.

Figure 4.6 shows the PFS depth profile of the Fe ion intensity converted to ϕ_{PFS} in SF65/20 on Si and SiO_2, with film thicknesses of 69 nm and 215 nm, respectively.

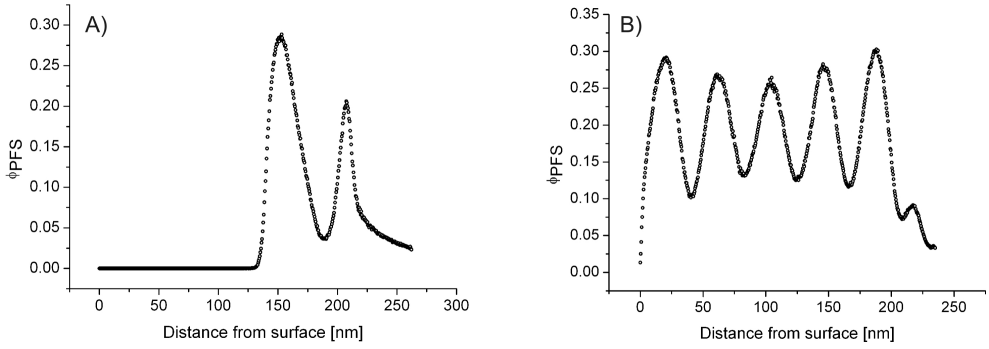

Figure 4.6: Depth profiles established with dynamic TOF-SIMS , represented as the PFS volume fraction, for SF65/20. A) 69 nm film on silicon. B) 215 nm film on silicon oxide.

The free surface was determined from the Au–signal (not shown here) of a thin gold layer evaporated on the polymer surface. The first maximum of ϕ_{PFS} is located at a distance from the surface, denoting the first layer of spherical domains located within the film. This peak in ϕ_{PFS} corresponds to a layer of PFS spherical domains with a half-peak width of 30 nm, which we take as the domain diameter. The next maximum in ϕ_{PFS} is located directly at the silicon substrate. The width of this PFS layer is 13 nm, which is approximately one-half of the domain diameter. The PFS volume fraction at the substrate is considerably lower compared to the layer of spheres. These results indicate that in PS-*b*-PFS block copolymer films the PFS preferentially resides at the silicon substrate, whereas the PS exhibits an affinity for the free surface. Figure 4.6B shows a similar trend of a somewhat thicker PS-*b*-PFS

film, but on a silicon oxide substrate. At the substrate, a PFS layer is present with one-half the thickness of the domain size within the specimen. The oscillating signal clearly indicates layers of spherical domains ordered laterally with respect to the substrate over the entire analysis area of 30 μm^2. There are five layers of spherical PFS domains present in this film with an average domain diameter of 22 nm. The layer periodicity (l), that is the spacing between two adjacent maxima in ϕ_{PFS}, is 42 nm. This corresponds well with the spacing of 39.2 nm for the first allowed reflection in the BCC structure (l_{BCC}), which is the (110) plane, that was determined by small-angle X-ray scattering (SAXS). Similar results where spherical domains were found to order on the substrate with the (110) plane parallel to the substrate were found by others for PS-*b*-PVP.[37] In Table 4.2, the average domain diameter ($2r$) and layer periodicity for the films are summarized.

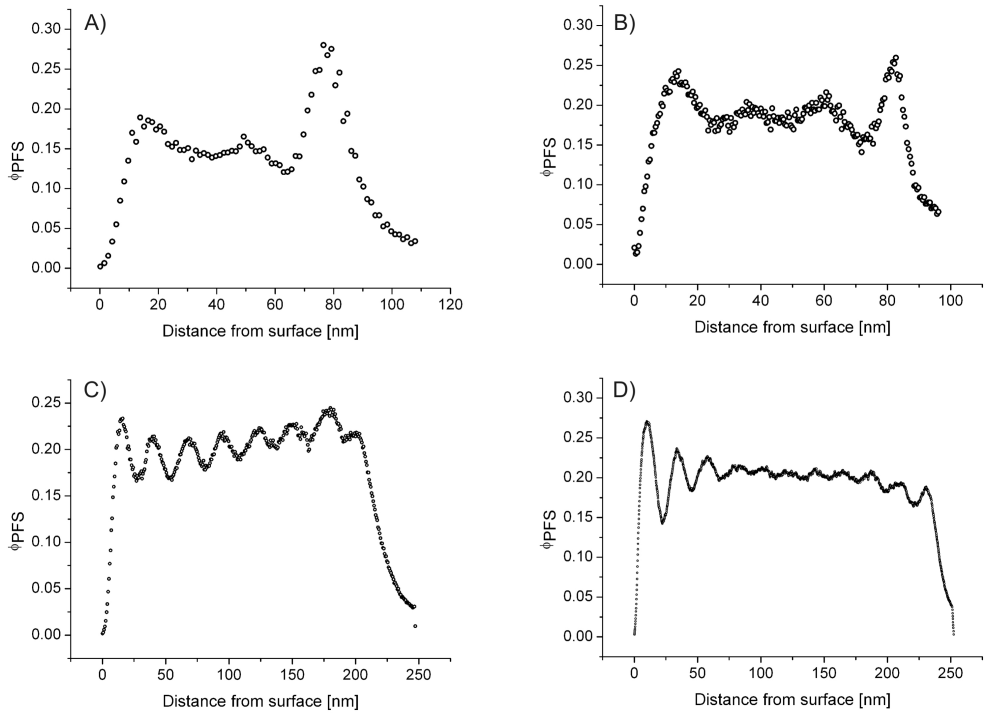

Figure 4.7: Dynamic TOF-SIMS depth profiles of IF46/15EM14, converted to the PFS volume fraction, for films of A) 73 nm on silica, B) 84 nm on silicon, C) 204 nm on silicon and D) 233 nm on silica.

Figure 4.7 shows the volume fraction of PFS in thin films of IF46/15EM14 on silicon and silica. First, the depth profile of the PI-*b*-PFS has a weaker variation in the PFS volume fraction ($\triangle\phi_{PFS}$) than observed

for PS-*b*-PFS. The weaker oscillation is likely due to the weaker phase segregation in PI-*b*-PFS (see section 3.3.2). From contact angle measurements it is known that PI wets the air interface.[38] In all films, maxima in the PFS volume fraction are found at the substrate interface, and there is no noticeable difference in wetting behavior on silicon or silicon oxide. Contrary to the copolymer film with a polystyrene majority phase, there is no notable decrease in PFS volume fraction directly near the substrate, nor are the widths of these peaks smaller compared to other depth values in the plots. Comparison of the dynamic TOF-SIMS data of SF65/20 and IF46/15EM14 leads us to conclude that while in PS-*b*-PFS films a layer of PFS is present at the substrate, due to the significant decrease in PFS volume and layer thickness at the surface, both blocks are present at silicon or silica substrates in the case of PI-*b*-PFS. The presence of both blocks directly at the substrate in PI-*b*-PFS is supported by SEM images of O_2-RIE exposed films on substrates with 100 nm deep grooves, where domains are observed directly on the groove walls (as will be discussed in Chapter 5.

Although the manner in which PFS is present at the substrate differs for PS-*b*-PFS and PI-*b*-PFS, the natural film thickness h_0 that is commensurate with the periodicity is consistent for both polymers with asymmetric wetting for surface and substrate, and is given by

$$h_0 = [(n-1) + 0.5]\, l_{(\mathrm{BCC})} \tag{4.2}$$

where n is an integer. The number of layers found by dynamic TOF-SIMS in the PI-*b*-PFS thin films and the corresponding average layer thickness and domain sizes are given in Table 4.2. First, the deviation from the natural film thickness is less than 1% for the thicker film of SF65/20, which implies that either the film thickness was coincidentally very well chosen, or that the copolymer responds easily to small deviations from the natural film thickness by chain stretching or compression, distributed throughout the entire film. For PI-*b*-PFS films of four layers or more (Figure 4.7B-D) the average layer thickness corresponds well with the equilibrium bulk value $l_{(\mathrm{BCC})}$ for the (110) plane in a BCC morphology, which was determined by SAXS to be 25.1 nm.

The planar (110) oriented BCC morphology found in dynamic TOF-SIMS does not correspond to the in-plane morphology of spheres in a monolayer, which are hexagonally packed (HP), as can be easily imaged, for instance by atomic force microscopy (AFM). The (110) plane of a BCC structure is a distorted hexagonal packing of domains. The (111) plane in FCC and the (111) plane in BCC exhibit hexagonal packing of domains. However, if one assumes either one of these planes to be parallel to the substrate, the corresponding layer periodicities are not compatible with the dynamic TOF-SIMS data.

Based on our dynamic TOF-SIMS results, we explain the discrepancy with the HP monolayer and the BCC bulk morphology by a rearrangement of the microdomains in thin films, a similar process to surface relaxations and relocations in atomically thin films of metals.[39] The first layer of domains forms an HP array of domains. When a second or even third layer of domains is present, a repositioning towards a more BCC-like morphology occurs, presumably via a base-centered orthorhombic arrangement. The position of the domains in both layers is shifted slightly with respect to the hexagonal packing. In the subsequent layers of domains, the HP morphology is abandoned and a BCC structure is adopted. Our results of a larger layer-spacing in thinner films (see Table 4.2) agree well with such a transition. A more close-packed arrangement of microdomains in a monolayer, as is the case for HP arrays compared to a BCC arrangement, will necessarily induce a mechanical stress normal to the plane of organization on the chains, which will result in chain stretching and larger domain sizes and interdomain spacings. This is supported by the film thickness of 41 nm for one monolayer of domains ($n = 1$) in PI-*b*-PFS, which is almost three times the calculated h_0, and close to h_0 for 1.5 layers ($n = 2$). However, just one layer of domains exists directly at the substrate ($n = 1$).[1] Similarly, the thickness for the monolayer in SF65/20 deviates by 17% from the natural film thickness. For films of more than one monolayer, a positional reorganization of the domains from HP to BCC phase induces most probably chain stretching both in-plane and out-of-plane. In the film of three layers of domains of IF46/15EM14 (Figure 4.7A) there is a considerable difference in the distance between adjacent layers and the bulk value. Moreover, the first layer directly next to the substrate is 27 nm, slightly larger than ($l_{(110)}$), while the second layer is 34 nm. The increase in domain sizes, as well as the increased layer thickness in the thinner films of both SF65/20 and IF46/15EM14 compared to the bulk, support our idea of a transition in the morphology going from films of a few layers of microdomains to thicker films in the copolymer studied. In thicker films, this difference in layer periodicity throughout the film is absent. Clearly, the rearrangement from HP to BCC strongly affects the orientation in films up to three layers in this polymer, but for thicker films, the BCC (110) morphology planar to the free surface dominates the order down to the substrate.

Small variations in periodicity and domain size are observed in the three thicker polyisoprene copolymer films. In case of incommensurability of the film thickness with the periodicity of the block copolymer the formation of islands or holes is typically observed. However, for some copolymer systems, deviations from the ideal domain size and periodicity occur in films of more

[1] The existence of more than one layer of domains would result in superimposed images of the layers of domains after O_2-RIE.

Table 4.2: Number of layers (n) observed with dynamic TOF-SIMS and the deviation from the natural film thickness (h_0) for asymmetric wetting of the substrate and surface.

	h[nm]	n	l [nm]	$2r$ [nm]	h_0 [nm]	$(h-h_0)/h_0$[%]
SF65/20	69	1	53	30	59	17
	215	6	42	22	216	< 1
IF46/15EM14	73	3	31	15	63	16
	84	4	23	11	88	5
	204	8	26	14	188	9
	233	11	24	12	263	8

than a few layers of domains, which is apparently less unfavorable than the rupture of the film.[40] This seems to be the case in thin films of PI-*b*-PFS block copolymer as well, which seems to exhibit a large degree of elasticity, as appears from the deviations from the natural thickness given in Table 4.2, ranging from 5 to 9%.

For the film thickness of 233 nm (Figure 4.7D) layers of domains are present both near the surface and the substrate, but the ordered layering does not propagate to the middle of the film. Since the SAXS scattering profile of a bulk specimen of this copolymer results in sharp, well-defined higher order peaks, it appears unlikely that this is due to the absence of long-range order. Further, since the two blocks of the copolymer are above the T_g, rendering the chains mobile, the absence of order in the film interior does not seem likely to be caused by kinetic trapping. Therefore, the absence of order most likely is the result of frustration due to incommensurability of the block copolymer repeat length with the film thickness. The surface and substrate strongly direct the position of the layers of domains directly next to the interfaces, and the frustration is spread over the interior layers of domains.

4.4 Conclusions

In thin films, amorphous low-T_g diblock copolymers self-assembled to form well-ordered monolayers of PFS spheres, with single grain sizes larger than 1 μm x 1 μm, without thermal annealing. This significant increase in correlation length with respect to PS-*b*-PFDMS or PI-*b*-PFDMS block copolymers renders the amorphous diblock copolymers highly useful as self-assembling templates for nanolithography or other functional nanostructures. The high degree of order is attributed to a combination of chain mobility, segregation strength and substrate and surface wetting. A study on the substrate wetting layer revealed that the domain diameters and layer thickness in thin films of PFS copolymer with a polystyrene or polyisoprene block were larger in films consisting of one to three layers of spherical domains, indicating chain stretching normal to the substrate. This stretching is thought to originate from a transition in microdomain packing from HP arrays of domains in a monolayer, probably via a base-centered orthorhombic to a BCC arrangement. In thicker films, a BCC phase is adopted with the (110) plane parallel to the surface, which persists through the entire film, including the three layers directly at the substrate. Deviations from the natural film thickness, dictated by the asymmetric wetting conditions of substrate and surface, are distributed over the layers of domains. Especially in case of the polyisoprene copolymers, a highly elastic response to incommensurability was observed, rather than the typical observed island or hole formation. Both blocks of PI-*b*-PFS were found at the substrate, while in PS-*b*-PFS the PFS preferentially segregated at the substrate.

4.5 Experimental

PI-*b*-PFS block copolymers were synthesized as described in section 3.5. PS-*b*-PFS was synthesized by sequential anionic polymerization, as described for the synthesis of PI-*b*-PFS. Styrene polymerizations in ethylbenzene were initiated by *n*-butyllithium. After completion of the styrene block, [1]dimethylsilaferrocenophane was added, followed by THF, for the formation of the PFS block. Degassed methanol was added after 1 h. Passivated silicon substrates were prepared by a 1 min dip in hydrofluoric acid, and subsequent rinsing with H_2O. Block copolymer films were immediately prepared on the passivated substrates. Alkyl modified substrates were prepared by overnight vapor phase silanization of freshly cleaned silicon wafers with octadecyltrichlorosilane (OTS), or by storing the substrates overnight in a toluene solution of OTS (*ca.* 0.1 ml in 1-2 ml toluene) under a nitrogen atmosphere. Thin films were spin-coated from 1 wt% PI-*b*-PFS solution in toluene on flat or topographically

patterned silicon substrates. Cleaning of the substrates and coating of the films were performed in a clean room. Film thicknesses ranged from 25 nm to 40 nm, measured by ellipsometry. The films were annealed at room temperature for the desired time period and subsequently either imaged directly by AFM in the tapping mode (height and phase images), or exposed to an oxygen plasma in a reactive ion etching (O_2-RIE) setup, carried out in an Elektrotech PF 340 apparatus. The pressure inside the etching chamber was 10 mTorr, the substrate temperature was set at 10 °C, and an oxygen flow rate of 20 cm^3/min was maintained. Power was set at 75 W, and the thin films were exposed to the O_2-plasma for 10 s. The morphology of the thin films and the etched patterns was studied using a NanoScope III multimode atomic force microscopy (AFM) instrument (Digital Instruments/Veeco), operated in the tapping mode, and by scanning electron microscopy (SEM) (LEO 1550 FEG microscope). Dynamic SIMS measurements were performed using a TOF-SIMS IV, with a 2 keV 20 nA Ar^+ sputtering beam. Analysis (using non-interlace mode in case of SiO_2 substrates and interlace mode on Si substrates) was done with a 10 keV Ar^+ with an additional $^{18}O_2$ flooding. Positive ions of H, CH, O, Na, Si, SiC and Fe were monitored as a function of time. The sputter beam was rastered over a 500 μm^2 area, the analysis area was 30 μm^2 centered within the sputtered area. Cooling to -100 °C was possible with a cooling device in the TOF-SIMS instrument. Films of PS-*b*-PFS for dynamic TOF-SIMS measurements were annealed at 150 °C for two days. To identify the wetting layer at the air-interface, a 5 nm gold layer was evaporated on the annealed film, on top of which a polystyrene sacrificial film was placed. This PS film was prepared prior by spincoating on a clean Si wafer and floated on H_2O, and was picked up by the sample from the water surface. The gold layer indicates the start of the film boundary during sputtering and the sacrificial layer allows one to determine the sputter rate and to stabilize the sputter beam. The PI-*b*-PFS films were cooled to -100 °C (well below the T_g of the PI block) during sputtering, to ensure the polymer being below the glass transition to prevent rearrangements during sputtering. Prior to TOF-SIMS measurements on the films, the films were carefully checked (by optical microscopy and AFM analysis) for the absence of terraces.

Bibliography

[1] Bates, F. S. and Fredrickson, G. H., *Annu. Rev. Phys. Chem.*, 1990, 41, 525-557.

[2] Zhao, D., and Feng, J., Huo, Q., Melosh, N., Fredrickson, G. H., Chmelka, B. F. and Stucky, G. D., *Science*, 1998, 279, 548-552.

[3] Templin, M., Franck, A., Du Chesne, A., Leist, H., Zhang, Y., Ulrich, R., Schadler, V. and Wiesner, U., *Science*, 1997, 278, 1795-1798.

[4] Yang, P., Wirnsberger, G., Huang, H. C., Cordero, S. R., McGehee, M. D., Scott, B., Deng, T., Whitesides, G. M., Chmelka, B. F., Buratto, S. K. and Stucky, G. D., *Science*, 2000, 287, 465-467.

[5] Fink, Y., Urbas, A. M., Bawendi, M. G., Joannopoulos, J. D., and Thomas, E. L., *J. Lightwave Technol.*, 1999, 17, 1963-1969.

[6] Hashimoto, T., Tsutsumi, K. and Funaki, Y., *Langmuir*, 1997, 13, 6869-6872.

[7] Hamley, I. W, *Soft Matter*, 2005, 1, 36-43.

[8] Park, M., Harrison, C., Chaikin, P. M., Register, R. A. and Adamson, D. H., *Science*, 1997, 276, 1401-1404.

[9] Harrison, C., Dagata, J. A. and Adamson, D. H., In *Developements in Block Copolymer Science and Technology*, Hamley, I. W., Ed., Wiley, Chichester etc., 2004, 295-323.

[10] Park, M., Chaikin, P. M., Register, R. A. and Adamson, D. H., *Appl. Phys. Lett.*, 2001, 79, 257-259.

[11] Park, C., De Rosa, C. and Thomas, E. L., *Macromolecules*, 2001, 34, 2602-2606.

[12] Park, C., Yoon, J. and Thomas, E. L., *Polymer*, 2003, 44, 6725-6760.

[13] Krausch, G., *Mater. Sci. Eng.*, 1995, R14, 1-94.

[14] Russell, T. P., Menelle, A., Anastasiadis, S. H., Satija, S. K. and Majkrzak, C. F., *Macromolecules*, 1991, 24, 6263-6269.

[15] Ragosti, A. K. and St. Pierre, L. E., *J. Colloid Interface Sci.*, 1969, 31, 168-175.

[16] Coulon, G., Russell, T. P., Deline, V. R. and Green, P. F., *Macromolecules*, 1989, 22, 2581-2589.

[17] Henkee, C. S., Thomas, E. L. and Fetters, L. J., *J. Mater. Sci.*, 1988, 23, 1685-1694.

[18] Liu, Y., Zhao, W., Zheng, X., King, A., Singh, A., Rafailovich, M. H., Sokolov, J., Dai, K. H., Kramer, E. J., Scwarz, S. A., Gebizlioglu, O. and Sinha, S. K., *Macromolecules*, 1994, 27, 4000-4010.

[19] Turner, M. S., Rubinstein, M. and Marques, C. M., *Macromolecules*, 1994, 27, 4986-4992.

[20] Coulon, G., Collin, B., Ausserre, D., Chatenay, D. and Russell, T. P., *J. Phys. (Paris)*, 1990, 51, 2801-2811.

[21] Suh, K. Y., Kim, Y. S. and Lee, H. H., *J. Chem. Phys.*, 1998, 108, 1253-1256.

[22] Lambooy, P., Russell, T. P., Kellogg, G. J., Mayes, A. M., Gallagher, P. D. and Satija, S. K., *Phys. Rev. Lett.*, 1994, 72, 2899-2902.

[23] Koneripalli, N., Singh, N., Levicky, R., Bates, F. S., Gallagher, P. D. and Satija, S. K., *Macromolecules*, 1995, 28, 2897-2904.

[24] Radzilowski, L. H., Carvalho, B. L. and Thomas, E. L., *J. Polym. Sci., Part B: Polym. Phys.*, 1996, 34, 3081-3093.

[25] Huinink, H. P., Brokken-Zijp, J. C. M., Van Dijk, M. A. and Sevink, G. J. A., *J. Chem. Phys.*, 2000, 112, 2452-2562.

[26] Grim, P. C. M., Nyrkova, I. A., Semenov, A. N., Ten Brinke, G. and Hadziioannou, G., *Macromolecules*, 1995, 28, 7501-7513.

[27] Heier, J., Sivaniah, E. and Kramer, E. J., *Macromolecules*, 1999, 32, 9007-9012.

[28] Cheng, J. Y., Ross, C. A., Smith, H. I. and Vancso, G. J., *Appl. Phys. Lett.*, 2002, 81, 3657-3659.

[29] Segalman, R. A., Hexemer, A., Hayward, R. C. and Kramer, E. J., *Macromolecules*, 2003, 36, 3272-3288.

[30] Leclere, P., Lazzaroni, R., Bredas, J. L., Yu, J. M., Dubois, P. and Jerome, R., *Langmuir*, 1996, 12, 4317-4320.

[31] Morkved, T. L., Lopes, W. A., Hahm, J., Sibener, S. J. and Jaeger, H. M., *Polymer*, 1998, 39, 3871-3875.

[32] Lammertink, R. G. H., Hempenius, M. A., Chan, V. Z. -H., Thomas, E. L. and Vancso, G. J., *Chem. Mater.*, 2001, 13, 429-434.

[33] Schwark, D. W., Vezie, D. L., Reffner, J. R., Thomas, E. L. and Annis, B. K., *J. Mater. Sci. Lett.*, 1992, 11, 352-355.

[34] Vezie, D. L., Thomas, E. L. and Adams, W. W., *Polymer*, 1995, 36, 1761-1779.

[35] Seemann, R., Herminghaus, S. and Jacobs, K., *Phys. Rev. Lett.*, 2001, 24, 5534-5537.

[36] Zalm, P. C., *Mikrochim. Acta*, 2000, 132, 243-257.

[37] Yokoyama, H., Kramer, E. J., Rafailovich, M. H., Sokolov, J. and Schwarz, S. A., *Macromolecules*, 1998, 31, 8826-8830.

[38] Lammertink, R. G. H., Hempenius, M. A. and Vancso, G. J., *Langmuir*, 2000, 16, 6245-6252.

[39] Morrison, S. R., *The Chemical Physics of Surfaces*, Plenum Press, New York and London, 2nd Ed., 1990.

[40] Yokoyama, H., Mates, T. E. and Kramer, E. J., *Macromolecules*, 2000, 33, 1888-1898.

CHAPTER 5

Graphoepitaxy

Topographic substrate features can induce ordering of block copolymer microdomains, a process that is called graphoepitaxy. This chapter describes the graphoepitaxial alignment of PI-*b*-PFS domains with the aim of achieving long-range order with positional control. For this purpose, the ordering of PI-*b*-PFS block copolymers in grooves of various geometry and size was studied. On silicon substrates, the position of the domains of the minority PFS phase directly near the sidewalls is fixed by the symmetric wetting condition, directing the position of domains located at larger distances from the sidewalls. Successful positioning of the block copolymer spheres in linear and hexagonal grooves was achieved in up to 1.3 μm wide grooves, whereby the hexagonal grooves demonstrated 2D alignment. In circular pits, the graphoepitaxial effect was absent. The domains rather formed one single grain than follow the curvature imposed by the groove edge. The strain imposed by curved sidewalls was absorbed by expansion or compression of the domains directly near the edge.

*Parts of this chapter are accepted for publication in *Small* as: Roerdink, M., Hempenius, M. A., Gunst, U., Arlinghaus, H. F. and Vancso, G. J., *Substrate wetting and topologically induced ordering of amorphous PI-b-PFS block copolymer domains.*

5.1 Introduction

Control over the orientation and registry of block copolymer domains is most important for applications such as high density data storage,[1,2] photonic crystals or waveguides.[3] A variety of methods have been explored over the last years to enlarge the grain sizes in block copolymer thin films, such as using substrate interactions,[4,5] directional solvent evaporation[6–8] and crystallization[9] or topographical patterns.[10–14] The use of substrate topographic features to induce positional ordering has been referred to as graphoepitaxy.

The term graphoepitaxy was first applied to the ordering in thin films of solid materials and mesophases, such as liquid crystals, induced by artificial surface patterns.[15–17] Substrate induced ordering was recognized to consist of two categories: one that depends on orienting faceted microcrystals that are mobile within the medium of crystallization and one consisting of translationally immobile material.[17] The main difference between both categories is that in the first case of mobile microcrystals, the surface grating structures should be larger than the microcrystalline size. In case of a material with immobile grains the spatial period of the substrate structures should be smaller than the grain size that would naturally develop. The orientation can occur by for instance nucleation, during film growth (through preferential growth or reorientation during growth, or coalesence) or by solid state recrystallization. The mechanism behind the ordering effect was based upon considerations of minimization of the interfacial tension. In case of for instance liquid crystals, the interfacial tension is anisotropic, therefore a minimum in interfacial free energy and elastic-strain energy corresponds to a preferred orientation.

Topographically induced order of the 'mesophase' block copolymer domains has been first described by Kramer and coworkers, who demonstrated surface induced ordering in thick films of PS-*b*-PVP up to microns perpendicular to the surface,[18] although the in-plane ordering was short-ranged. In-plane order was shown to be obtained using topographically structured substrates on which thin films consisting of one monolayer of domains were cast, resulting in single grains of domains in the wells and on top of the mesas that extended over microns.[11,19,20] This work of Segalman, Kramer *et al.* on the templating effect of edges on domain ordering in block copolymer thin films was the first example of graphoepitaxy with amorphous block copolymers. Another study of graphoepitaxy was reported by Cheng, Ross, Vancso *et al.*, aligning domains of poly(ferrocenylsilane) in a polystyrene matrix.[21,31] The domains registered with the groove edges up to 12 rows, after which the order broke down. Incommensurability of the groove width with the ideal number of rows was adjusted by changes in the inter-row spacing (stretching or compressing) or changes in domain size directly near the edges. The regis-

tration of domains in grooves with modulated widths was described in terms of elastic strain,[22] which enabled prediction of the occurrence of a constant number of rows despite groove width modulations as well as the controlled addition or omission of one or more rows, for given groove widths. Although the system described by Cheng has a high tolerance to imperfections in templating geometry or edge roughnesses,[22,23] a maximum number of 11 to 12 rows could be successfully guided by templated grooves.

The orientational effect of silica substrates on spherical domains in thin films of PS-*b*-PFS was attributed to the presence of a PFS brush layer at the substrate, which was suggested by dynamic SIMS data and by the decrease of groove width by twice a brush layer thickness after spincasting a film.[21,24] The difference in substrate wetting between PS-*b*-PFS and PI-*b*-PFS as discussed in Section 4.3 presents a qualitatively different situation for the graphoepitaxial templating of domains along edges with PI-*b*-PFS block copolymer. The natural occurring grain size in PI-*b*-PFS is significantly larger compared to the grain size in for instance PS-*b*-PFS. Since achieving alignment by graphoepitaxy is limited by the natural grain size, the topographically induced order in PI-*b*-PFS is studied since one would expect a significant increase in the area that can be aligned successfully.

5.2 Graphoepitaxy with PI-*b*-PFS

Several experiments on graphoepitaxy with PI-*b*-PFS block copolymers were carried out to study the effect of pit geometry. Substrates with linear, circular and hexagonal grooves and pits with dimensions of approximately 300 nm, 500 nm, 800 nm, 1 μm and 1.5 μm were used, prepared by E-beam lithography. In Figure 5.1, a typical substrate is shown. Three amorphous PI-*b*-PFS block copolymers were used. The characteristics of these polymers are listed in Table 5.1.

The substrate wetting differs between PS-*b*-PFS and PI-*b*-PFS, as discussed in Section 4.3, and therefore the graphoepitaxy alignment of the microdomains in PI-*b*-PFS block copolymers was studied next. The polymer at the mesa directly next to the side-walls flows into the grooves immediately after spincoating. The area around the grooves is therefore depleted from polymer, except for a brush layer of adhered chains, as can be seen from remaining contrast in both SEM as AFM phase images. Probably, the rapid transport of material into the grooves proceeds over this adhered brush.[25] This necessitates adjusting the amount of material spincoated with the groove depth and groove width.

Figure 5.2 shows three linear grooves with a depth of 50 nm. The initial film thickness of the block copolymer was about 30 nm. In the smallest groove

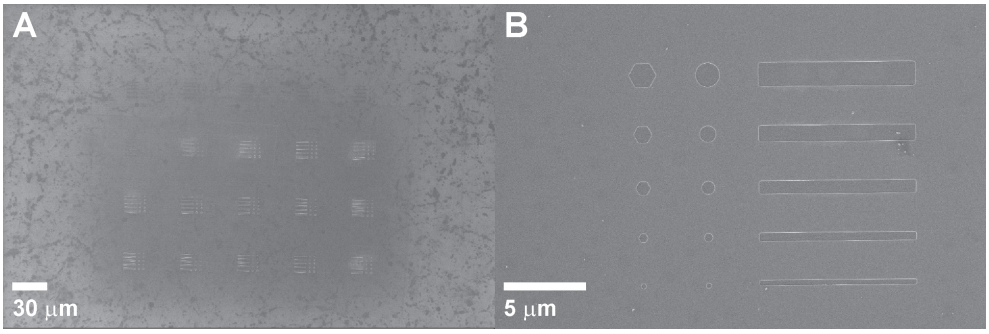

Figure 5.1: SEM images of a typical substrate patterned by E-beam lithography. A pattern consisting of circles, hexagons and lines with different dimensions is written 10 or more times on a resistive resin layer and subsequently developed and etched into a silicon wafer (A). The groove widths are typically around 300 nm, 500 nm, 800 nm, 1 μm and 1.5 μm (B). See also Figure C.6.

Table 5.1: Characteristics of the polymers based on GPC and ^{1}H NMR analysis.

	$M_n{}^a$ [kg/mol]	$M_w{}^a$ [kg/mol]	$M_w/M_n{}^a$	PFS^b [vol%]	EM^c [mol%]
IF35/11EM11^d	45	47	1.04	18	11
IF44/15EM14^d	58	62	1.06	20	14
IF47/13EM45^d	60	62	1.02	16	45

^{a}Measured by GPC, relative to polystyrene standards. ^{b}Calculated from ferrocenyl and polyisoprene ^{1}H NMR integrals. ^{c}Calculated from ethylmethyl and dimethyl ^{1}H NMR integrals. ^{d}Notation for PI-*b*-PFS, with the indication of the M_n of the PI and the PFS block, respectively, and EM mol%.

(top) directly near the groove edges, the domains are of irregular shape and in close proximity, even merging together to wormlike domains. Away from the edges, the domains are spherically shaped and hexagonally packed, and the rows are aligned with the groove walls. Too much material has accumulated directly near the walls. In the wider groove (middle), this is not observed, but the domains in the middle of the groove are smaller and spaced further away from each other. In the widest grooves (bottom), the groove could not be filled completely with a monolayer of domains and on the left side of the image a hole is observed in the middle of the groove. In hexagonal and circular

pits the sidewall-to-volume ratio is higher than in the case of linear grooves, resulting rather in overfilled than underfilled pits, as in case of linear grooves.

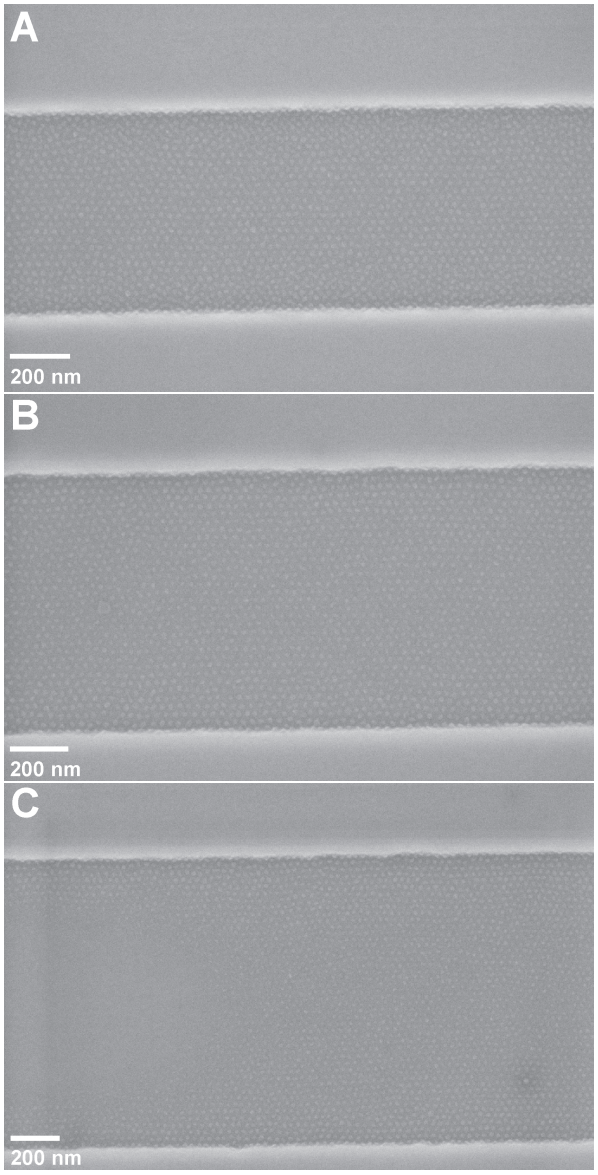

Figure 5.2: SEM images of IF35/11EM11 block copolymer in linear grooves of 800 nm (top), 1 μm (middle) and 1.3 μm (bottom) width. The films were exposed to an O_2-RIE plasma before imaging. See also Figure C.7.

Figure 5.3 shows PFS domains in linear grooves after O_2-RIE exposure,

to remove the organic PI phase. There are 38 rows accommodated in the 1.1 μm wide groove, aligned parallel to the groove edge. In grooves of up to 1.3 μm, alignment is observed, but in wider grooves the alignment is lost, as in the 2.2 μm wide groove in Figure 5.3 (right). The number of rows aligned in the grooves exceeds by far the number of rows that could be aligned in case of PS-*b*-PFS (12 rows[22]). The width of the grooves that can successfully guide block copolymer domains for PI-*b*-PFS is comparable to the grain size of the polymer on flat substrates, as expected. Therefore, there is apparently no qualitative difference in topographically induced ordering of block copolymer domains based on symmetric or asymmetric wetting of the substrate. A recent work on cylindrical microdomains in a PS-*b*-PMMA block copolymer film on topographically patterned substrates that were covered by a neutral brush agrees with our findings.[14]

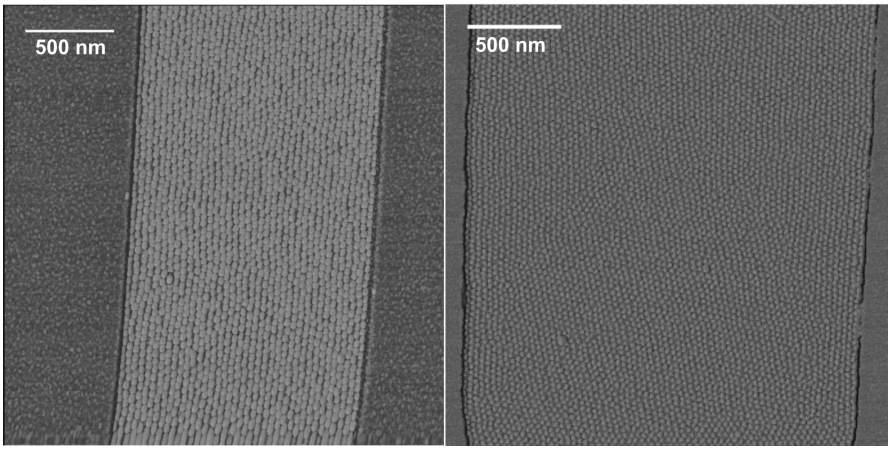

Figure 5.3: AFM-TM phase images (*z*-range is 30°) of IF35/11EM block copolymer in a linear groove of 1.1 μm (left), with all 38 rows of domains aligned parallel to the groove edges, and in a 2.2 μm wide groove with no particular alignment of the domains (right). The films were exposed to an O_2-RIE plasma before imaging.

Figure 5.4 shows two rectangular groove endings. Next to all three side-walls, rows align parallel to the edge, but the two parallel side-walls dominate the overall ordering. The 90° angle is incommensurate with the hexagonal packing of domains. The result is a semicircular row of dislocations perpendicular to the grooves length, located close to the end of the 300 nm wide groove. The row of dislocations was found to advance more to the interior of the groove for wider grooves (not all shown here). The grain boundary formed by the dislocations absorbs internal stresses induced by the incommensurability between the 90° sidewall and the block copolymer lattice and tends to

minimize its length, resulting in the semi-circular shape observed.

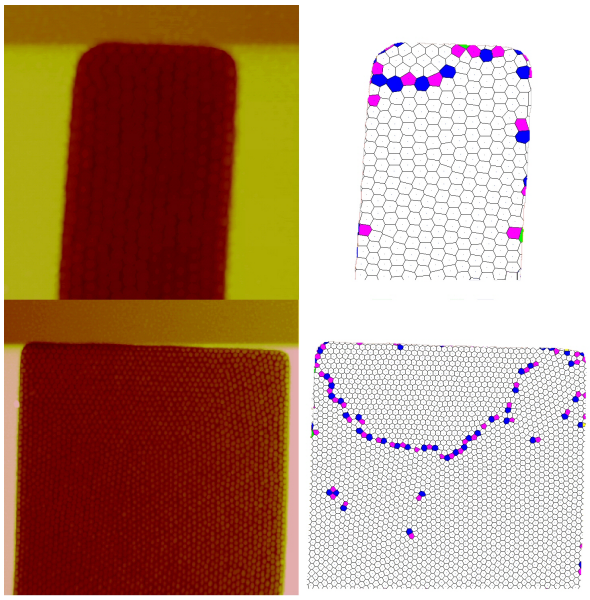

Figure 5.4: TM-AFM height images (z-range is 20 nm) of alignment of PFS domains in square corners of grooves with widths of 300 nm and 1.3 μm. The IF35/11EM11 films were exposed to an O_2-RIE plasma before imaging. The corresponding Voronoi representations are shown at the right hand side. See also Figure C.8.

The combination of wall-induced alignment and large-area correlation is expected to be optimal in hexagonal grooves that match the HP lattice of the copolymer. In series of hexagonal pits with different widths we observed single grains where the block copolymer matched its grain lattice to the angle of registration of 120°. In the smaller hexagonal pits, variations in row spacing and domain size were observed close to the edges. Figure 5.5 shows a SEM image of the largest hexagonal groove of approximately 1.3 μm. The domains are aligned with respect to the six side-walls over the entire groove, resulting in a 2-D ordering over a 1 μm^2 area. No apparent differences in domain sizes or row spacings near the edges are observed, indicating that deviations from incommensurability are distributed more easily over a large number of domains. The hexagonal grooves open up the possibility of accurate positioning of the domains, since one single domain is located in each corner, as shown in Figure 5.6.

The results on ordering in linear and hexagonal grooves suggest that the ordering mechanism is a combination of the aligning effect of the wall and the interaction between microdomains over a correlation length that extends

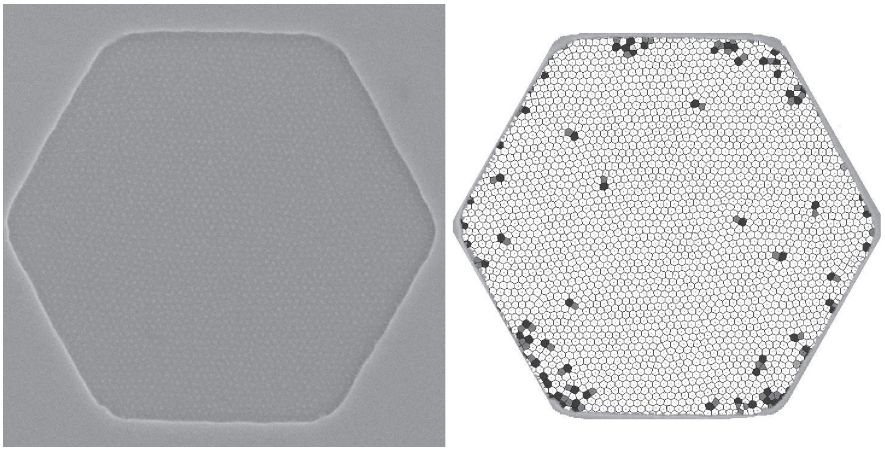

Figure 5.5: SEM image of PI-*b*-PFS block copolymer in a 1.3 μm wide hexagonal groove, and the corresponding Voronoi representation of the domains. The film was exposed to an O_2-RIE plasma before imaging. See also Figure C.9.

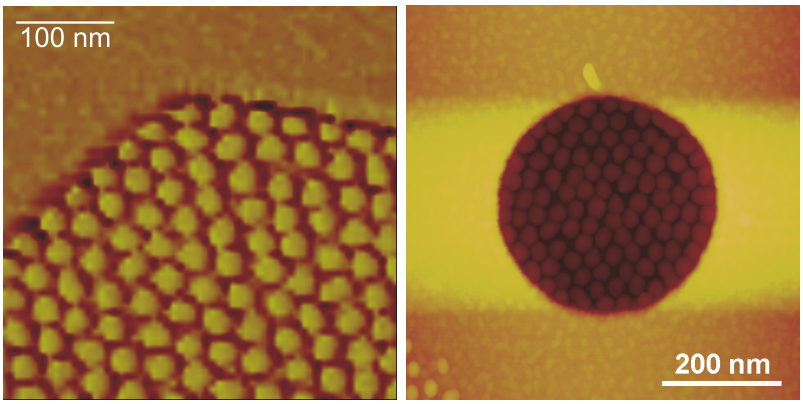

Figure 5.6: AFM-TM phase image (z- range is 30°) of domains in a 120° corner. One domain is located exactly in the middle of the corner, allowing for precise positional control of the domains over the entire hexagon (left). TM-AFM height image (z-range is 30 nm) of a PI-*b*-PFS block copolymer thin film in a circular pit (right). The IF47/13EM45 films were exposed to an O_2-RIE plasma before imaging.

over larger areas. An interesting case is therefore presented by the study of graphoepitaxial alignment in a series of circular pits with varying radii, and therefore varying curvature. Figure 5.6 (but also Figure 5.8) shows a typical example of PFS domains in a circular pit with a diameter of 300 nm. Although the row directly next to the edge follows the curvature, the other rows are not aligned with respect to the edge, but organize in one or few well-ordered grains,

independent of the side-wall. The block copolymer system adjusts to the side-wall curvature by a strong compression or expansion of the row spacing and strong variation in the domain size directly near the side-wall. The absence of alignment is in contrast to the directing effect of the side-walls in linear and hexagonal grooves. This displays the considerable ability to absorb stress by local adjustments, and demonstrate the high degree of elasticity in the phase-separated PI-*b*-PFS, that was also found in the response to incommensurate film thickness. The degree of curvature of the side-wall in circular pits does not play a role in the absence of alignment of the domains, as can be seen in Figure 5.8 for a number of pits with different diameter.

As discussed in section 4.3, PFS preferentially wets the thick silicon oxide layers, whereas on silicon there is no preference of PI or PFS blocks for the substrate. On flat substrates, long-range order was observed both on silicon and silica. On topographically patterned silica substrates, sidewall-induced ordering of PI-*b*-PFS is mostly absent, not extending to more than two to three rows directly near the edges. In addition, a coexistence of spherical and cylindrical morphology occurred often on silica substrates, as shown in the SEM images in Figure 5.7, which was not observed on silicon substrates.

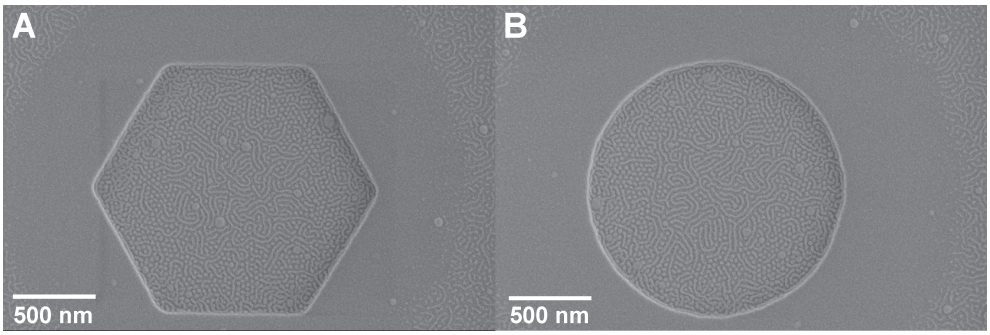

Figure 5.7: SEM images of IF44/15EM14 block copolymer in hexagonal and circular pits on silica substrates. The films were exposed to an O_2-RIE plasma before imaging. See also Figure C.10.

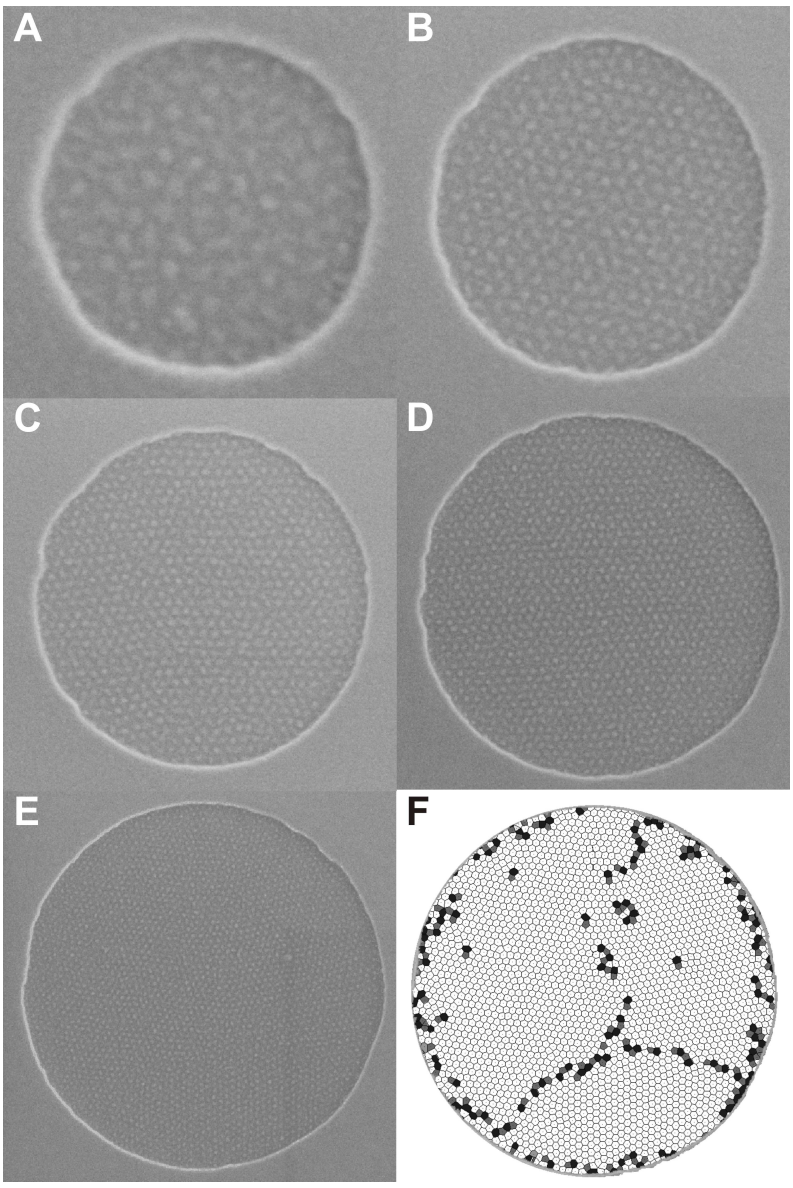

Figure 5.8: Series of IF44/15EM14 block copolymer in circular pits with diameters of A) 300 nm, B) 500 nm, C) 800 nm, D), 1 μm and E) 1.3 μm and its Voronoi representation (F). The films were exposed to an O_2-RIE plasma before imaging. See also Figure C.11.

5.3 Conclusions

Results of graphoepitaxial experiments with amorphous PI-*b*-PFS block copolymers in differently shaped grooves were presented. Successful alignment was achieved as long as the groove width did not extend beyond the natural grain size of the copolymer, which in case of PI-*b*-PFS is between 1 and 2 μm. 2D alignment was achieved in hexagonal grooves, where the HP coordination axes are registered with the side-walls. A complete mismatch between the HP ordered microdomain and the side-walls, as in case of circular pits, resulted in a complete absence of edge-induced order beyond more than one row of domains. The copolymer rather formed a single grain and absorbed the stress induced by the side-walls by variation in the domain sizes and row spacings near the edge. The results demonstrate that there appears to be no qualitative difference between asymmetrical or symmetrical wetting of the substrate in graphoepitaxy. This demonstrates that the nature of the substrate wetting is not a key issue in graphoepitaxial alignment of microdomains.

5.4 Experimental

Patterned substrates were prepared by electron beam lithography and optical lithography. Series of lines, circles and hexagons were patterned on the wafers. After resist removal, the wafers were cleaned in fuming nitric acid (100%) for 10 min and in boiling nitric acid (70%) for 10 min to destroy any residual organic material. Thin films were spin-coated from 1 wt% PI-*b*-PFS solution in toluene on flat or topographically patterned silicon substrates. Cleaning of the substrates and coating of the films was performed in a clean room. Film thicknesses (measured on flat areas of the substrates) ranged from 20 nm to 30 nm, established by ellipsometry, so as to yield a film with only one monolayer of microphase separated spherical domains in the grooves. The films were annealed at room temperature for approximately 20 h and subsequently exposed to an oxygen plasma, carried out in an Elektrotech PF 340 apparatus. The pressure inside the etching chamber was 10 mTorr, the substrate temperature was set at 10 °C, and an oxygen flow rate of 20 cm^3/min was maintained. Power was set at 75 W, and the thin films were exposed to the O_2-plasma for 10 s. The morphology of the thin films and the etched patterns was studied using a NanoScope III multimode atomic force microscopy (AFM) instrument (Digital Instruments/Veeco), operated in the tapping mode, and by scanning electron microscopy (SEM) (LEO 1550 FEG microscope).

Bibliography

[1] Ross, C. A., *Annu. Rev. Mater. Res.*, 2001, 31, 203-235.

[2] Naito, K., Hieda, H., Sakurai, M., Kamata, Y. and Asakawa, K., *IEEE Trans. Magn.*, 2002, 38, 1949-1951.

[3] Maier, S. A., Brongersma, M. L., Kik, P. G., Meltzer, S., Requicha, A. A. G. and Atwater, H. A., *Adv. Mater.*, 2001, 13, 1501-1505.

[4] Kim, S. O., Solak, H. H., Stoykovich, M. P., Ferrier, N. J., De Pablo, J. J. and Nealey, P. F., *Nature*, 2003, 424, 411-414.

[5] Edwards, E. W., Stoykovich, M. P., Möller, M., Solak, H. H., De Pablo, J. J. and Nealey, P. F., *J. Pol. Sci., Part B: Polym. Phys.*, 2005, 43, 3444-3459.

[6] Mansky, P., Liu, Y., Russell, T. P. and Hawker, C., *Science*, 1997, 275, 1458-1460.

[7] Kimura, M., Misner, M. J., Xu, T., Kim, S. H. and Russell, T. P., *Langmuir*, 2003, 19, 9910-9913.

[8] Kim, S. H., Misner, M. J., Xu, T., Kimura, M. and Russell, T. P., *Adv. Mater.*, 2004, 16, 226-231.

[9] Park, C., De Rosa, C. and Thomas, E. L., *Macromolecules*, 2001, 34, 2602-2606.

[10] Segalman, R. A., Cochran, E., Fredrickson, G. H. and Kramer, E. J., *Macromolecules*, 2005, 38, 6575-6585.

[11] Segalman, R. A., Yokoyama, H. and Kramer, E. J., *Adv. Mater.*, 2001, 13, 1152-1155.

[12] Cheng, J. Y., Ross, C. A., Smith, H. I. and Vancso, G. J., *Appl. Phys. Lett.*, 2002, 81, 3657-3659.

[13] Sundrani, D., Darling, S. and Sibener, S., *Nano Lett.*, 2004, 4, 273-276.

[14] Xiao, S., Yang, X., Edwards, E. W., La, Y. -H. and Nealey, P. F., *Nanotechnology*, 2005, 16, S324-329.

[15] Flanders, D. C., Shaver, D. C. and Smith, H. I., *Appl. Phys. Lett.*, 1978, 32, 597-580.

[16] Smith, H. I. and Flanders, D. C., *Appl. Phys. Lett.*, 1978, 32, 349-350.

[17] Smith, H. I., Geis, M., Thompson, C. and Atwater, H., *J. Chrystal Growth*, 1983, 63, 6831-6839.

[18] Yokoyama, H., Mates, T. E. and Kramer, E. J., *Macromolecules*, 2000, 33, 1888-1898.

[19] Segalman, R. A., Hexemer, A., Hayward, R. C. and Kramer, E. J., *Macromolecules*, 2003, 36, 3272-3288.

[20] Segalman, R. A., Hexemer, A. and Kramer, E. J., *Macromolecules*, 2003, 36, 6831-6839.

[21] Cheng, J. Y., Ross, C. A., Thomas, E. L. and Smith, H. I. and Vancso, G. J., *Adv. Mater.*, 2003, 15, 1599-1602.

[22] Cheng, J. Y., Mayes, A. and Ross, C. A., *Nat. Mater.*, 2004, 3, 823-828.

[23] Cheng, J. Y., Zhang, F., Smith, H. I., Vancso, G. J. and Ross, C. A., *Adv. Mater.*, 2006, 18, 597-601.

[24] Lammertink, R. G. H., Hempenius, M. A., Vancso, G. J., Shin, K., Rafailovich, M. H. and Sokolov, J., *Macromolecules*, 2001, 34, 942-950.

[25] Segalman, R. A., Schaefer, K. E., Fredrickson, G. H. and Kramer, E. J., *Macromolecules*, 2003, 36, 4498-4506.

CHAPTER 6

Poly(ferrocenylsilane-*b*-lactide) block copolymers

A block copolymer of PFS with a polar poly(*D,L*-lactide) (PLA), biodegradable block was synthesized and studied, to probe the effect of strong substrate interactions on pattern formation in thin films. Successful synthesis of PFS-*b*-PLA was demonstrated, which constitutes to our knowledge the first example of a block copolymer with an organometallic block and a biodegradable organic block. Thin films of these polymers phase separate to form PFS microdomains in a PLA matrix. Additionally, for ultra thin films (< 5 nm) substrate induced patterns (SINPATs) formed. The SINPATs consisted of strongly surface-adsorbed PLA blocks on top of which the PFS blocks dewetted into sphere-like features, with diameters of around 20 nm. The lateral spacing between these features is regular, and is typically larger than the length-scale associated with block copolymer phase separation. Two distinct types of patterns are thus accessible with these block copolymers through substrate interactions and film thickness. These patterns might serve as templates in the fabrication of functional nanoplatforms.

*Parts of this chapter are included in: *Nanopatterning with polyferrocenylsilane-block-polylactide block copolymers.* Roerdink, M., van Zanten, T. S., Hempenius, M. A. and Vancso, G. J., *o be submitted.*

6.1 Introduction

Polymer-substrate interactions have been shown to strongly affect the morphology in thin block copolymer films. Specific interactions between one block and the substrate or surface dictate preferential wetting or dewetting and thus the thickness commensurability and morphology. The block copolymers studied in the previous chapters, PI-*b*-PFS and PS-*b*-PFS, demonstrated different substrate wetting, but consisted nonetheless of two apolar blocks with a small difference in interfacial energy. Many examples exist of studies on thin films of block copolymers with a polar and apolar block.[1–4] The difference in polarity suggests a larger enthalpic contribution to the phase segregation in comparison with the systems studied by us so far. We were interested in studying the effect of an increased segregation strength on thin film morphology, in particular the effect on ordering of the microdomains. Further, regarding the discussion of the importance of substrate wetting in graphoepitaxy, it is of interest to know if a strong preferential interaction of one of the blocks affects the ability of guided assembly of the domains on the substrate.

Large-area lateral ordering in a block copolymer with a strongly polar block and an apolar block, PS-*b*-poly(2-vinylpyridine) (P2VP), was demonstrated by Segalman *et al.*[1] on topologically patterned substrates. Ordering on the mesas and in the grooves extended over widths of 4.5 μm in thin films of about one monolayer thickness. The copolymer formed a brush layer on the substrate, with P2VP located directly at the substrate. Spatz *et al.*[2–4] reported on so-called ultrathin monomolecular PS-*b*-P2VP films. In these films, a brush could not be formed due to the extremely low surface concentration of polymer that was too low to ensure a homogeneous film without severe deviation from the equilibrium shape. The P2VP blocks adsorbed on the substrate (mica was used, but similar observations were made on hydrophilic GaAs and silicon wafers), and stretched to about five times their radius of gyration in the unperturbed state. The PS block dewetted the P2VP block, forming clusters with diameters and lateral spacings tunable by the block lengths (see Figure 6.1). The lateral phase separation thus obtained is much larger than the typical microdomain phase separation and constitutes another approach to periodic arrays of domains on the nanoscale. The structures were used for nanolithography by preferential deposition on the PS clusters, which enabled the selective removal of the P2VP and transfer of the pattern into the underlying substrates.[4]

Successful sequential anionic polymerization to form block copolymers requires equal or greater basicity of the carbanion of the first block compared to the resulting propagating chain end.[1] Tuning of the basicity of the living end

[1] pK_a of the initiating carbanion $\geq$ resulting carbanion

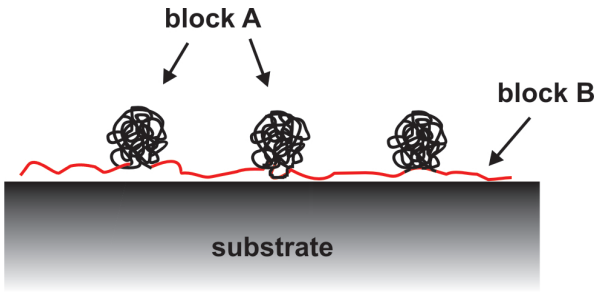

Figure 6.1: Clusters formed by block A dewet onto block B that is strongly absorbed to the substrate.

can be done by end-capping with an appropriate endgroup, thus forming a macroinitiator that can initiate the next block. PFS containing block copolymers with relatively polar blocks, such as poly(methacrylates) have been obtained using hydroxyl-functional initiators or end-cappers for the PFS blocks. These could be used directly for the growth of a poly(*N,N*-dimethylaminoethyl methacrylate) block[5] or be derivatized to an atom transfer radical polymerization (ATRP) initiator for growing a poly(methyl methacrylate) block.[6] Other end-capping strategies have also led to PFS-*b*-PMMA block copolymers using an all-anionic polymerization approach.[7,8] The self-assembly of PS-*b*-PMMA in thin films was described and demonstrated a typical, but not well-ordered block copolymer morphology. In a block-selective solvent, cylindrical micelles were formed.[9]

The choice of the second block was intended to be such that next to a difference in polarity, an additional functionality could be introduced. PLA is obtained by polycondensation of hydrocarboxylic acids, or by ring-opening polymerization (ROP, see Figure 6.2) of cyclic esters.[10] These polymers are biodegradable through enzymatic degradation or through hydrolysis, where the rate of hydrolysis depends on the microstructure,[11] pH,[12] or temperature.[11,12] During degradation, the pharmacological inactive substance lactic acid is formed, which is absorbable by the body or removable by metabolism.[13]

Thin films of diblock copolymers of PLA have been reported with polyisoprene,[14] poly(ethylene-*alt*-propylene),[15] polystyrene,[16] and poly(4-fluorostyrene)[17] to create nanoporous material[18] or nanolithographic templates for magnetic nanodots through the hydrolytic degradation of the PLA phase.[19]

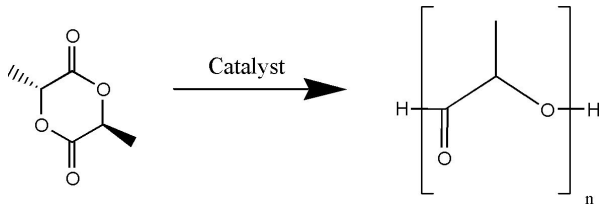

Figure 6.2: Polylactic acid from the cyclic lactide mononer.

Block copolymers of PFS and an aliphatic polyester poly(lactic acid) (PLA) have not been reported, but offer, through the biodegradability in combination with the organometallic block, novel options for the fabrication of nanosized patterns. This chapter describes the synthesis of a PFS-*b*-PLA diblock copolymer, using a two-step living polymerization process, and a study of its thin film behavior.

6.2 PFS-*b*-PLA synthesis

PFDMS-*b*-PLA block copolymers were synthesized, where the organometallic block was prepared by anionic polymerization and hydroxypropyl end-functionalized, to serve as a macroinitiator in the catalyzed ring-opening polymerization (ROP) of *D,L*-lactide monomers. The macroinitiator was end-capped by adding 3-(*tert*-butyldimethylsiloxy)propyldimethylchlorosilane to the living PFS ends, as described by Korczagin *et al.*[6] The ROP to form the polylactide block proceeded in the presence of a Sn(II) or Zn(II) catalyst. This type of polymerization has a pseudo-anionic character and is often referred to as a coordination-insertion ROP.[20,21] The mechanism of the growth of the PLA block is schematically depicted in Figure 6.3.

The thus obtained block copolymers were characterized by ^{1}H NMR spectroscopy and GPC. The ^{1}H NMR spectra of the macroinitiator with the protecting *tert*-butyl trimethylsilyl ether end-group **1**, macroinitiator with the hydroxypropyl group **2**, and the PFS-*b*-PLA diblock copolymer **3** are shown in Figure 6.4. The degree of polymerization can be obtained from the ratio of the integral of the singlet at 0.208 ppm, associated with the dimethylsilyl moiety at the *n*-butyl initiated side (a), and the singlet at 0.46 ppm that originates from the dimethylsilyl units in the polymer backbone (b). Deprotection of **1** with diisobutylaluminium hydride to **2** is accompanied by a shift of the signal associated with the dimethylsilyl moieties at the functionalized end of the copolymer from 0.218 ppm to 0.238 ppm (d). The singlet resulting from the *tert*-butyl groups at a chemical shift of 0.900 disappears accordingly

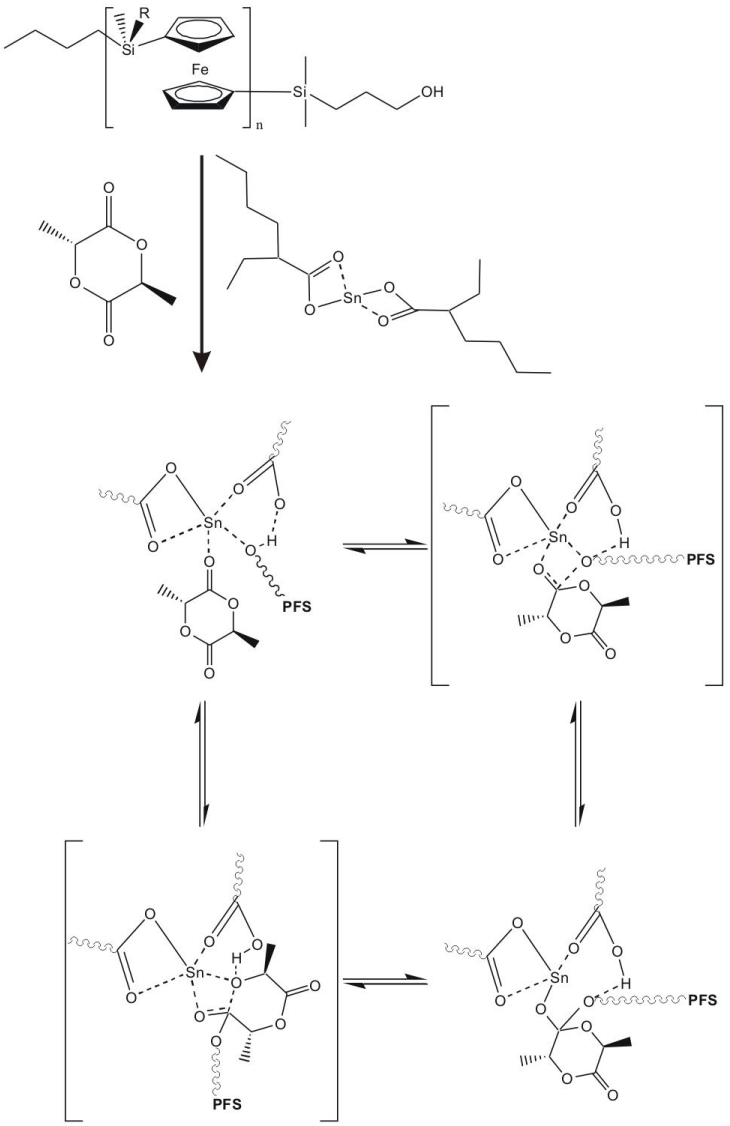

Figure 6.3: Mechanism of ring-opening polymerization of *D,L*-lactide with stanneous actoate. Adapted from ref.[21]

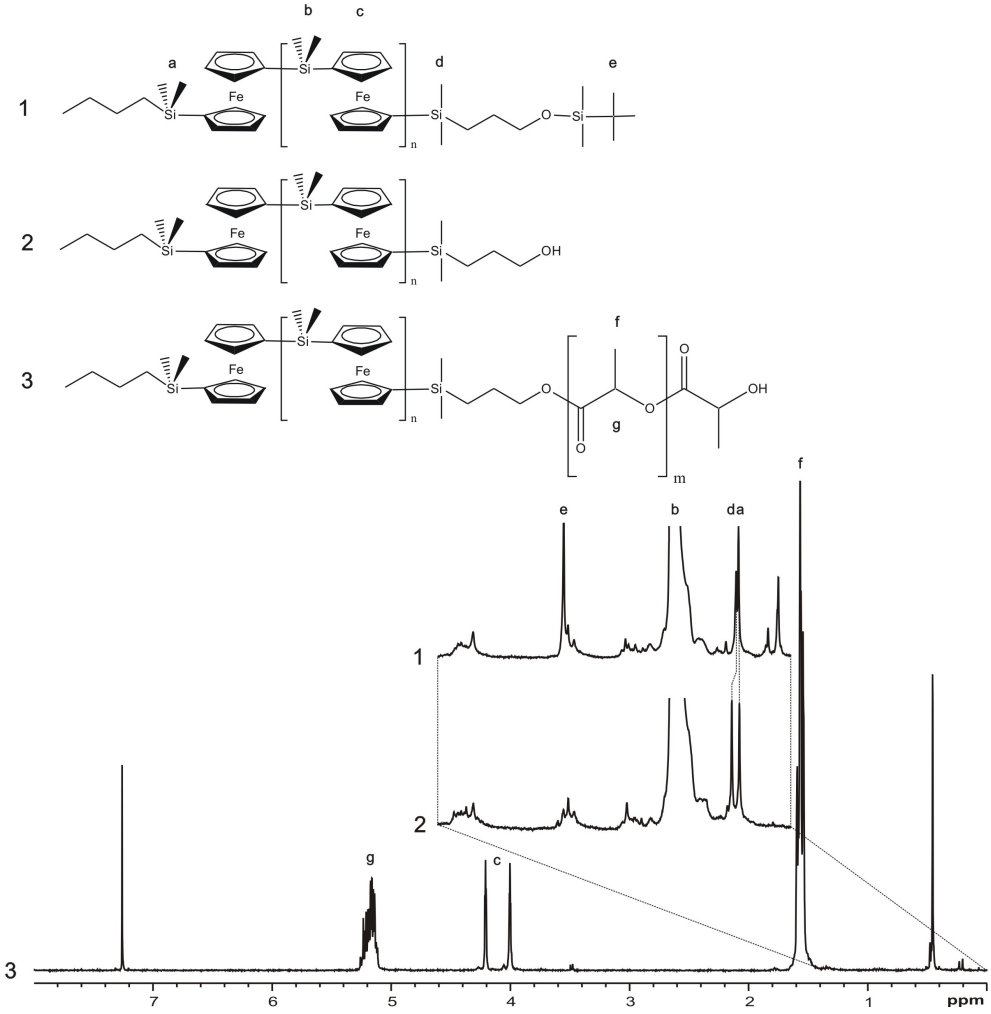

Figure 6.4: 400 MHz ^{1}H NMR spectra of the protected macroinitiator (**1**), the macroinitiator (**2**), and the PFS-*b*-PLAdiblock copolymer (**3**). The zoomed in sections show the dimethylsilyl signals at the *n*-butyl side at $\delta = 0.238$ (a) and at the hydroxypropyl-functionalized side at $\delta = 0.208$ (d).

(e). The degree of end-functionalization was determined from the ratio of dimethylsilyl signals of the end-functionalized side and *n*-butyl side. The efficiency for end-functionalization was typically around 65%. An efficiency of less than 100% was likely caused by the presence of impurities in the endcapper reactant. These impurities can be removed by treating the endcapper reactant with 10-20 mol% of *sec*-butyllithium.[22] This resulted in an efficiency for end-functionalization of more than 95%. The remaining 5% of unfunction-

alized PFS could easily be removed by column chromatography, leading to 100% hydroxypropyl end-functionalized PFS.

The PFS-*b*-PLA **3** shows characteristic multiplets from PLA at chemical shifts of 1.59 ppm (f) and 5.16 ppm (g). Conversion after ROP was determined before precipitation in methanol by comparing the signals of the PLA block with the relative amount of unreacted monomer that shows peaks at chemical shifts of 1.68 ppm and 5.02 ppm.

A two dimensional COSY spectrum of the PFS macroinitiator is shown in Figure 6.5. The three scalar couplings ($J_{a,b}$, $J_{b,c}$, and $J_{c,d}$) that originate from the *n*-butyl group and the three scalar couplings ($J_{j,k}$, $J_{k,l}$, and $J_{l,m}$) from the end-functionalized side are indicated in the spectrum. With the aid of this COSY spectrum, the ^{1}H NMR spectrum of the macroinitiator could be fully assigned.

Table 6.1: Molecular characteristics of the synthesized diblock copolymers.

Name	M_n [a]	M_n [b]	M_w [b]	M_w/M_n [b]	PFS [a]	M_w/M_n	M_w/M_n
	[kg/mol]	[kg/mol]	[kg/mol]		[vol%]	PFS [b]	PLA [d]
FL7/17 [e]	23	13	26	2.00	28	1.32	2.51
		16 [c]	29 [c]	1.84 [c]			
FL8/34 [f]	41	39	56	1.41	19	1.32	1.62
FL7/27 [f]	34	25	45	1.78	21		

[a]Measured by ^{1}H NMR. [b]Measured by GPC in THF, relative to polystyrene standards. [c]Measured by GPC in chloroform, relative to polystyrene standards. [d]Calculated using Equation 6.1. [e]Prepared with the Sn-catalyst. [f]Prepared with the Zn-catalyst.

The characteristics of the PFS-*b*-PLA diblock copolymers obtained by NMR and GPC are summarized in Table 6.1. The nomenclature of the different polymers in Table 6.1 will be used throughout the chapter and is based on the ^{1}H NMR measurements. FL 7/17, for example, is a PFS-*b*-PLA copolymer consisting of a PFS (F) block with a molar mass of 7 kg/mol and a PLA (L) block with a molar mass of 17 kg/mol.

The apparent molar masses obtained by NMR and GPC differ. The GPC results depend on the compatibility of the individual blocks with the solvent which is used. A higher molar mass is obtained in chloroform compared to THF, due to the better solubility of the majority block PLA in chloroform, presumably resulting in an increased expansion of the PLA block. Since the two blocks are synthesized in independent polymerization steps, the polydisper-

sity of each block contributes to the polydispersity of the PFS-*b*-PLA diblock copolymer according to

$$\mathrm{PDI}_{\text{PFS-}b\text{-PLA}} = (\mathrm{PDI}_{\mathrm{PFS}} - 1){w_{\mathrm{PFS}}}^2 + (\mathrm{PDI}_{\mathrm{PLA}} - 1){w_{\mathrm{PLA}}}^2 + 1 \qquad (6.1)$$

where $\mathrm{PDI}_{\text{PFS-}b\text{-PLA}}$ is the polydispersity of the overall diblock copolymer and PDI_i and w_i are the polydispersity and weight fraction of each respective block.[23] The conversion of PLA monomer units during the ROP and the polydispersity of the PFS-*b*-PLA diblock copolymer was found to be lower when using the Zn(II) catalyst, compared to the Sn(II) catalyst. However, the Zn(II) catalyst is, on the small scale of the polymerization employed (10^{-4} mol living chain ends), extremely sensitive to impurities. Clean glassware, a fresh catalyst solution and a freshly recrystallized PLA monomer batch resulted in successful ROP with the Zn(II) catalyst.

The PFS-*b*-PLA block copolymers show a glass transition at 20 °C for the PFS block and at 36 - 44 °C for the PLA block, and are therefore glassy at room temperature. The PFDMS block constitutes a semi-crystalline block, and crystallization can be expected at temperatures above the glass transition of both blocks. To assess the degree of crystallization, isothermal crystallization was allowed for up to 2 hours at various temperatures using differential scanning calorimetry (DSC). However, only isothermal crystallization at 70 °C yielded a small endothermic peak associated with melting of crystals around 120 °C. Isothermal crystallization at other temperatures (90 °C - 100 °C) did not result in observable melting transitions. The distinct difference in blocks apparently traps configurational rearrangements of the chains at the block-block interface, which restricts the mobility in the PFS microdomain as well.

6.3 Bulk morphology

Monitoring the storage and loss moduli (G' and G'') as a function of temperature provides information on thermal transitions in the block copolymer, such as the order-disorder transition. The order-disorder transition (ODT) temperature is an indication for the strength of the phase segregation. Strong phase separation between PFS and PLA is expected, due to the chemical contrast between the polar PLA and the apolar PFS. Another indication of strong phase separation is that PS-*b*-PLA was found to be in the strong segregation regime. Since PFS and PS have similar solubility parameters, PFS-*b*-PLA can also expected to be in the strong segregation regime.[18,24]

Figure 6.6 shows a plot of the storage and loss moduli versus temperature

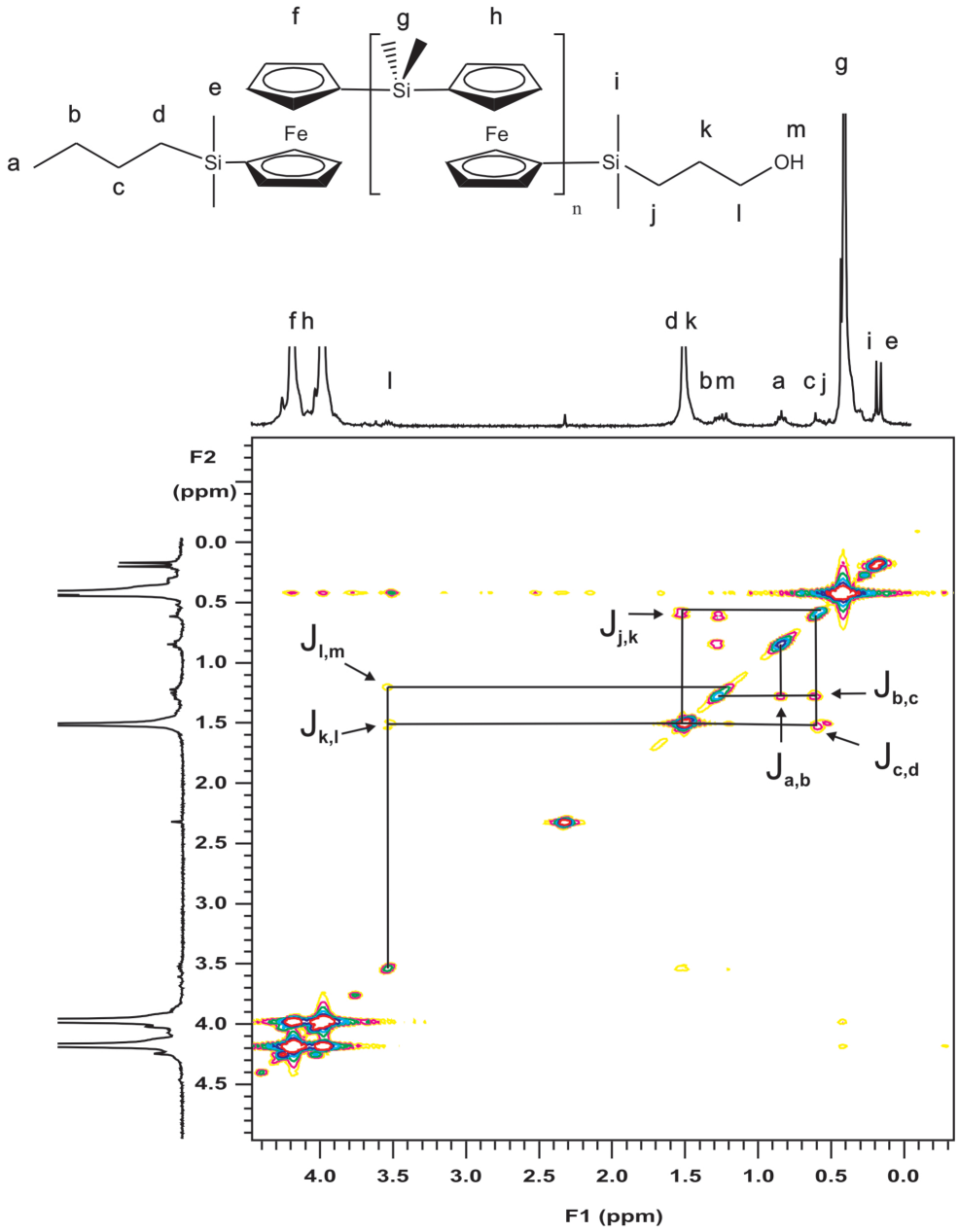

Figure 6.5: COSY spectrum of the hydroxypropyl-terminated macroinitiator. The characters are associated with the different protons of the macroinitiator and their respective ^{1}H NMR peaks in the upper frequency plot. The cross signals that deviate from the diagonal represent the couplings originating from the initiator side (here indicated below the diagnonal) and from the end-functionalized side (indicated above the diagonal).

for a bulk sample of FL7/17 which was heated from 100 °C to 250 °C at 0.25 °C/min.

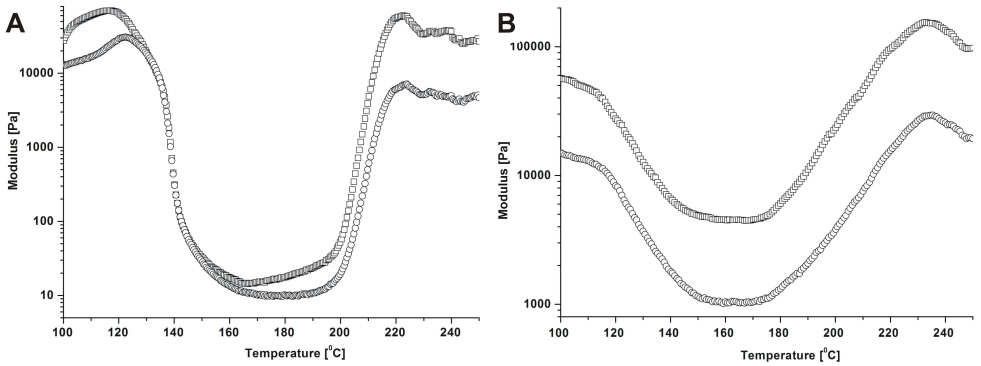

Figure 6.6: The change in loss (□) and storage (○) modulus of FL7/17 upon increasing the temperature, as observed by means of dynamical mechanical measurements. (A) The first run and (B) the second run after cooling.

The first drop in both the loss and storage modulus at 136 °C (inflection point) is most probably due to an order-disorder transition. Based on DSC measurements, possible melting of the PFS microdomains is discarded. At 215 °C both moduli increase again. This is unexpected but might be due to transesterfication reactions at these temperatures, resulting in high modulus network-like structures. The much higher initial moduli in the second heating run (Figure 6.6B) can be taken as a good indication for a chemical transformation, such as transesterfication.

Thermogravimetrical analysis on PFS-*b*-PLA block copolymers indicated mass loss of the PLA block at temperatures of 230 °C and higher.[2] Hillmyer and coworkers[27] have reported similar observations on the chemical stability of PLA in block copolymers when annealing at temperatures above 150 °C.

To complement the dynamic mechanical measurements, SAXS measurements were performed to determine the bulk morphology and find temperature-dependent morphology transitions. Unannealed samples did not show higher order peaks, reflecting the necessity of an annealing step. Annealing at 90 °C resulted in the azimuthally averaged intensity plot and the corresponding Fourier transform shown in Figure 6.7.

The first well-defined intensity maximum denotes the presence of periodicity, corresponding to a *d*-spacing of 26.4 nm. The two broad shoulders in the intensity indicate higher order, although ill-defined. This specific sample

[2]Thermogravimetry analysis (TGA) showed 5% and 10% weight loss of PLA (M_w of 35 k) at 230 °C and 290 °C, respectively. For PFS-*b*-PLA, 5% and 10% weight loss was observed at 275 and 290 °C, respectively.

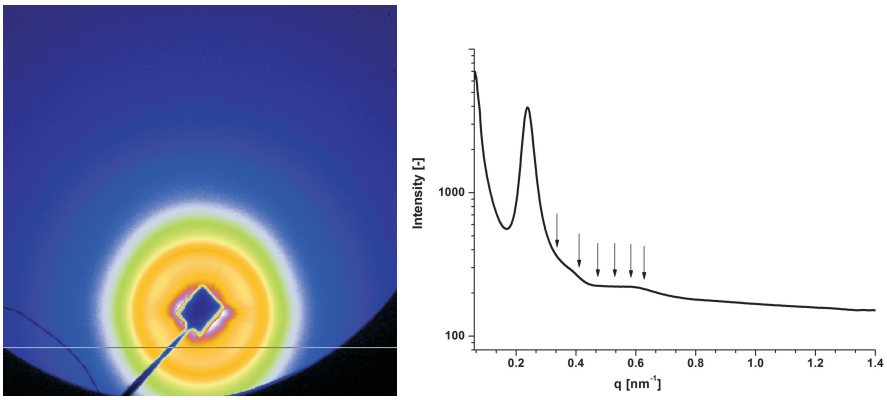

Figure 6.7: Small angle X-ray scattering (SAXS) profiles of FL8/34 annealed for five h at 90 °C with a d-spacing of 26.4 nm. The figures show some higher order reflections, although ill-defined. The arrows in the right profile indicate the $\sqrt{2} - \sqrt{7}$ relative peak positions for a BCC morphology.

was, after annealing 10 min at 150 °C to melt crystalline areas, annealed for 5 hours at 90 °C, to obtain thermodynamic equilibrium. Apparently, the degree of order in this block copolymer is very short-ranged in the bulk, even upon annealing.

Specimens annealed for 2 days at 150 °C (above or around the ODT, as determined from rheology) showed a broadening of the first intensity maximum, as well as a shift of the position of this maximum to higher d-values. GPC measurements indicated an increase in the number average molar mass and in the polydispersity (see Table 6.2). Since PFS is known to be stable up to high temperatures, the increase in polydispersity is assigned solely to the PLA block. According to Equation 6.1, the polydispersity of the PLA block can be calculated to increase from 1.6 to 3.7. This increase in the molar mass distributions arises from chemical changes in the backbone upon annealing at this temperature. Most probably chain scission takes place, resulting in the lower number average molar mass M_n. The relatively small decrease in the weight average molar mass M_w compared to M_n, and the strong increase in the polydispersity of the PLA blocks are due to transesterfication reactions of the cleaved PLA chains. Furthermore, the onset of macrophase separation is observed in SAXS.

To determine the ODT temperature, SAXS profiles were taken during heating runs. Arrangement of these profiles at the different temperatures resulted in the 3D plot shown in Figure 6.8. Before the SAXS measurement, the FL8/34 bulk sample was annealed for 48 h at 150 °C, but specimens

Table 6.2: Molar mass and polydispersity of the FL8/34 diblock copolymer after vacuum annealing for 48h at 150°C.

Time at 150 °C	M_n	M_w	M_w/M_n
h	[kg/mol]	[kg/mol]	
0	39	56	1.41
48	18	51	2.80

annealed at lower temperatures or unannealed showed similar results. The low temperature shoulders became more vague around 160 °C, which suggests the occurrence of an ODT. However, two broad maxima reappear at higher temperature, though shifted to lower q and thus higher d-spacing. As argued before, this can be caused by the onset of macrophase separation, caused by chain scission and transesterfication of the PLA blocks. The chain scission seems to be a gradual process at these temperatures, as the associated domains slowly increased in size. The scattering signal completely disappeared at temperatures above 250 °C, due to complete degradation of the PLA matrix. To illustrate the difference at the starting and end temperature, the first and the last scattering profiles of Figure 6.8 are shown separately in Figure 6.9, demonstrating the change in morphology of the block copolymer upon heating.

An ODT typically leads to the disappearance of higher order peaks and a sharp drop in the intensity of the first peak. However, due to the chain scission processes that occur, an order-disorder transition cannot be identified anymore as such since the sample consists of ill-defined block copolymer and homopolymer. The SAXS scattering profiles at higher temperatures are the result of phase separation of the remaining chemically modified block copolymer (possibly with very different solubility parameters than the initial block copolymer) and possibly macrophase separation of formed homopolymer.

The ODT temperatures observed for the polymers are slightly lower, but comparable to values reported for ODT temperatures in PS-*b*-PLA, which were around 165 °C for polymers with cylindrical morphology and similar molar mass.[18]

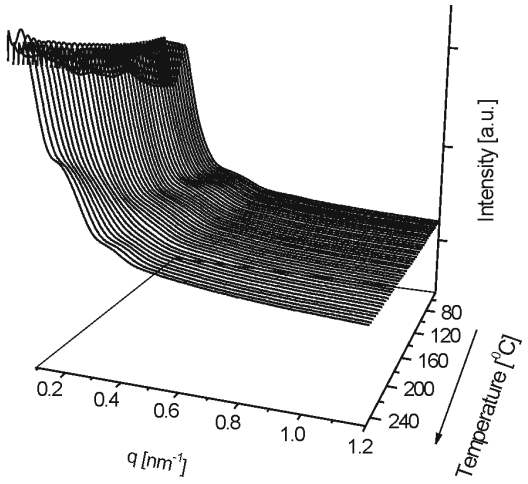

Figure 6.8: Dynamic SAXS scattering patterns at temperatures from 45 °C to 250 °C. The heating rate is 10 °C/min.

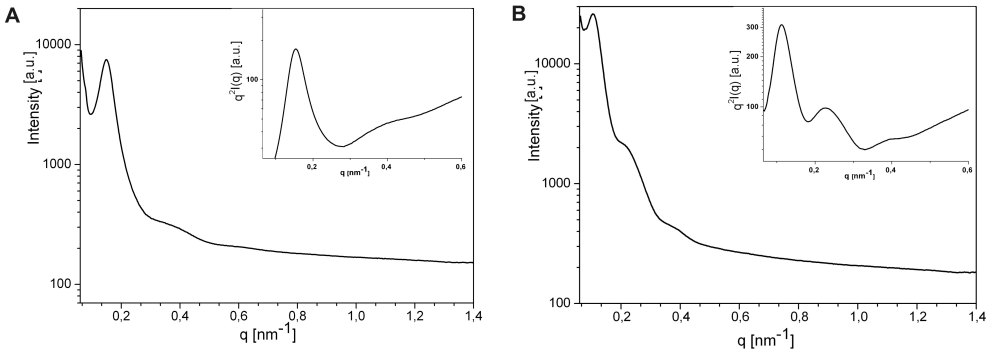

Figure 6.9: Two SAXS patterns taken during a heating scan of FL8/34, showing the scattering profile at 45 °C (A) and at 250 °C (B). The insets show Kratky-plots ($q^2 I(q)$ versus $I(q)$) at low values of q.

6.4 Thin film morphology

A thin film morphology study can help to elucidate the bulk morphology. The SAXS data indicated, in conjunction with the volume fraction determined from ^{1}H NMR, a BCC morphology for FL8/34. Nevertheless, due to the absence of well-defined higher order peaks such a conclusion remains suggestive. The morphology in thin films of PFS-*b*-PLA clearly indicated microscopic phase separation (Figure 6.10B and C), confirming the restricted phase separation and thus confirming the successful block copolymerization, as opposed to the macroscopic phase separation in a blend of homopolymers (hPFS, and hPLA) with similar molar mass (Figure 6.10A).

Films of FL7/17 ($\phi_{PFS} = 0.28$) and FL8/34 ($\phi_{PFS} = 0.19$) show a mixed cylindrical and spherical thin film morphology and a spherical morphology, respectively. The high polydispersity (PDI = 1.998) of FL7/17 is most probably the reason for the occurrence of both cylinders and spheres, by promoting locally the crossing of the order-order transition. The spherical morphology observed for FL8/34 agrees with the morphology established by SAXS. However, due to strong substrate interactions, thin film morphologies can differ from the bulk. This needs to be considered when comparing the thin film and the bulk morphology.

Thin films were prepared on mica, silicon with native oxide, and on a silanized silicon surface. The thin PFS-*b*-PLA films on silanized (with octadecyltrichlorosilane) silicon did not remain the surface during spincoating, indicating unfavorable surface interactions between the alkyl chain on the substrate surface and the PFS or PLA chains. The small amount of diblock copolymer that remained on the surface agglomerated in droplike domains. The contact angle on these silanized surfaces was ~80° (implying only partial covering of the substrate with self-assembled monolayer). The polar PLA block is expected to preferentially wet the native oxide layer of silicon, silica, and possibly adsorb strongly to the more ionic surface of mica. Based on the surface tension of PFS (γ = 33 mN/m[25]) compared to the surface tension of PLA (γ = 36.6 - 41.1 mN/m[26]), PFS is expected to wet the free surface of the thin films. However, SIMS indicated the presence of repeating units of the PLA polymer backbone at the surface (Figure 6.11). Apparently, the segregation of the minority PFS block at the surface, which would involve chain stretching and a severe distortion from the spherical equilibrium shape, results in a higher free energy penalty than the energy gain on surface wetting by the lower interfacial tension block. Thus, both phases are expected at the surface.

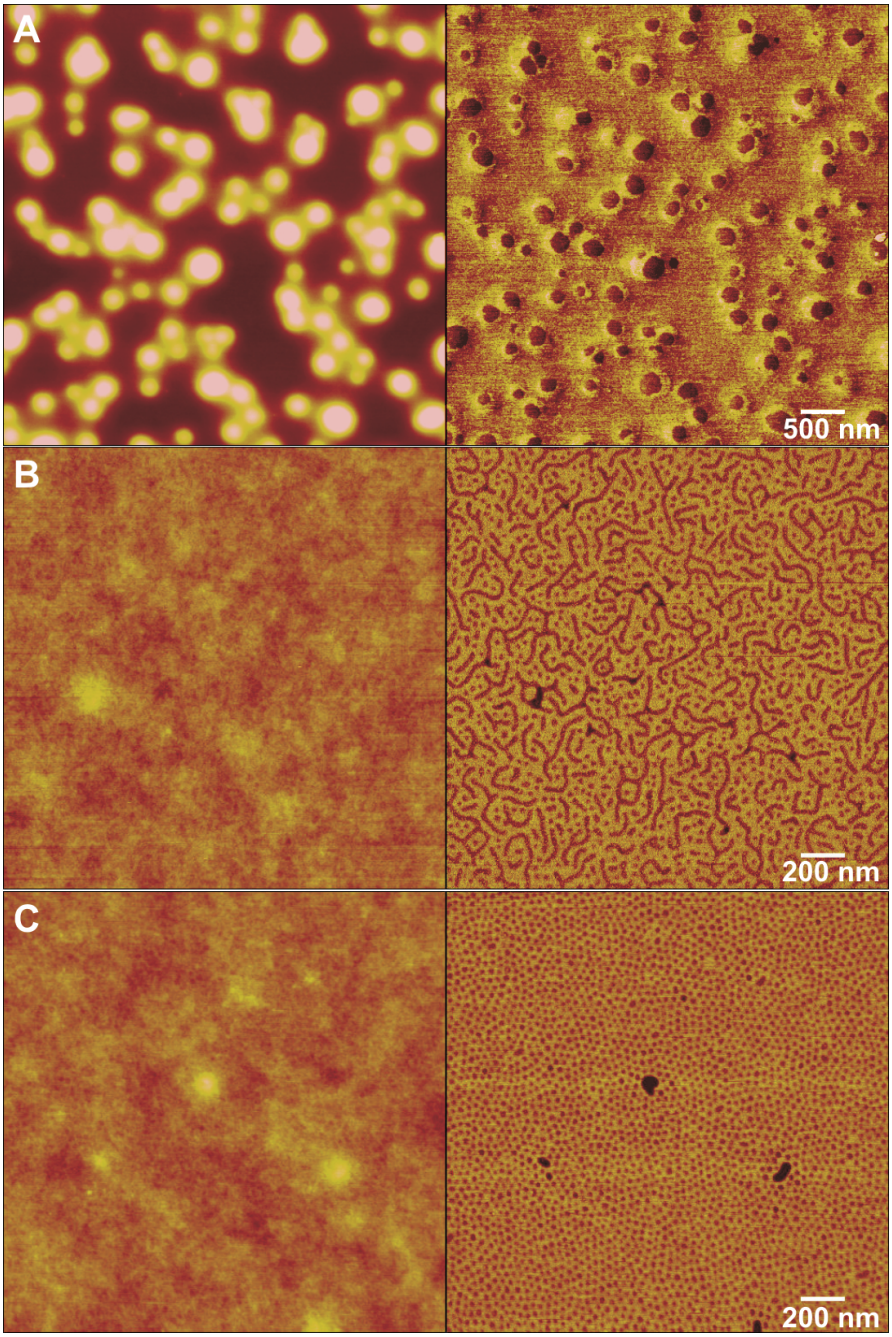

Figure 6.10: Height and phase AFM images of thin films made from a blend of F20 with L35 ($\phi_{PFS} = 0.20$), annealed for 12h at 150 °C (A), of a thin film made from FL7/17 ($\phi_{\mathrm{PFS}} = 0.28$) (B) and FL8/34 ($\phi_{\mathrm{PFS}} = 0.19$) (C). The block copolymer films were annealed at 150 °C for 36h. The *z*-range for the phase images is 40°. For the height images: 40 nm for (A) and 10 nm for (B) and (C).

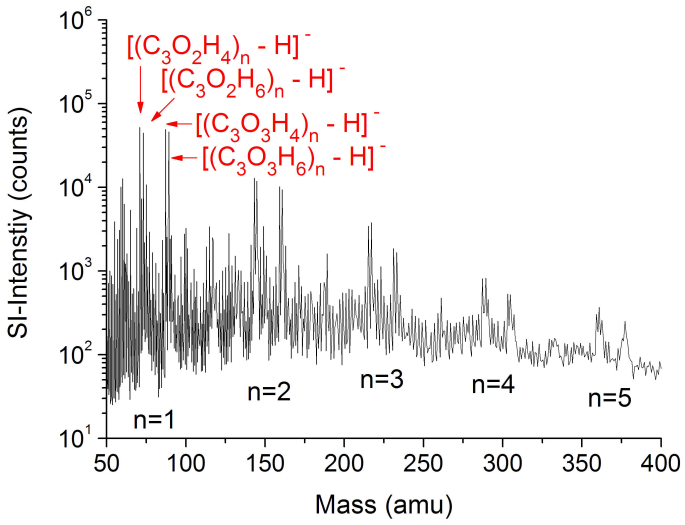

Figure 6.11: SIMS spectrum of a 182 nm thick film showing the negative secondary ions from PLA. Not only C_3 units of the backbone are ionized but also dimers (C_6, n=2), trimers (C_9, n=3) *etc.* units.

Block copolymer films that are incommensurate with a specific film thickness will form relief structures that locally have a commensurable height. A dewetted ultra thin film of FL8/34 on mica (film thickness ∼10 nm) showed such relief structures (Figure 6.12). Cross-sectional analysis of the height image indicated step heights of ∼15 nm, 33 nm and 43 nm, suggesting stable films for these film thicknesses.

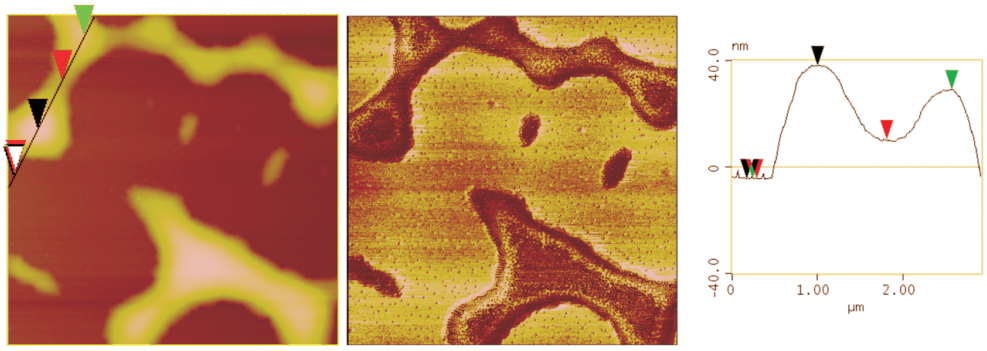

Figure 6.12: AFM-TM height (*z*-range is 80 nm) and phase (*z*-range is 10°) images of a dewetted FL8/34 thin film on mica, showing step heights of 14.7 nm (red), 33.3 nm (green), and 42.3 nm (black). The image width is 5 μm. See also Figure C.12.

Films with a thickness of 15 nm or 42-45 nm were stable upon annealing, as expected. However, 30 nm thick films became unstable upon annealing at 150 °C for 48 h, that is the obtained films were not flat. The commensurable film thicknesses agree with a wetting of substrate and surface as depicted in Figure 6.13 and can be described by $h = (n + 0.5)\, L_0$, where L_0 is the d-space obtained from SAXS, and n is an integer.

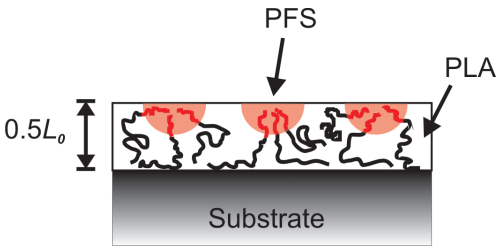

Figure 6.13: Schematic of the proposed wetting of the PLA block of a hydrophilic substrate (silicon oxide, mica) and wetting of PFS and PLA at the free surface. The natural film height is $(n + 0.5)L_0$.

Similar to the SAXS observations, temperature and annealing time proved to be of importance for the size of the domains in 45 nm films. The domain size changed considerably with annealing time at 150 °C and was approximately doubled after 48 hours (Figure 6.14). In contrast, no increase in domain size was observed in 15 nm thick FL8/34 films (Figure 6.15). After 30 min annealing at 150 °C, the morphology of the film did not change further.

We assume that upon annealing at 150 °C chemical modification, such as transesterfication of the PLA occurs. This results in an increase in polydispersity and an increase in mobility. Similar observations on chain scission in PLA block copolymers on annealing have been made by others.[16,27] The authors observed an increase in domain size of the minority PLA phase and attributed this to swelling of the domains with *in-situ* formed homopolymer of the minority phase. The homopolymer was formed through chain scission at the block junction. A similar phenomenon probably causes the increase in domain sizes observed for the PFS-*b*-PLA studied. First, longer annealing at elevated temperatures leads to more chain scission. Second, the formed PFS homopolymer can easily diffuse and enrich the microdomains. However, in the 15 nm films, the mobility is restricted due to the strong interaction of PLA with the substrate, which probably impedes chain scission and certainly the diffusion of formed homopolymer.

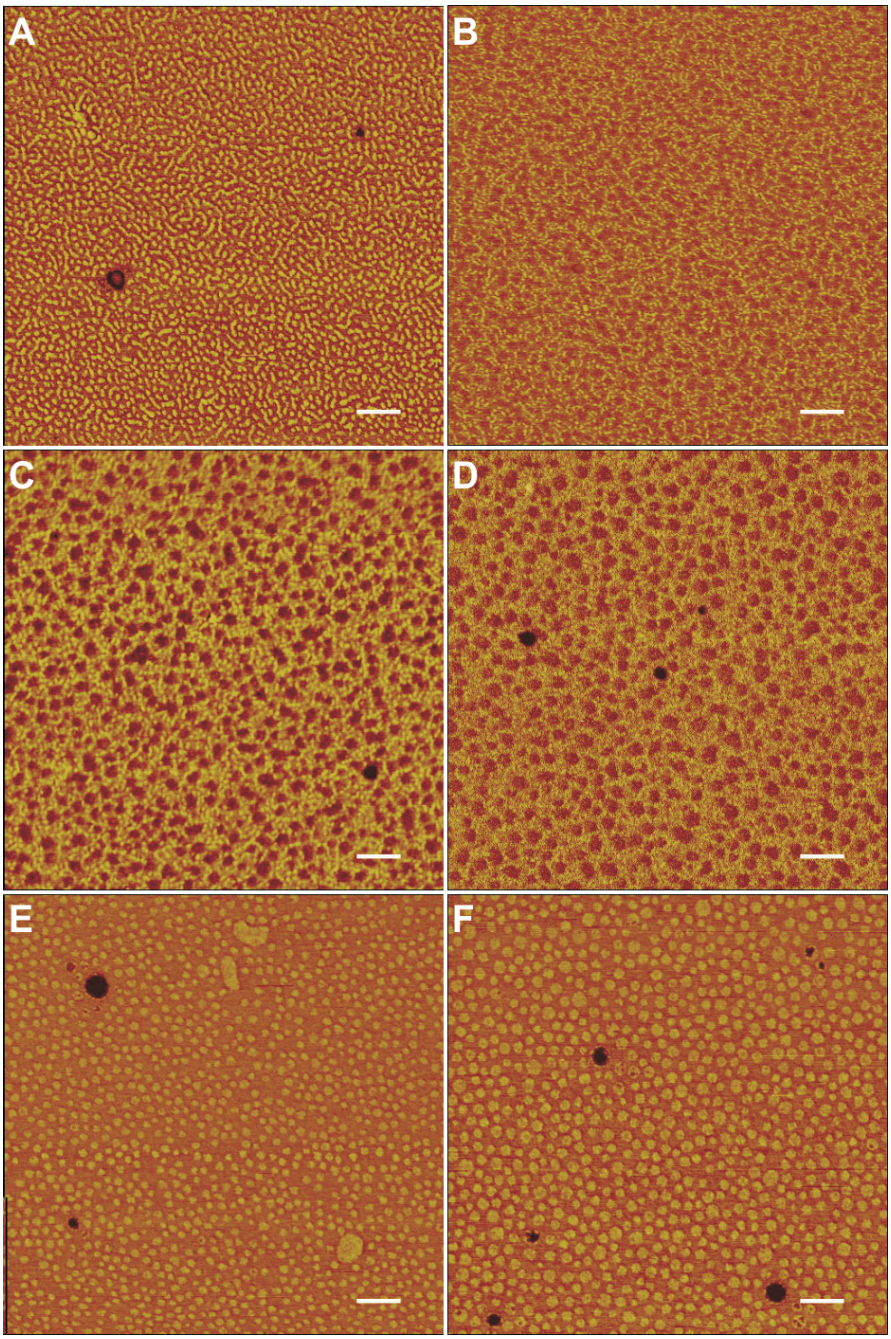

Figure 6.14: AFM-TM phase images (*z*-range is 20°), illustrating the effect of annealing time at 150 °C on 45 nm FL8/34 films as cast (A), after 30 min (B), after 4 h (C), after 8 h (D), after 24 h (E), and after 48 h (F). All scale bars are 200 nm.

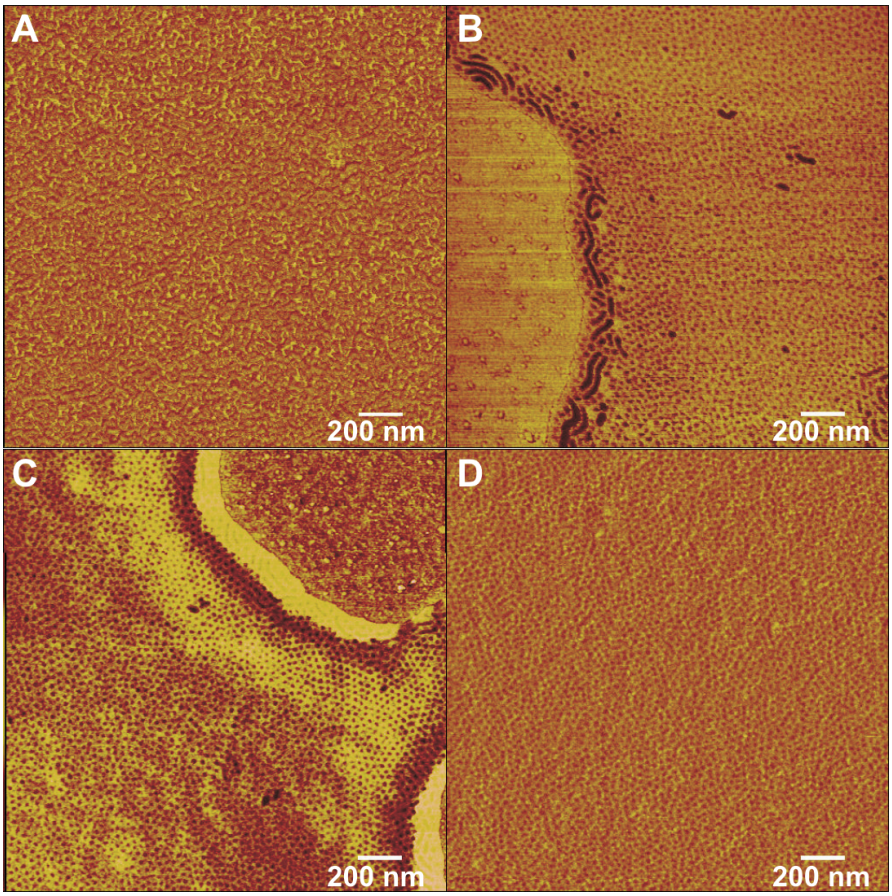

Figure 6.15: AFM-TM phase images (z-range is 30-60°), illustrating the effect of annealing time at 150 °C on initially 10 nm FL8/34 films as cast (A), after 30 min (B), after 2 h (C), and after 8 h (D). The films shown in images (B) and (C) were initially 10 nm high, and show 15 nm thick relief structures and holes.

6.5 Substrate induced patterns (SINPATs)

In the holes of the surface relief structures, which were formed in the 10 nm thin films, sphere-like features of 5 nm in height were found (see Figure 6.16, but also Figure 6.12).

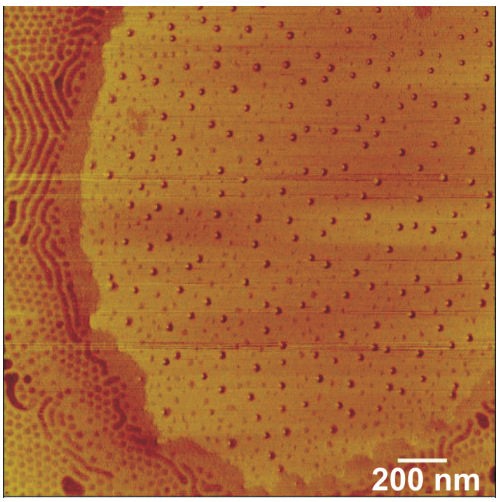

Figure 6.16: TM-AFM phase image (*z*-range is 40°) of a hole in a 10 nm FL8/34 thin film on Si showing substrate induced features (SINPATs).

These features form the so-called substrate induced patterns (SINPATs) caused by the strong adsorption of the PLA block on the substrate, and the subsequent segregation of the PFS block on the PLA layer (see Figure 6.1). Further exploration of these features was done on mica, because of anticipated stronger interactions between mica and PLA.

The average height H of the PFS features was found to be 5 ± 1 nm (see the cross-section in Figure 6.17) and their radius R is 8 ± 2 nm (assuming an AFM tip diameter of ∼10 nm). The number of aggregated PFS chains n_{PFS} in an island can be calculated using the following expression, assuming a spherical cap-like shape of the islands.

$$n_{PFS} = \frac{\frac{\pi}{6}H(3R^2 + H^2)\rho N_A}{M_{n,PFS}} \tag{6.2}$$

where N_A is Avogadro's number, ρ is the density of PFS, and $M_{n,\mathrm{PFS}}$ is the molar mass of the PFS block. This resulted in an average number of aggregated PFS chains in an adsorbed PFS domain of ∼50. The domain size of the

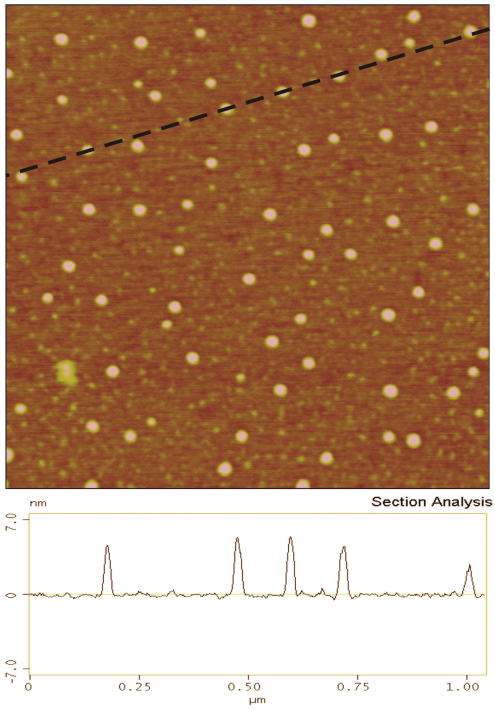

Figure 6.17: AFM-TM height image (z-range is 5 nm) and cross-section of the PFS spheres that segregate on the strongly absorbed PLA blocks on a mica surface.

features is similar to the domain diameters in a typical block copolymer morphology, yet the lateral spacing is much larger. As shown by Spatz *et al.*,[2–4] this spacing can be tuned by varying the length of the adsorbing block, in this case PLA. The pattern we observed was not well ordered. This might be due to the polydispersity of the block copolymers. In the studies by Spatz *et al.*, mainly cylinder and lamellae forming block copolymers were used. Therefore, the small amount of PFS present in the block copolymer used in this study might impose some degree of chain stretching, and the use of cylindrical or even symmetric PFS-*b*-PLA might result in better ordered structures. The formation of two distinct types of nanoscale patterns with the same block copolymer, where one consists of PFS, has not been observed before and is of interest in nanofabrication as another tool to form nanopatterns.

6.6 Conclusions

Successful synthesis of PFS-*b*-PLA, the first example of a block copolymer with an organometallic block and a biodegradable organic block to our knowledge, was demonstrated. The block copolymers were characterized by NMR and GPC for their molecular properties and by SAXS, rheological measurements, and DSC to establish the bulk morphology and thermal behavior. The block copolymers are mainly amorphous and experience an ODT around 135 °C. At higher temperatures, the PLA block becomes chemically liable to chain scission and transesterfication processes, and degradation of the block copolymer sets in. The cleaved chains of mainly PFS or PLA eventually showed the onset of macrophase separation in both bulk and thin films.

Substrate induced patterns (SINPATs) formed in the case of ultra thin films (< 5 nm), which is the first example of these patterns with PFS block copolymers. The SINPATs consisted of strongly substrate-adsorbed PLA blocks on top of which the PFS blocks segregated into sphere-like features with diameters of around 20 nm. The lateral spacing between these features is regular, typically larger than the length-scale associated with block copolymer phase separation, and tunable through the adsorbable block. As a result, two distinct types of patterns are accessible with these block copolymers through tuning of substrate interactions and film thickness. These patterns might serve as templates in the fabrication of functional nanoplatforms. The combination of an organometallic and a biodegradable block offers a range of approaches to selective removal of one block. In addition to reactive ion etching techniques, mild conditions such as hydrolysis might be applicable for selective removal of the PLA phase.

6.7 Experimental

Materials Diisobutylaluminum hydride (1M in toluene), triethylamine, Rochelle salt (Potassium sodium tartrate tetrahydrate, $NaKC_4H_4O_6{\cdot}4H_2O$) and Zn(II) bis[bis(trimethylsilyl)amide] 97% were purchased from Aldrich. Sn(II)-2-ethyl hexanoate and CaH_2 were purchased from Sigma. *D,L*-Lactide was purchased from Purac Biochem and was recrystallized from toluene before usage. Diethyl ether, *n*-heptane, and Silica gel 60 (70 - 230 mesh ASTM) were purchased from Merck. Toluene was dried over *n*-butyllithium and distilled under vacuum. Dichloromethane was dried over CaH_2 and distilled under an overpressure of argon. Heptane and diethyl ether were dried over CaH_2.
Instrumentation 2D ^{1}H NMR correlation spectroscopy (COSY) was performed on a Varian Unity 400 spectrometer at 399.9 MHz. Thermal degrada-

tion was measured on a Perkin-Elmer thermogravimetric analyzer (TGA) 7, with a heating rate of 30 °C/min. AFM imaging on films that were etched with reactive ion etching was performed with the amplitude of oscillation at free vibration (A_0) set at 1.5 V, and with the operating setpoint ratio (A/A_0) set at 0.9. The unetched thin films could be studied best at higher amplitudes of oscillation at free vibration (A_0 = 2.5 V) and an operating setpoint ratio of 0.7. Height and phase images were recorded at a scanning rate of 1 Hz. Hydrolysis of the PLA phase in thin films was carried out in a 40:60 methanol/MilliQ solution containing 0.5 M NaOH as described by others.[16]

Macroinitiator The synthesis of the macroinitiator was performed in an Mbraun glovebox, purged with prepurified nitrogen ($[H_2O] < 0.1$ ppm). PFDMS polymerization was initiated as described elsewhere (Section 3.5). The living chain ends were terminated by approximately 0.2 mL 3-(*tert*-butyldimethylsiloxy)propyldimethylchlorosilane after 20-40 min at room temperature. After 1 to 2 h the reaction mixture was precipitated in a vigorously stirred ten-fold excess of methanol containing 3 mL of triethylamine. The triethylamine trapped any formed HCl, which is the product of unreacted endcapper with methanol. The endcapping efficiency was around 65%. Efficiency <100% is likely caused by the presence of impurities in the endcapper reactant. These impurities could be removed by adding 10-20 mol% *sec*-butyllithium to a solution of 0.2 mL endcapper in 1 mL THF, which was immediately added to the living PFS solution. This method of endcapping resulted in an endfunctionalization efficiency of >95%, as determined by ^{1}H NMR. Column chromatography was used to obtain 100% hydroxyl-terminated PFS. An amount of 0.5 mL diisobutylaluminum hydride (DIBAL) was added to a solution of the protected hydroxy terminated PFS in 5 mL dichloromethane and stirred for 48 h. The addition of a few drops of methanol, to destroy excess DIBAL, and 5 mL 1.5 M aqueous Rochelle salt solution to remove aluminum salts, resulted in a gel-like substance. After a few minutes, two phases were formed that were stirred for 24 h. The aqueous phase appeared opaque, probably due to dissolved aluminum salts. After removing the aqueous layer, the dichloromethane solution was washed twice by vigorous stirring with 5 mL deionized water for two h. The PFS was subsequently precipitated in methanol, dried, dissolved in toluene and fractionated on a silica gel column ($63\ \mu m < d_{SiO_x} < 40\ \mu m$) with toluene as eluent, to separate the deprotected end-functionalized PFS polymers from the non-functionalized PFS polymer. The retention ratio of hydroxyl terminated PFS and nonfunctionalized and protected PFS polymers was 0.75. Toluene was removed by rotary evaporation and the macroinitiator was thoroughly dried in vacuum. This resulted in 100% hydroxyl terminated PFS, that was used for the ring-opening polymerization of the lactide.

PFS-*b*-PLA *D,L*-lactide was purified by recrystallization from dry toluene

just before copolymerization, and added to a toluene solution of macroinitiator. Polymerization with Sn(II)-2-ethyl hexanoate catalyst was initiated by adding a molar equivalent of catalyst of a fresh 1 wt% stock solution with respect to the macroinitiator . Polymerization was allowed to proceed for 24 h at 100 °C. Polymerization with Zn bis[bis(trimethylsilyl)amide] catalyst proceeded by dissolving macroinitiator with a double molar equivalent of a fresh 1 wt% toluene solution of catalyst. After 10 min, a dichloromethane solution of lactide monomer was added, resulting in a 1 M monomer concentration. An increase in viscosity after 30 min indicated successful polymerization. The total reaction time was 2 h, carried out at room temperature. Precipitation in a ten-fold excess of methanol, and subsequent washing and drying resulted in yellow colored block copolymer. **Thin films** Thin films of PFS-*b*-PLA on silicon, mica and silicon modified with octadecyltrichlorosilane were prepared as described elsewhere (see Chapter 4), from 0.25 - 5 wt% solutions of PFS-*b*-PLA in toluene. Film thicknesses varied between 8 and 182 nm. The thin films were imaged by AFM directly or after an additional annealing step (performed in a vacuum oven).

Bibliography

[1] Segalman, R. A., Yokoyama, H. and Kramer, E. J., *Adv. Mater.*, 2001, 13, 1152-1155.

[2] Spatz, J. P., Sheiko, S. and Möller, M., *Adv. Mater.*, 1996, 8, 513-517.

[3] Spatz, J. P., Möller, M., Noeske, M., Behm, R. J. and Pietralla, M., *Macromolecules*, 1997, 30, 3874-3880.

[4] Spatz, J. P., Eibeck, P., Mossmer, S., Möller, M., Herzog, T. and Ziemann, P., *Adv. Mater.*, 1998, 10, 849-852.

[5] Wang, X. -S., Winnik, M. A. and Manners, I., *Macromol. Rapid Comm.*, 2002, 23, 210-213.

[6] Korczagin, I., Hempenius, M. A. and Vancso, G. J., *Macromolecules*, 2004, 37, 1686-1690.

[7] Datta, U. and Rehahn, M., *Macromol. Rapid Comm.*, 2004, 25, 1615-1622.

[8] Kloninger, C. and Rehahn, M., *Macromolecules*, 2004, 37, 1720-1727.

[9] Korczagin, I., Hempenius, M. A., Fokkink, R. G., Stuart, M. A. C., Al-Hussein, M., Bomans, P. H. H., Frederik, P. M. and Vancso, G. J., *Macromolecules*, 2006, 39, 2306-2315.

[10] Odian, G., *Principles of Polymerization*, Wiley, New York, 3d ed., 1991.

[11] Ye, W. P., Du, F. S., Jin, J. Y., Yang, J. Y. and Xu, Y., *React. Funct. Polym.*, 1997, 32, 161-168.

[12] Zhao, Y., Fu, J., Ng, D. K. P. and Wu, C., *Macromol. Biosci.*, 2004, 4, 901-906.

[13] Sherwood, L., *Human Physiology: From Cells to Systems*, Brooks/Cole, Pacific Grove, 4th ed., 2001.

[14] Schmidt, S. C. and Hillmyer, M. A., *Macromolecules*, 1999, 32, 4794-4801.

[15] Schmidt, S. C. and Hillmyer, M. A., *J. Polym. Sci., Part B: Polym. Phys.*, 2002, 40, 2364-2376.

[16] Zalusky, A. S., Olayo-Valles, R., Taylor, C. J. and Hillmyer, M. A., *J. Am. Chem. Soc.*, 2001, 123, 1519-1520.

[17] Crossland, E. J. W., Luwigs, S., Hillmyer, M. A. and Steiner, U., *Soft Matter*, 2007, 3, 94-98.

[18] Zalusky, A. S., Olayo-Valles, R., Wolf, J. H. and Hillmyer, M. A., *J. Am. Chem. Soc.*, 2002, 124, 12761-12773.

[19] Olayo-Valles, R., Lund, M. S., Leighton, C. and Hillmyer, M. A., *J. Mater. Chem.*, 2004, 14, 2729-2731.

[20] Stridsberg, K. M., Ryner, M. and Albertsson, A. C., In *Adv. Polym. Sci.*, 2002, 157, 41-65.

[21] Ryner, M., Stridsberg, K., Albertsson, A. C., Von Schenck, H. and Svensson, M., *Macromolecules*, 2001, 34, 3877-3881.

[22] Peters, M. A., Belu, A. M., Linton, R. W., Dupray, L., Meyer, T. J. and Desimone, J. M., *J. Am. Chem. Soc.*, 1995, 117, 3380-3388.

[23] Hamley, I. W., *Developments in Block Copolymer Science and Technology*, John Wiley and Sons, Hoboken, 2004.

[24] Eitouni, H. B., Balsara, N. P., Hahn, H., Pople, J. A. and Hempenius, M. A., *Macromolecules*, 2002, 35, 7765-7772.

[25] Lammertink, R. G. H., Hempenius, M. A., Manners, I. and Vancso, G. J., *Macromolecules*, 1998, 31, 795-800.

[26] Ringard-Lefebvre, C. and Baszkin, A., *Langmuir*, 1994, 10, 2376-2381.

[27] Olayo-Valles, R., Guo, S. W., Lund, M. S., Leighton, C. and Hillmyer, M. A., *Macromolecules*, 2005, 38, 10101-10108.

CHAPTER 7

Templated growth of carbon nanotubes with controlled diameters using PS-*b*-PFS

Block copolymer thin films fabricated from polystyrene-polyferrocenylsilane (PS-*b*-PFS) block copolymers on silicon substrates were used as precursors of well-ordered, nanosized growth catalysts for carbon nanotubes (CNTs). The size of the catalytic domains was tuned by varying the molecular weight of the block copolymer, enabling control of the diameter of the CNTs grown from these substrates. Using acetylene with an additional hydrogen flow as gas feed, decreasing CNT diameters with decreasing domain sizes were observed. Multiwalled CNTs with inner and outer diameters of 4 and 7 nm, respectively, and a narrow diameter distribution were obtained.

*This chapter has been published: Roerdink, M., Pragt, J., Korczagin, I., Hempenius, M. A, Stöckli, T., Keles, Y., Knapp, H. F., Hinderling, C., and Vancso, G. J., *J. Nanosci. Nanotechnol.*, 2007, 7, 1052-1058.

7.1 Introduction

Carbon nanotubes (CNTs), first reported by Iijima and co-workers,[1] have attracted much interest due to their fascinating electrical and mechanical properties. Consisting of only carbon organized in graphite-like sheets, the tubes typically have lengths on the order of micrometers and circumferences that can go down to 10 carbon atoms. Due to the near-ideal structural organization and the unusual dimensions, exceptional mechanical, electrical and phonon propagating properties are observed in CNTs for both single-walled nanotubes (SWNTs), consisting of just one graphite sheet, and tubes with multiple walls (MWNTs).[2] The areas of application where CNTs are considered range from use in electronic (nano)devices, field emission or superconductivity applications, to reinforcing fibers due to the exceptional high density-normalized strength and modulus, and superplasticity.[3–5] CNTs are usually fabricated using the arc-discharge method[1,6], laser ablation[7] or chemical vapor deposition.[8] Control over the type of CNT (SWNT or MWNT) and the quality (number of defects) is typically better in the case of the first two methods, but both techniques are time consuming, either due to the process itself, or to the necessary purification steps[9,10]. For larger scale CNT growth, chemical vapor deposition (CVD) is the method of choice, in which a carbon gas feed is led over a catalyst material at temperatures between 500 and 1000 °C. Due to the relatively low temperatures used in CVD, the CNTs obtained in this way typically have a larger number of defects.[9] Optimizing conditions in CVD processes to gain a better control over the number of defects in the tubes, orientation, tube diameters and number of walls is therefore important. One method to obtain control over the tube diameter and the number of walls is using small catalyst particles, as several groups have observed a strong correlation between the diameter of the CNTs and the size of the catalyst particles.[11–13] Small diameter catalyst particles have been produced by evaporating thin metal films follwed by fractionating these films thermally or by ageing, as well as by the assembling of metallic ions from solution during annealing.[14–16] Zhang *et al.*[17] showed SWNTs grown from Fe(III) particles with a size of 1-3 nm that were prevented from agglomeration by a calcinated protein ferritin shell. The diameter of the tubes grown showed a direct correlation to the iron particle size. CNT deposition based on a ferritin precursor was also described by Bonard *et al.*,[18] who used microcontact printing for the patterned deposition of a natural ferritin based catalyst, which resulted in monodisperse nanotubes with mean diameters close to the particle size of approximately 5 nm. Despite these examples, the preparation of nanometer-sized catalyst particles still proves difficult, since agglomeration of the catalyst particles at the temperatures of deposition remains hard to avoid.

PS-*b*-PFS was shown to be an effective, nanostructured growth catalyst for carbon nanotube formation after exposure to O_2-RIE.[19,20] Using CVD, crystalline MWNTs with outer diameters of similar size as the oxidized PFS domains were obtained after a short induction time, as the iron species were reduced from Fe(III) to Fe(II) and Fe(0) in the initial stage of the growth process. Agglomeration of iron from different domains was not observed at the temperatures applied in this process.

Recently, a PFS containing block copolymer, polystyrene-*block*-poly(ferrocenylethylmethylsilane) has also been used as an effective precursor for the preparation of lithographically patterned catalytic surfaces using a bilayer lift-off procedure with a precursor film, resulting in selective deposition of CNTs on the PFS containing areas.[21]

The work described in this chapter focused on finding the optimal conditions for controlling CNT deposition and CNT morphology in the CVD process previously applied by us, using PS-*b*-PFS block copolymers to prepare arrays of catalytic nanodomains. The influence of feed gas composition and variation in block copolymer molar mass on CNT characteristics was explored.

7.2 CNT growth from acetylene

A series of PS-*b*-PFS block copolymers with PFS volume fractions of approximately 20 % and total molar masses of 20-90 kg/mol was prepared (Table 7.1). These block copolymers have an equilibrium morphology of PFS spheres in the PS majority phase. Molar masses were varied to influence the size of the organometallic domains, with the aim to control CNT diameters.

Table 7.1: Characteristics of the block copolymers used for the preparation of the catalytic substrates.

Substrate	M_n[a]	M_w[a]	M_w/M_n[a]	PFS[b]	Domain diameters[c]
	[10^3 kg/mol]	[10^3 kg/mol]		vol%	[nm]
SF65/20[d]	85	89	1.07	20	31.4 ± 3.7
SF34/9	43	45	1.05	18	23.2 ± 3.1
SF13/4	17	19	1.12	20	19.0 ± 2.5

[a]Measured by GPC, relative to polystyrene standards. [b]Calculated from ferrocenyl and polystyrene ^{1}H NMR integrals. [c]Determined from TM-AFM image analysis. [d]Notation for PS-*b*-PFS, with the indication of the M_n of the PS and the PFS block, respectively.

Thin films of block copolymers SF65/20, SF34/9 and SF13/4 on silicon substrates were treated with an oxygen plasma to remove the organic matrix (as described in Chapter 2), and subsequently employed in a CVD process using acetylene as a carbon source.[19] Substrates obtained from SF65/20, the highest molar mass block copolymer, showed the highest surface coverage by CNTs. A micrometer thick layer of hollow tubes was formed over the entire substrate, see Figure 7.1A and Figure 7.1B.

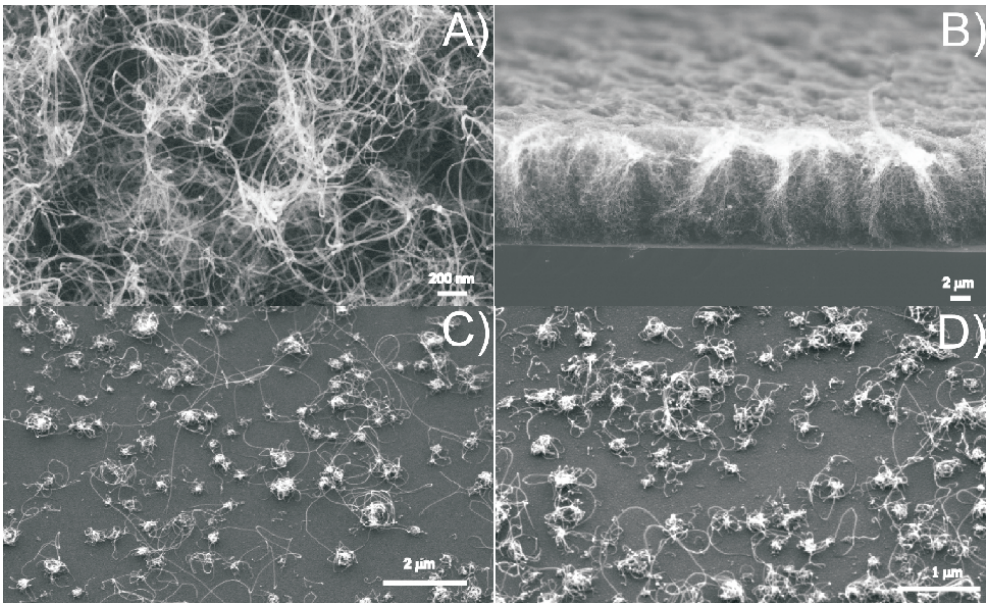

Figure 7.1: SEM images of CNT growth from acetylene on catalytic substrates prepared from SF65/20 (A,B), SF34/9 (C) and SF13/4 (D).

Figure 7.2A shows a TEM image of a typical CNT found on these substrates. The tube shows parallel walls that are well-crystallized, but exhibit some irregularities, due to defects commonly found in CVD grown CNTs. In this representative tube, two iron particles are included, which indicates growth by the tip growth mechanism, where the catalyst particle is lifted-off the surface by the growing tube.[22,23] In this particular tube the catalyst particle apparently has split before the termination of the reaction. Another observation about the nature of growth initiation can be derived from SEM images as shown in Figure 7.2B. The tubes emerge from small islands of amorphous carbon which typically extend over a few precursor domains and are assumed to be either deposited on the substrate before tube initiation starts or are accumulating during tube growth. The CNTs grown from SF65/20 covered substrates were characterized using TEM. Figure 7.3 shows a histogram summarizing measurements on the diameter distribution in the CNTs.

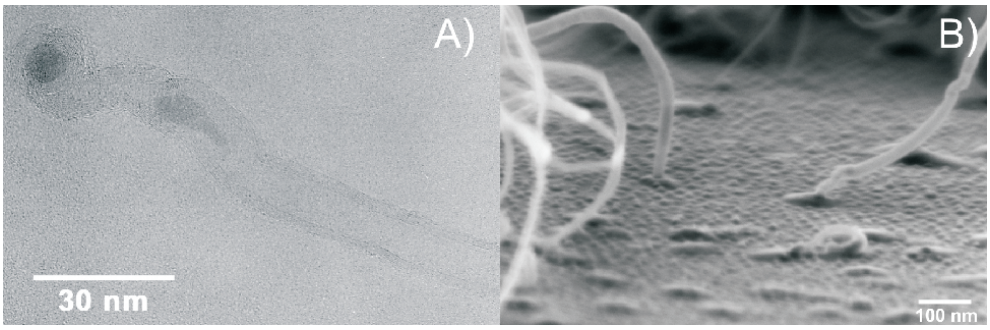

Figure 7.2: TEM image of a typical CNT grown from acetylene and SF65/20 block copolymer catalyst precursor substrate (A). SEM image of typical CNT growth from SF34/9 block copolymer catalyst precursor substrate from acetylene (B).

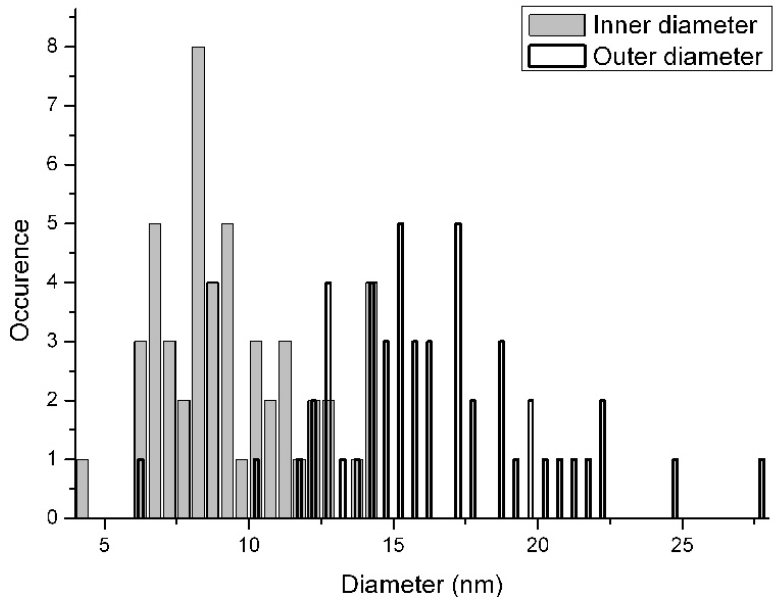

Figure 7.3: Histogram of inner and outer diameters of CNTs deposited from acetylene on catalytic substrates prepared from SF65/20. The diameters were obtained from TEM images.

Multiwalled CNTs with average inner and outer diameters of 8.3 nm (± 2.4 nm) and 15.7 nm (± 5.4 nm), respectively, were obtained. These values are slightly smaller than the diameters of the organometallic domains after O_2-plasma treatment (31 nm). O_2-plasma-treated PFS domains were found to consist of iron and silicon oxides.[24] As Fe(0) is the catalytically active species, Fe(0) particles formed under the reducing conditions and at the high temperatures of the CVD process are expected to have smaller dimensions than their corresponding O_2-plasma exposed domains. During the heating step employed prior to acetylene addition and in the initial phase of CNT growth, the metallic iron present in the block copolymer domains can agglomerate within single domains to form larger Fe(0) particles. Although migration within the domains is highly probable, migration of iron between separate domains is assumed to be highly unlikely, based on the intactness of the domains and the typical block copolymer-like array after the heat treatment. Thus, the iron agglomerates present on the catalytic substrate can be expected to have diameters smaller than those of the oxidized PFS domains due to the limited amount of iron present in each domain. The smaller iron oxide domains formed from the lower molar mass SF34/9 and SF13/4 block copolymers were somewhat less effective catalyst precursors in the presence of acetylene, compared to domains from SF65/20, see Figure 7.1C and Figure 7.1D.

7.3 CNT growth from acetylene and hydrogen

A more efficient reduction of the iron oxides to metallic iron was required, in order to enhance catalyst activity. Since the gas composition during CVD is known to have a strong effect on the CNT deposition, variations of the CVD process and their influence on CNT deposition and tube morphology were explored. Prereaction annealing using two different schemes from the thus far employed CVD process were considered. The substrates were equilibrated for 4 h at reaction temperature while a N_2 flow was led over the substrates. The effect of this long annealing in N_2 atmosphere was an increased deposition of CNTs on all substrates, which can be attributed to the thermal degradation of the PFS domains to iron silicon carbides at this temperature, resulting in more catalytically active species during the reaction.[25] In contrast to these findings, the CNT deposition was strongly reduced in case of long annealing at reaction temperature with a small flow of H_2 added to the N_2 flow. Under these conditions more diffusion of iron in the silicon wafer may take place as a result of reduction of PFS by the hydrogen, resulting in the formation of the catalytically inactive iron silicides.[26,27] The CVD process was then varied by adding a small flow of H_2 during equilibration of the substrates and to the acetylene flow during the reaction, since the addition of H_2 is known to aid the

formation of SWNTs, decrease the formation of amorphous carbon deposition, and enable the synthesis of smaller diameter tubes.[28–30] The addition of H_2 resulted in a significant increase in CNT deposition on the substrates prepared form SF34/9 and SF13/4, see Figure 7.4 in comparison with Figure 7.1.

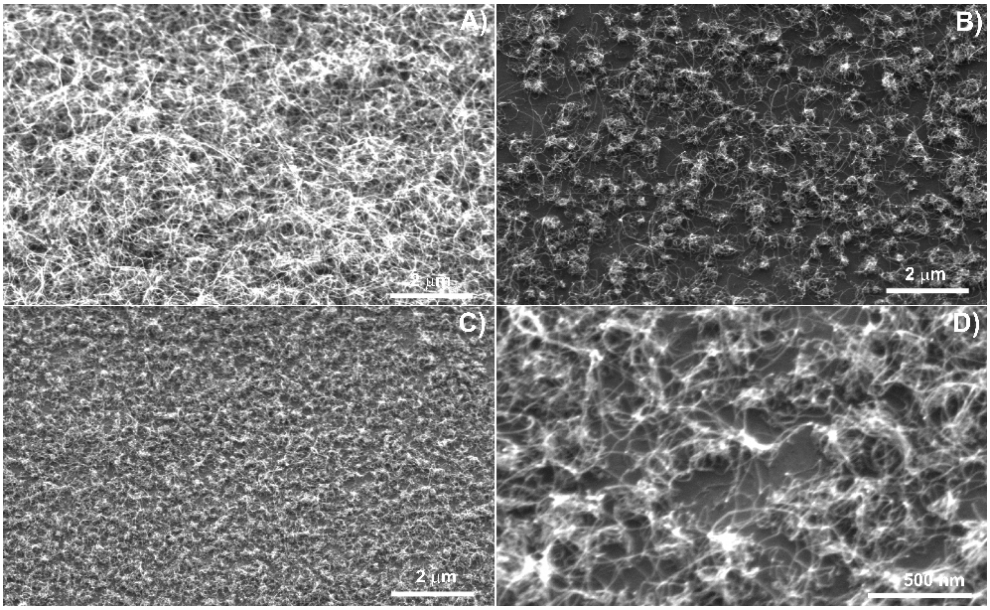

Figure 7.4: SEM images of CNT growth from acetylene in the presence of H_2 on catalytic substrates prepared from SF65/20 (A), SF34/9 (B) and SF13/4 (C,D).

Considering the reductive role hydrogen plays, H_2 is assumed to enhance the reduction of the iron species present in the precursor domains to the catalytically active form, thus strongly increasing the CNT deposition. The CNTs deposited on SF34/9 decorated substrates were analyzed by TEM and inner and outer diameters of 4.2 ($\pm$ 2.0 nm) and 7.1 nm ($\pm$ 2.2 nm) were found, respectively, using acetylene and H_2, as can be seen in Figure 7.5. Figure 7.6 shows a TEM image of typical tubes obtained using SF34/9 prepared substrates under these conditions. On the substrate prepared from SF65/20 a decrease in wall thickness of the tubes deposited under these conditions was observed, *i.e.* no significant decrease in outer diameter was found, but the inner diameter increased, when compared to the tubes obtained on these substrates using only acetylene. The significant decrease in tube diameter found on SF34/9 prepared substrates compared to tubes on SF65/20 prepared substrates indicates a strong influence of the catalytic domain size on the tube diameter when using an acetylene and H_2 gas feed. Further, the distribution of tube diameters was narrower than found when using only an acetylene feed

gas. This demonstrates that the tube diameter can be controlled under these conditions by tuning the molar mass of the block copolymer used to prepare the catalyst substrate.

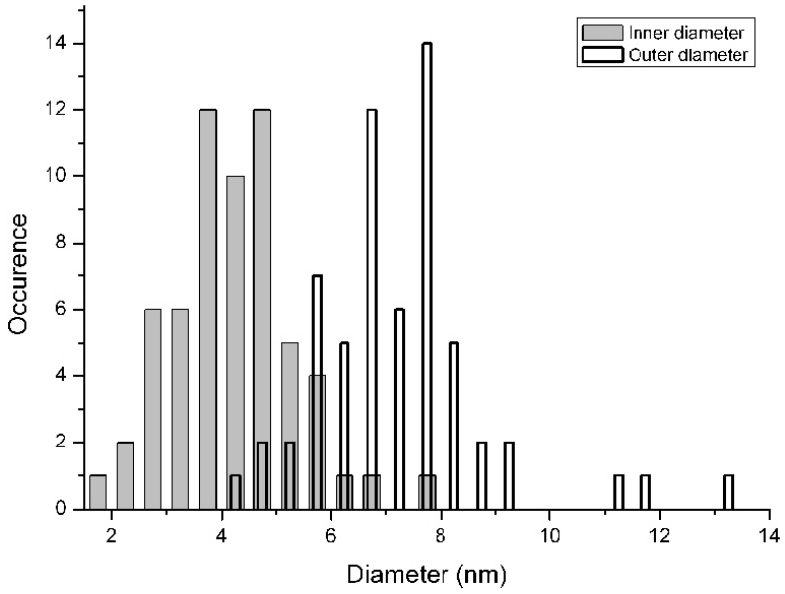

Figure 7.5: Histogram of inner and outer diameters of CNTs growth from acetylene in the presence of H_2 on catalytic substrates prepared from SF34/9. The diameters where obtained from TEM images.

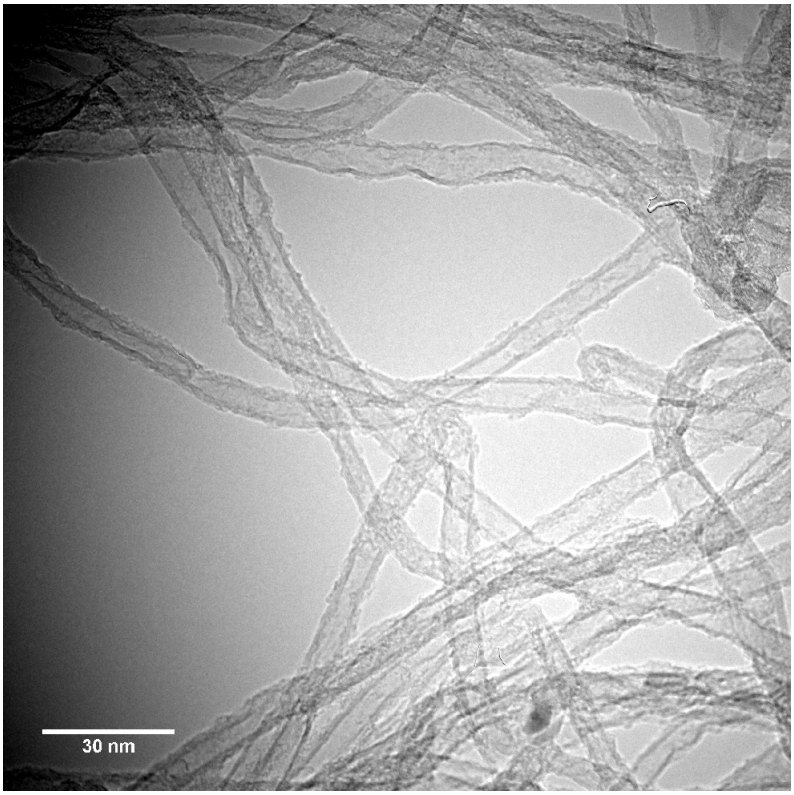

Figure 7.6: TEM image of CNT's grown from SF34/9 using acetylene and H_2 as gas feed.

7.4 PFS homopolymer films as catalytic precursor

For the purpose of comparison, films of poly(ferrocenyldimethylsilane) homopolymer were subjected to the CVD process. CNT deposition was observed on these films, indicating that PFS homopolymer films are also catalytically active. However, the deposition was very inhomogeneously distributed over the substrate, with large areas having no tubes at all and occasionally yielding areas with a dense packing of tubes. Figure 7.7 shows a SEM image of CNT deposition on a substrate prepared from PFS homopolymer. Furthermore, as can be seen in Figure 7.7, large globular deposits of amorphous carbon where found on these substrates, which were not observed on substrates prepared from block copolymers.

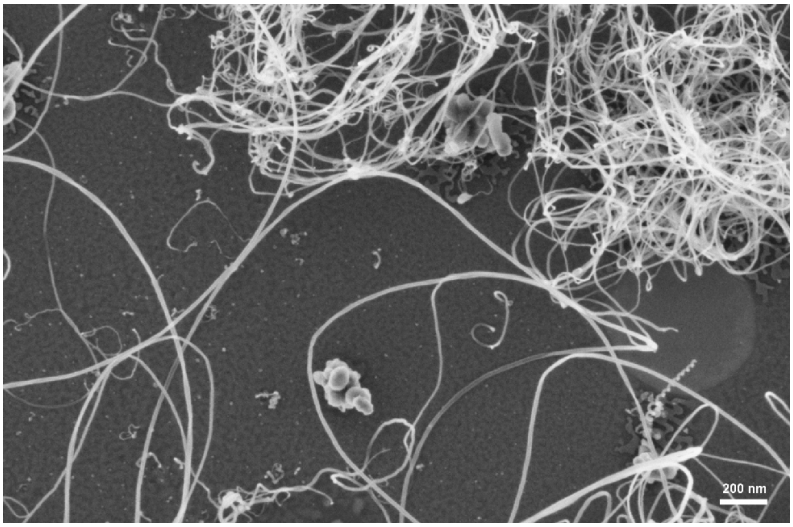

Figure 7.7: SEM image of CNT growth from acetylene on a PFS homopolymer film.

7.5 Conclusions

Arrays of nanometer-sized catalytic domains, prepared from PS-*b*-PFS block copolymers, were used for growing carbon nanotubes in a CVD process. Variations in both gas composition and in annealing steps strongly influenced the amount of deposition and the morphology of the carbon nanotubes deposited. In the presence of hydrogen and using acetylene as a carbon source, the CNT diameters could be influenced by tuning the molar mass of the block copolymer used as a catalyst precursor, resulting in decreasing diameters with decreasing domain size as well as narrow diameter distributions.

7.6 Experimental

PS-*b*-PFSs were prepared as described earlier (see Chapter 4). Film thicknesses ranged from 20 nm to 68 nm, so as to yield a film with only one monolayer of microphase separated spherical domains. Film thicknesses were established by ellipsometry, using a wavelength of 632.8 nm and a fixed angle of 70°, and a refractive index of 1.54. Thin films of PS-*b*-PFS were annealed under vacuum at 160 °C for 2 days (SF14/5), 4 days (SF34/9) or 6 days (SF65/20). Oxygen reactive ion etching (O_2-RIE) (Elektrotech PF 340 apparatus) was carried out on the PS-*b*-PFS films with a pressure inside the etching chamber of 10 mTorr, the substrate temperature was set at 10 °C,

an O_2 flow rate of 20 sccm was maintained, and power was set at 75 W. The thin films were etched for 10 s. O_2-RIE (Oxford Plasmalab 80 plus) on homopolymer PFS films was carried out for 3 min using 30 mTorr O_2 and 30 W RF power. CNT synthesis was performed in a dedicated CVD thermal reactor. The growth temperature was 720 °C (acetylene) and the pressure was 700 mbar. The carbon source was 15 sccm acetylene (and optional 8.25 sccm H_2) diluted in N_2 flowing at a rate of 1000 sccm over the catalyst coated substrate. The catalyst coated substrates were heated to the reaction temperature and either allowed to equilibrate for 30 min or pre-annealed for 4 h, during which an optional flow of 8.25 sccm H_2 was led over the substrates. Reaction was completed by flowing N_2 through the reaction chamber at the reaction temperature for 5 min and subsequent cooling to room temperature under vacuum. The substrates containing CNTs were analyzed using scanning (SEM) or transmission electron microscopy (TEM, Philips CM30). For TEM, the samples were prepared by scraping the deposit from the catalytic substrate and sonicating the deposit in ethanol. Drops of this suspension were successively deposited onto carbon-coated microscopy grids and blotted dry.

Bibliography

[1] Iijima, S., *Nature*, 1991, 354, 56-58.

[2] Dresselhaus, M. S., Dresselhaus, G. and Jorio, A., *Annu. Rev. Mater. Res.*, 2004, 34, 247-278.

[3] Baughman, R. H., Zakhidov, A. A. and De Heer, W. A., *Science*, 297, 787-792.

[4] Wong, E. W., Sheehan, P. E. and Lieber, C. M., *Science*, 277, 1971-1975.

[5] Huang, J. Y., Chen, S., Wang, Z. Q., Kempa, K., Wang, Y. M., Jo, S. H., Chen, G., Dresselhaus, M. S. and Ren, Z. F., *Nature*, 2006, 439, 281.

[6] Bethune, D. S., Kiang, C. H., Devries, M. S., Gorman, G., Savoy, R., Vazquez, J. and Beyers, R., *Nature*, 1993, 363, 605-607.

[7] Chen, M., Chen, C. M. and Chen, C. F., *J. Mater. Sci.*, 2002, 37, 3561-3567.

[8] Kong, J., Soh, H. T., Cassell, A. M., Quate, C. F. and Dai, H. J., *Nature*, 1998, 395, 878-881.

[9] Thien-Nga, L., Bonard, J. M., Gaal, R., Forro, L. and Hernadi, K., *Appl. Phys. Lett.*, 2002, 80, 850-852.

[10] Thien-Nga, L., Hernadi, K., Ljubovic, E., Garaj, S. and Forro, L., *Nano Lett.*, 2002, 2, 1349-1352.

[11] Cheung, C. L., Kurtz, A., Park, H. and Lieber, C. M., *J. Phys. Chem. B*, 2002, 106, 2429-2433.

[12] Dai, H., Rinzler, A. G., Nikolaev, P., Thess, A., Colbert, D. T. and Smalley, R. E., *Chem. Phys. Lett.*, 1996, 260, 471-475.

[13] Ren, Z. F., Huang, Z. P., Wang, D. Z., Wen, J. G., Xu, J. W., Wang, J. H., Calvet, L. E., Chen, J., Klemic, J. F. and Reed, M. A., *Appl. Phys. Lett.*, 1999, 75, 1086-1088.

[14] Cassell, A. M., Verma, S., Delzeit, L., Meyyappan, M. and Han, J., *Langmuir*, 2001, 17, 260-264.

[15] Chhowalla, M., Teo, K. B. K., Ducati, C., Rupesinghe, N. L., Amaratunga, G. A. J., Ferrari, A. C., Roy, D., Robertson, J. and Milne, W. I., *J. Appl. Phys.*, 2001, 90, 5308-5317.

[16] Kind, H., Bonard, J. M., Emmenegger, C., Nilsson, L. O., Hernadi, K., Maillard-Schaller, E., Schlapbach, L., Forro, L. and Kern, K., *Adv. Mater.*, 1999, 11, 1285-1289.

[17] Zhang, Y., Li, Y., Kim, W., Wang, D. and Dai, H., *Appl. Phys. A*, 2002, 74, 325-328.

[18] Bonard, J. M., Chauvin, P. and Klinke, C., *Nano Lett.*, 2002, 2, 665-667.

[19] Hinderling, C., Keles, Y., Stöckli, T., Knapp, H. F., De los Arcos, T., Oelhafen, P, Korczagin, I., Hempenius, M. A., Vancso, G. J., Pugin, R. and Heinzelmann, H., *Adv. Mater.*, 2004, 16, 876-879.

[20] Lastella, S., Jung, Y. J., Yang, H. C., Vajtaj, R., Ajayan, P. M., Ryu, C. Y., Rider, D. A. and Manners, I., *J. Mater. Chem.*, 2004, 14, 1791-1794.

[21] Lu, J. Q., Kopley, T. E., Moll, N., Roitman, D., Chamberlin, D., Fu, Q., Liu, J., Russell, T. P., Rider, D. A., Manners, I. and Winnik, M. A., *Chem. Mater.*, 2005, 17, 2227-2231.

[22] Vajtai, R., Wei, B. Q., Zhang, Z. J., Jung, Y., Ramanath, G. and Ajayan, P. M., *Smart Mater. Struct.*, 2002, 11, 691-698.

[23] Meyyappan, M., Delzeit, L., Cassell, A. and Hash, D., *Plasma Sources Sci. Technol.*, 2003, 12, 205-216.

[24] Lammertink, R. G. H., Hempenius, M. A., Chan, V. Z. -H., Thomas, E. L. and Vancso, G. J., *Chem. Mater.*, 2001, 13, 429-434.

[25] Petersen, R., Foucher, D. A., Tang, B. Z., Lough, A., Raju, N. P., Greedan, J. E. and Manners, I., *Chem. Mater.*, 1995, 7, 2045-2053.

[26] De los Arcos, T., Vonau, F., Garnier, M. G., Thommen, V., Boyen, H. G., Oelhafen, P., Duggelin, M., Mathis, D. and Guggenheim, R., *Appl. Phys. Lett.*, 2002, 80, 2383-2385.

[27] Jung, Y. J., Wei, B. Q., Vajtai, R., Ajayan, P. M., Homma, Y., Prabhakaran, K. and Ogino, T., *Nano Lett.*, 2003, 3, 561-564.

[28] Dong, L., Jiao, J., Foxley, S., Tuggle, D. W., Mosher, C. L. and Grathoff, G. H., *J. Nanosci. Nanotechnol.*, 2002, 2, 155-160.

[29] Franklin, N. R., Li, Y. M., Chen, R. J., Javey, A. and Dai, H. J., *Appl. Phys. Lett.*, 2001, 79, 4571-4573.

[30] Oberlin, A., Endo, M. and Koyama, T., *J. Crystal Growth*, 1976, 32, 335-349.

CHAPTER 8

Outlook: Amine-terminated PFS for novel self-assembled structures

PFS are highly interesting polymers due to their unusual properties caused by the presence of iron, as discussed in this thesis. As a result of this functionality, PFS polymers or block copolymers containing PFS are close to actual applications including for instance the fabrication of functional nanostructured surfaces or stimulus-responsive polymer architectures such as redox-responsive capsules. The functional structures are formed in self-assembly processes.

Substrate interactions can be a simple and highly useful tool in directing block copolymer self-assembly. The positional control of microdomains of PFS through substrate interactions finds application in data storage, but one can also imagine utilization in sensor applications, when considering for example cylindrical structures. Sensing of molecules can take place making use of several properties of PFS, such as redox responsiveness, or quenching of the photoluminescence of small dye molecules, a property demonstrated for PFS. The sensing studies have been carried out mainly in bulk, but it seems highly relevant to extend these studies to supported films and to probe the effect of a substrate on these properties.

The chemical contrast that the organometallic nature of PFS provides compared to organic polymers can be considered the main asset of PFS. Work on PFS has thus far covered lithography, catalytic activity in carbon nanotube growth, redox responsiveness, formation of ceramic structures, formation of cylindrical micelles that can be selectively loaded with metals, as well as photoluminescent quenching. All these areas are application-oriented and demonstrate the versatility of PFS. In addition, the chemical contrast facilitates for

instance imaging, scattering or spectroscopic monitoring, due to the particular intrinsic properties of PFS, where similar studies with other organic polymers might be complicated, if not inaccessible at all, due to lack of contrast.

Throughout this thesis, the etch contrast of PFS has been employed to study underlying physical principles of ordering under different conditions. This was, with exception of the last chapter, remote from real technological applications. For example, the resistance to reactive ion etching facilitated imaging of phase separated structures in thin films. Similarly, PFS provided the contrast in small-angle X-ray scattering without the need for staining. Therefore, PFSs may be very useful in more fundamental studies, enabling the study of phase separation in new types of polymers, which have different types of blocks or block junctions.

When exploring options for creating novel block copolymers, end-functionalization of PFS chains proves to be relevant for introducing blocks grown by routes other than anionic polymerization. The functionalization of polymers with reactive end groups allows such materials to be applied in surface functionalization and in the formation of novel block and graft copolymers. End-capping of living polymers obtained by anionic polymerization, such as polystyryllithium and polybutadienyllithium, has been pursued actively in the last decades and a variety of reagents for introducing *e.g.* hydroxyl-, amine, thiol and carboxylic acid groups have been established. One class of end-capping reagents that has proved to be particularly effective for introducing hydroxyl or amine end groups combines a chlorosilyl moiety and OH or NH_2 functions, protected as silyl ethers or silazanes, respectively. Chlorosilanes react quantitatively with a range of living polymer anions but haloalkanes have also been employed successfully. The end-functionalization of living poly(ferrocenyldimethylsilane) chains with hydroxyl and primary amine groups has recently been reported, to produce PFS-*b*-PMMA[1] and PFS-*b*-polypeptide diblock copolymers.[2] Another example was described in this thesis, where PFS-*b*-PLA block copolymers were synthesized through hydroxyl-endcapping. The obtained polymers demonstrated an interesting combination of functionalities by the combination of an organometallic block with a biodegradable block. One can envisage investigating the selective removal of the PLA block not only by mild hydrolytic conditions, but also via enzymatic degradation, which would constitute a novel tool for the fabrication of functional nanoplatforms.

End functionalization enables the design of specific endgroups or units at the junction of two blocks. Particularly, through amino-endcapping, self-complementary groups such as ureidopyrimidinone (UPy) and ureidotriazine (UTr) groups[2] can be introduced as an endgroup of PFS, and block copolymers where the separate blocks are linked together by multiple H-bonding interactions can be obtained.

Amine end-functional PFS and PI can be linked by isocyanate chemistry to form a block copolymer with a bisurea unit at the block junction. The presence of such a H-bonding motif is expected to enhance phase separation and allows one to explore the lateral association of these motifs, perhaps leading to novel self-assembled structures in thin films and in solution.[3]

As a part of this thesis, the synthesis of an amine endfunctionalized PFS was undertaken. The end-capping reagent used was a chlorosilane, which was obtained by hydrosilylation of an *N*-allyl disilazane as shown in Figure 8.1. The functionalization of living PFS is schematically shown in Figure 8.2. An end-capping efficiency of >70 % was reached, as gauged by ^1H NMR. This efficiency is higher than the one observed for α-haloalkyl-based endcapping reagents (40%). PFS-NH_2 (as well as PS-NH_2 and PI-NH_2) could be purified by column chromatography, which removed unterminated polymer.

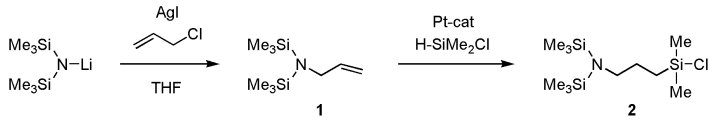

Figure 8.1: Synthesis of the amine endcapper.

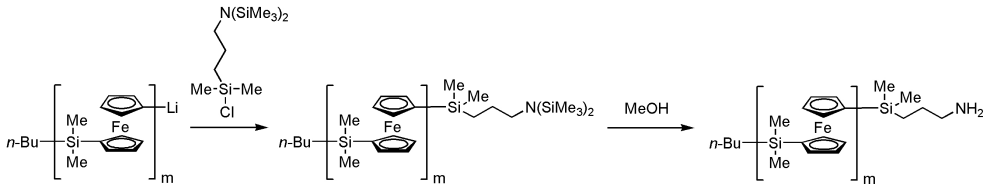

Figure 8.2: End-functionalization of living PFS chains with a primary amine group.

8.1 Experimental

3-[*N,N*-bis(trimethylsilyl)amino]-1-propene (**1**) A dry 250 mL two-necked flask equipped with a stirring bar and septum was connected to a Schlenk line. AgI (9.9 g, 0.042 mol) was added, protected from light. After evacuating and filling with argon for three times, the flask was placed in a water bath and $LiN(SiMe_3)_2$ in THF (100 mL, 0.1 mol) was added and stirring was continued for 22 h. Ice was added to the water bath to reach 10 °C followed by the portion wise addition of allyl chloride (8.61 g, 0.112 mol). The mixture was stirred overnight at room temperature. About 50% of the THF was evaporated and replaced by *n*-hexane. The salts were left to settle and the solution was transferred into a vacuum distillation setup. Hexane was distilled off at ambient pressure under argon, using a Schlenk line. The product, a colorless liquid, was distilled into an ampoule (bp 50-60 °C, 9 mbar), lit.: bp 60 °C/ 16 mmHg.[4] Isolated yield 14.83 g (73.6 mmol, 74 %).[5–7]

1-(Chlorodimethylsilyl)-3-[*N,N*-bis(trimethylsilyl)amino]propane (**2**) The *N*-allyl disilazane was hydrosilylated with dimethylchlorosilane and chloroplatinic acid under argon as described by DeSimone *et al.*[8]

Amine-terminated homopolymers 0.2 mL THF, and 10-20 mol% *sec*-butyllithium were added to 20 equivalents of chlorosilane to scavenge any impurities. The mixture was directly added to living polymer solutions of PFS, PS or PI, prepared as described earlier. After 2 h, the polymer was precipitated in a mixture of a 10-fold excess of methanol and 3 mL of triethylamine. Column chromatography, using a dichloromethane/THF mixture, was used to obtain 70-100% amine-terminated PFS.

Bibliography

[1] Korczagin, I., Hempenius, M. A. and Vancso, G. J., *Macromolecules*, 2004, 37, 1686-1690.

[2] Kim, K. T., Vandermeulen, G. W. M., Winnik, M. A. and Manners, I., *Macromolecules*, 2005, 38, 4958-4961.

[3] Kautz, H., Van Beek, D. J. M., Sijbesma, R. P. and Meijer, E. W., *Macromolecules*, 2006, 39, 4265-4267.

[4] Bestmann, H. J. and Wölfel, G., *Chem. Ber.*, 1984, 117, 1250-1254.

[5] Kukula, H., Schlaad, H., Falkenhagen, J. and Kr uger, R. -P., *Macromolecules*, 2002, 35, 7157-7160.

[6] Murai, T. and Yamamoto, M. and Kato, S., *Chem. Commun.*, 1990, 789.

[7] Murai, T., Yamamoto, M., Kondo, S. and Kato, S., *J. Org. Chem.*, 1993, 58, 7440-7445.

[8] Peters, M. A., Belu, A. M., Linton, R. W., Dupray, L., Meyer, T. J. and Desimone, J. M., *J. Am. Chem. Soc.*, 1995, 117, 3380-3388.

CHAPTER 9

Summary

The work described in this thesis aimed at gaining a better understanding of factors involved in directed self-assembly of block copolymer microdomains. For many possible applications of block copolymers, such as high density data storage, the positional control of microdomains is crucial. Understanding the mechanisms governing the ordering in phase separated block copolymers is therefore fundamental for designing usable systems. In this study, organic-organometallic block copolymers were used, in which the organometallic block was poly(ferrocenylsilane) (PFS). The presence of iron in the backbone of these polymers imparts properties such as etch resistance or catalytic activity to the polymers. Therefore, PFS containing block copolymers can directly be used as nanolithographic templates or for the fabrication of a catalytic platform of nanosized domains.

Two different approaches were explored and are described in this thesis. The first approach involved the study of the effect of chemical and topographical modifications of a substrate on the morphology of one particular type of diblock copolymer. The second method involved the study of polymer-substrate interactions in diblock copolymers with different chemistry.

Chapter 1 and *Chapter* 2 give a general introduction to the scope of the work and to phase separation in block copolymers. Particular attention was given to ordered morphologies in bulk and in supported films of asymmetric block copolymers, where spherical domains of one phase exist in a matrix of the other. A number of techniques that were used to probe different aspects of order are discussed. These techniques include structure characterization techniques, such as small-angle X-ray scattering and dynamic secondary ion mass spectrometry, as well as image analysis techniques used to quantify lateral order. The correlation between the information obtained by these different

techniques, and how this information needs to be interpreted for block copolymers in bulk and in thin films is addressed in *Chapter* 2.

In *Chapter* 3 through 5 the synthesis, characterization and a thin film study of amorphous, low-T_g block copolymers are described. The synthesis of amorphous PFS polymers and block copolymers, and their thermal properties in the bulk are discussed in *Chapter* 3. Amorphous PFS was prepared by copolymerization of small amounts of asymmetrically substituted ethylmethyl-[1]silaferrocenophane monomer with dimethyl[1]silaferrocenophane. The corresponding polyisoprene (PI)-*b*-PFS block copolymers showed no crystallization within the studied periods of time. Time-consuming annealing steps to obtain thermodynamic equilibrium were redundant in these copolymers, which makes them attractive for use in thin film applications. An important thermal transition for the choice of the annealing strategy is the order-disorder transition between an ordered phase-separated system and a disordered melt. The order-disorder temperatures were determined for the synthesized block copolymers and were shown to decrease with an increasing amount of incorporated asymmetrically substituted monomer. This dependence on the EM content was probably due to the slightly more aliphatic character of the PFS phase with increasing amount of EM.

The thin film morphology of the PI-*b*-PFSs is discussed in *Chapter* 4. On flat substrates, the amorphous copolymers exhibited an intrinsic large-area ordering, extending over more than 1 micron, which is exceptionally large for block copolymers that generally have grain sizes of only a few hundred nanometer. In films of one monolayer of domains, a hexagonal packing of microdomains was found. A dynamic secondary ion mass spectrometry study revealed the structural transition of this hexagonal packing to a BCC morphology with increasing film thickness. The BCC morphology was oriented with the 110 plane parallel to the substrate throughout the entire film. Both blocks of PI-*b*-PFS were found at the polymer-substrate interface, while in PS-*b*-PFS the PFS wetted the substrate, rendering the substrate wetting for PI-*b*-PFS and PS-*b*-PFS qualitatively different. A study of graphoepitaxial alignment of microdomains (order directed by topographic features on a substrate) with PI-*b*-PFS is therefore of special interest, since the alignment effect in grapoepitaxy has so far been ascribed to the existence of a brush layer of just one phase at the substrate. Such a study is presented in *Chapter* 5. In grooves of one monolayer thickness, the position of the domains was fixed despite the neutral wetting condition. The position of the domains was successfully directed at larger distances from the side-walls in linear and hexagonal grooves of up to 1.3 μm width. The hexagonal pits demonstrated 2D alignment. In circular pits, the graphoepitaxial effect was absent. The strain imposed by curved sidewalls was absorbed by expansion or compression of microdomains near the edge.

Chapter 6 presents the synthesis, characterization and thin film morphology of a different PFS containing block copolymer, to probe the polymer-substrate interactions in case of different chemistry. PFS-*b*-polylactide (PLA) was synthesized using a combination of anionic polymerization and catalyzed ring-opening polymerization. The PLA block constituted a distinctly more polar block. The resulting strong substrate-polymer interactions caused the formation of dewetted aggregates of PFS on top of a strongly substrate-adsorbed PLA layer in ultrathin films (< 10 nm). This polymer, the first example of a block copolymer consisting of an organometallic block and a biodegradable block, enabled the fabrication of two different types of patterns, which might serve as templates for arrays of functional nanodomains. In addition, the PLA enables soft etching methods, through the selective hydrolysis of the PLA. The PFS-*b*-PLA block copolymers were mainly amorphous and exhibited an order-disorder transition around 135 °C. At higher temperatures, chain scission and transesterfication processes of the PLA block became more important, which influenced the thin film morphology.

In *Chapter* 7 the use of PFS containing block copolymers in a catalytic application was explored. The formation of carbon nanotubes (CNTs) with controlled diameters fabricated from PS-*b*-PFS templated catalytic arrays is described. Multiwalled carbon nanotubes with a narrow distribution in diameter were obtained. The diameters could be tuned by varying the molar mass of the block copolymer precursor, using acetylene/hydrogen as the feed gas in chemical vapor deposition. The CNT diameters decreased with decreasing domain sizes.

Preliminary results on amine end-functionalization of PFS are given as an outlook in *Chapter* 8. This functionalization enables new routes for the addition of particular chemical functionalities at the PFS chain end or other organic blocks. Also, specific motifs may be introduced at the junction between two blocks, with the aim of enhancing phase-separation.

CHAPTER 10

Samenvatting

Het in dit proefschrift beschreven werk heeft tot doel om een beter inzicht te verkrijgen in de factoren die een rol spelen in gestuurde zelforganisatie van microdomeinen in fasegescheiden blok copolymeren. Controle over de positie van blok copolymeerdomeinen is van belang in veel toepassingen van blok copolymeren, zoals bijvoorbeeld gegevensopslag met hoge dichtheid. Inzicht in de mechanismen die ordening van domeinen in blok copolymeren bepalen is daarom essentieel voor het ontwikkelen van daadwerkelijk toepasbare systemen. In deze studie zijn organisch-organometaal blok copolymeren gebruikt, waar het organometaal blok gevormd werd door poly(ferrocenylsilane) (PFS). De aanwezigheid van ijzer in de hoofdketen geeft deze polymeren bijzondere eigenschappen voor polymeren, zoals etsweerstand of katalytische eigenschappen. Deze polymeren kunnen daardoor vrij gemakkelijk worden toegepast als nanolithografisch masker of als een platform voor het generen van katalytisch actieve nanostructuren.

Om inzicht te krijgen in de ordeningsmechanismen in blok copolymeren zijn twee verschillende aanpakken gehanteerd. De eerste aanpak omvatte het bestuderen van het effect van chemische en topologische modificaties van een substraat op de morfologie en orde in een specifiek blok copolymeer. De tweede benadering behelsde het bestuderen van polymeer-substraat interacties in blok copolymeren met andere chemische eigenschappen.

Hoofdstuk 1 en *Hoofdstuk* 2 geven het kader van het werk weer en een introductie van fasescheiding in blok copolymeren. Geordende structuren in de bulk en in substraat-ondersteunde dunne lagen van asymmetrische blok copolymeren, waarin bollen van de ene fase in een matrix van de andere fase voorkomen, worden extra toeglicht. Een aantal technieken die verscheidene aspecten van de aanwezige orde van domeinen bepalen worden besproken.

Hiertoe behoren structuurkarakteriserende technieken zoals small angle röntgenverstrooiing en dynamische secundaire ionmassaspectrometrie, en beeldanalysetechnieken die gebruikt worden om laterale orde te kwantificeren. De relatie tussen informatie die uit deze verschillende technieken verkregen wordt, en de relatie met de ordening van de microdomeinen in de polymere bulk en in de dunne lagen is met name van belang in de verdere hoofdstukken en wordt daarom hier uitgelicht.

In de hoofdstukken 3 tot en met 5 wordt de synthese, karakterisatie en een dunne laag studie van amorfe, lage T_g blok copolymeren beschreven. De synthese van amorfe PFS polymeren en blok copolymeren met polyisopreen (PI) en de bulk thermische eigenschappen van deze polymeren worden besproken in *Hoofdstuk* 3. Amorf PFS werd verkregen door copolymerisatie van kleine hoeveelheden van asymmetrisch gesubstituteerd ethylmethyl[1]silaferrocenophane monomeer (EM) met dimethyl[1]silaferrocenophane (DM). De bijbehorende, PI-*b*-PFS blok copolymeren vertoonden geen tekenen van kristallisatie binnen de gehanteerde tijdsperioden. Tijdrovende annealing om thermodynamisch evenwicht te krijgen is overbodig, wat deze blok copolymeren aantrekkelijk maakt voor de beoogde dunne laag toepassingen. Een belangrijke thermische overgang in blok copolymeren voor het bepalen van de annealing strategie is die tussen een geordende en een ongeordende morfologie. Deze overgang is voor de gemaakte polymeren bepaald en bleek afhankelijk te zijn van het gehalte EM dat in het polymeer geïncorporeerd is, waarschijnlijk doordat het EM een iets meer alifatisch karakter van de PFS fase creëert.

De morfologie in dunne lagen van deze polymeren wordt in *Hoofdstuk* 4 besproken. De amorfe copolymeren vertonen een ordening die op vlakke substraten over meer dan 1 micron reikt, wat uitzonderlijk hoog is voor blok copolymeren, die gewoonlijk slechts over een paar honderd nanometer coherente orde vertonen. In dunne lagen met een dikte van slechts één laag van fasegescheiden domeinen zijn de bollen hexagonaal georganiseerd. Door middel van een studie met dynamische ionmassaspectrometrie is een overgang in de structuur van deze hexagonale pakking naar een BCC morfologie aangetoond als functie van de laagdikte, waarbij in de BCC structuur het 110 vlak zich parallel ten opzichte van het substraat bevindt. Deze BCC structuur was in de gehele laag aanwezig. Beide blokken van PI-*b*-PFS zijn op het substraat aangetoond, in tegenstelling tot PS-*b*-PFS, waar PFS het substraat bevochtigde. De substraatbevochtiging door PI-*b*-PFS en PS-*b*-PFS verschilt dus kwalitatief, waardoor het vergelijken van graphoepitaxiale ordening (ordening geïnduceerd door een topologische structuur) van de fasegescheiden domeinen interessant werd, aangezien de sturende werking in graphoepitaxie tot dusverre toegeschreven werd aan de aanwezigheid van een moleculaire laag van slechts één van de blokken op het substraat. Een graphoepitaxiale studie

van PI-*b*-PFS wordt daarom in *Hoofdstuk* 5 gepresenteerd. In groeven met een diepte van één monolaag van domeinen werd de positie van de blok copolymeer domeinen langs de groefwand gedicteerd, ondanks de neutrale bevochtigingsvoorwaarde. Succesvolle positionering van de domeinen op grotere afstand van de groefwand werd in lineaire en hexagonale groeven met breedtes tot 1.3 μm gevonden. De hexagonale groeven vertonen 2D organisatie van domeinen. In circulaire groeven kwam graphoepitaxiale ordening niet voor. De gebogen zijwanden veroorzaakten direct naast de groefwanden een druk op het copolymeer die geabsorbeerd werd door uitrekking of compressie van de domeinen zelf en door aanpassing van de afstanden tussen de domeinen.

In *Hoofdstuk* 6 wordt de synthese, karakterisatie en dunne laag morfologie van een PFS bevattend blok copolymeer gegeven, met als doel polymeer-substraat interacties in het geval van andere chemische samenstellingen te bestuderen. PFS-*b*-polylactide (PLA) werd gesynthetiseerd door gebruik te maken van zowel anionische als gekatalyseerde ring-openings polymerisatie-technieken. Het PLA blok vormde een beduidend polairder blok dan de tot dusver gebruikte blokken, wat sterkere substraat-polymeer interacties tot gevolg had. In extreem dunne lagen (< 10 nm) resulteerde deze substraatinteractie in geaggregeerde PFS structuren op een aan het substraat geabsorbeerde PLA laag. Dit copolymeer, het eerste voorbeeld van een blok copolymeer met een organometaal blok en een biodegradeerbaar blok, maakt gemakkelijke fabricage van twee verschillende types structuren mogelijk, die beide als een sjabloon voor een platform bestaande uit functionele nanodomeinen kunnen dienen. Het gebruik van PLA maakt tevens toepassing van milde etstechnieken, zoals hydrolyse, mogelijk. De gesynthetiseerde blok copolymeren waren grotendeels amorf, met een overgang van geordende structuren naar een ongeordende smelt rond 135 °C. Bij hogere temperaturen werden ketenbreuk en transesterficatieprocessen belangrijker in het PLA blok, wat de dunne laag morfologie beïnvloedde.

In *Hoofdstuk* 7 wordt het gebruik van PFS bevattende blok copolymeren in een katalytische toepassing verkend. De vorming van carbon nanotubes (CNTs, 'koolstof nanobuisjes') met gecontroleerde diameters, waarbij gebruik gemaakt werd van een katalytisch platform gebaseerd op PS-*b*-PFS, wordt besproken. Meerwandige carbon nanotubes zijn gemaakt met een nauwe verdeling in diameters. De diameters konden beïnvloed worden door de molaire massa van de precursor blok copolymeren aan te passen en een acetyleen/ waterstof gasmengsel te gebruiken in een chemisch gasfase depositieproces. De grootte van de CNT diameters nam af in het geval van kleiner wordende precursordomeinen.

Tot slot worden in *Hoofdstuk* 8 als vooruitblik voorlopige resultaten met betrekking tot amine-functionalisering van PFS gegeven. De beschreven functionalizering maakt routes naar specifieke chemische eindfunctionaliteit van PFS of overige organische blokken mogelijk, maar ook functionalisering tussen twee blokken met als doel de fasescheiding tussen twee blokken te versterken.

Acknowledgements

Man reist nicht um anzukommen, sondern um zu reisen.

Johann Wolfgang von Goethe

When I first came to Twente I had little idea I would be melancholic to leave after a bit more than four years, but so it is. The thesis is done, finally, and I owe many people my gratitude for their help in accomplishing this. I'd like to thank some of them especially.

First, I'd like to thank Julius Vancso for the opportunity to join his group. I truly appreciate the chances you gave me to develop myself professionally, and consequently personally. It has been in many ways a most valuable experience. The scientific discussions we had, especially in the last year, were very inspirative and I enjoyed these conversations a lot. As you are well aware, I have always felt 'at home' in MTP. Thank you for creating this environment!

Mijn oprechte dank gaat uit naar Mark Hempenius, mijn dagelijkse begeleider in MTP. Ik heb veel steun aan je gehad bij het onderzoek en bij het schrijven. Je hebt zeker engelengeduld met mij gehad! Het was daarnaast altijd erg gezellig om wat te kletsen, of om verhaal te houden, wat ik dan ook volop gedaan heb. Met name de laatste maanden heb ik geloof ik de deur van je kantoor platgelopen (vandaar de losse deurkruk?), erg fijn dat dat kon! Ik vond het erg leerzaam en plezierig samenwerken!

I worked together with three master students, and parts of their work is included in this thesis. Joris, Qi en Thomas, thanks for your dedication! I hope you liked getting bossed around by me as much as I did doing so! I enjoyed working together!

Clemens, dankje voor al je hulp met (niet werkende) apparatuur (waaronder met name de zelf-denkende computers)! Jouw hulp was onmisbaar!

Genevieve en Cindy, ook bedankt voor de ondersteuning en de gezellige 5 minuten-gesprekjes.

I would like to express my gratitude to many persons who helped me with experimental work: Zlata (chemical lab), Mark Smithers (SEM), Joy Cheng (Massachusetts Institute for Technology, graphoepitaxy), Rachel Segalman, (Berkely, Voronoi script), Anja van Langen, DIMES Delft (E-Beam), Arthur Woll (Cornell High Energy Synchrotron Source, SAXS), Ullrich Gunst (University of Münster, TOF-SIMS) and the clean room staff.

Most important for my time in Twente were the people from MTP, who, although the members have changed completely during my stay in the group, have always made MTP like a home to me, and who made it so worthwhile to come to work everyday (and night): Douwe Wiebe, Atilla, Barbara, Igor, Nikodem, Ewa, Beáta, Nina, Shan, Chuangliang, Sasha, Steffi, Henrik (my faithful correspondent from Vàsteras), Sandra (my faithful correspondent from La Coruna, although sometimes in Spanish), Monika, Szczepan, Iwan, Ramon, Dorota, Shuying WHO, Marina, Qi, Yujie, Jing, In Yee, Edi, Eugenia, Anika, Joost, Cynthia, fantastic Dennis, singing Oya, Weiging, Janet, Thomas, Johannes, Joris, Melba, Carlos, Holger, Emilia, and (perfect neighbor) Maria. My apologies to everyone I forgot here. I have many great memories of things we did together, besides working... Many persons of you joined the 'very-Dutch wadloop-expedition' across the Waddenzee, and I'm proud on the MTP-ers that did this 'once in a lifetime experience' (according to GJV) twice! Other great activities were the camping/hiking trips in the Ardennen, the trips to Mainz, and Bath, and of course Lunteren! I am extremely happy to have made so many friends among my colleagues.

The girls from our girls-only office are all very dear to me: Nina, Ewa and Janet. We had truly 'the best office', this is why everybody came and visited us all the time (and of course for the tea)! Tough-girl Nina, always joking with everybody maar 'met een hartje van goud'. We had so much fun and (almost hysteric) fits of laughter, unforgettable! Great to keep in touch with you! Ewa, we had many pleasant talks over a cup of tea in our office.. It was great to be at your wedding in Poland and see you this happy! Janet, you are a really sweet person, and a lot of fun to be with! I trust, you take care of the crazy guys in MTP, SMCT (and in your neighborhood) and make them behave!
Siggi, you are a very good friend to have, we had a lot of fun doing our girly things, having wild evenings, or just having a cup of tea together! Thanks for always being there! Marina, I enjoyed our small 'big' conversations at work a lot, as well as competing at squash, or dancing out! Thanks very much for

your support especially in the last months, and for going so carefully through my thesis.
All of these girls made sure I was eating properly while writing my thesis (enough vitamins, fibers, salads or turkish food), getting coffee or tea... thanks for all the good cares!

Once in a while some brave men dared entering the girls-office... with these courageous guys I enjoyed hanging out, discussing how they can improve their gallantry towards women... and to compensate the girl-talk. Some of my favorite evenings were spent with both Bas and Thomas during our 'book-club' (I know you 'cool' guys resent this name, but I like it!). Discussing philosophy or books with two handsome men... what else a girl needs?! And, I must add, I am impressed with you guys reading *Persuasion*! I remember with a lot of pleasure the 'road-trip' in Canada at -20 °C and the very adventurous, but dangerous hiking trips in the Letchworth and Ole Bull state parks after the SAXS (with an 'a') measurements. And, of course, tango! Thanks for the good company, Thomas... and keep in touch! Bas, I enjoyed especially 'het spijbelen', and all our nice conversations in between and after work! Eddy, my 3^{rd} paranimf, those were good times, hanging out late at night at the UT (most of the times) or at a bar (occasionally)! A lot of depth, I must say! Thanks, guys!

I would like to thank Beáta (the real 'Vilmos-babe') and Douwe Wiebe especially for all the great time we spent together in Enschede, Hungary, Belgium, France and, again, in The Netherlands. Since I followed your trail all over Europe, I hope you will come and visit me in M.! You are both always very, very welcome!

With many people from other groups (PBM, RBT, STEP, SMCT) I spent great times and they have left me nice memories. With so many people, I will not mention everyone, but to Miguel, Fernando (PARTY!!!), Bart Jan, Ferry, Willeke, Erhan and Henriëtte I want to express a warm 'thanks'! And of course the P-NUTters Alexander, Sebastiaan, Annelous, Eric en Jeroen. I hope P-NUT establishes itself firmly at the UT! Also, most importantly: I would like to thank all the early-morning coffee-makers (mostly Anika and In Yee)! Kees Venner, thanks for the karate-coaching, that comes in very useful in everyday (Ph. D. student) life.

I am very happy to have stayed in touch with Ulli Steiner and with so many of my former 'collegues': Ole, Nico, Mihai, Pieter and Stephan. Ulli, thanks for your comments on my thesis and the discussions about my work. I'm happy to have you on my committee! Ole, since you moved to Twente, we see each other much oftener, and I enjoy our 'small talks' a lot! And thanks very much

for your help at work and especially in my Latex-crisis just before submitting the thesis! Thanks Nico, for the tips on floating films and the good time, when visiting C. I'd like to thank Cynthia, Siggi, Bas and Marina for giving corrections to this thesis, I appreciate your help very much! Thanks to my paranimfen Sandra en Hendrike for always being there for moral support!

Many thanks to my friends from Groningen who stayed in touch: Marleen (SAXS was supergezellig!), Hendrike, Micha (uren aan de telefoon!), Gerlof (volgend jaar kerstvakantie weer een date?!), Guus, Niels, Willem, JP en Kuik, waardoor de zeil-weekenden en *tig*-gangen diners altijd gezellig zijn!

All the persons mentioned here (and many that I could not mention) have contributed to make the time I spent in Enschede an unforgettable experience, which I would not have missed out on!
But most importantly, I owe my family my deepest gratitude for all the support they give me. Boven alles, wil ik mijn familie bedanken. Mijn zussen Sandra en Christine, mijn kleine grote broertje Anton, mijn zwager Remon, mijn allerliefste nichtje Ylse en mijn vader en moeder, Wim en Hilde, bedankt dat jullie altijd voor me klaar staan en zo'n ongekende vertrouwen in mij hebben!

Monique

APPENDIX A

PI-*b*-PFS characteristics

polymer	M_n[a] [kg/mol]	M_w[a] [kg/mol]	M_w/M_n[a]	EM[b] [mol%]	ϕ_{PFS}[b]	Morp.[c]	d[c] [nm]
IF52/20EM7	71.5	74.8	1.05	7.4	22	HEX	35.9
IF55/22EM23	76.3	80.8	1.05	22.7	23	HEX	41.3
IF50/21EM10	70.9	72.6	1.02	9.7	23	HEX	33.8
IF54/18EM6	71.8	74.2	1.03	5.6	19	BCC	31.1
IF58/22	79.8	83.3	1.04	0	22	HEX	38.6
IF57/18	74.8	77.1	1.03	0	18	BCC	31.1
IF35/11EM11	45.1	46.8	1.04	10.9	18	BCC	22.1
IF47/13EM45	60.3	61.5	1.02	44.8	16	BCC	23.9
IF51/17EM100	67.7	72.3	1.07	100	19	BCC	31.2
IF37/13EM100	50.1	51.4	1.03	100	20	BCC	21.3
IF29/11EM10	39.2	42.7	1.09	10.4	21	BCC	21.9
IF24/13EM20	36.4	41.2	1.13	19.7	27	HEX	25.2
IF23/12EM17	35.3	44.0	1.25	16.9	27	HEX	25.9
IF20/10EM20	29.9	37.9	1.24	19.9	27		24.0
IF27/15EM16	42.9	49.0	1.14	15.9	29	HEX	34.5
IF17/9EM28	26.8	30.4	1.13	28.0	28	HEX	18.3
IF30/16EM38	46.0	51.0	1.11	37.5	28		25.5
IF30/15EM26	44.7	50.9	1.14	26.3	20		26.4
IF54/19EM16	72.3	76.7	1.06	16.3	20		48.5
IF58/22EM9	80.2	82.9	1.03	8.7	21	BCC	37.1
IF44/15EM14	58.2	61.2	1.06	14	19	BCC	25.1
IF48/18EM24	66.0	69.3	1.06	24.2	21		32.5
IF51/16EM13	67.1	69.5	1.04	13.1	18	BCC	27.6
IF30/18EM12	48.0	49.8	1.04	12.2	31		26.9
IF21/12EM15	32.9	38.8	1.18	15.4	30		22.4
IF59/19EM30	77.8	80.6	1.04	30.0	19	BCC	33.8
IF37/12EM26	48.7	50.4	1.04	25.9	19	BCC	22.5
IF34/12EM52	45.5	51.7	1.14	52.1	19	BCC	23.5
IF64/18EM30	82.0	105.1	1.28	30.3	17	BCC	36.9
IF33/11	44.6	50.5	1.13	0	20	BCC	22.1

[a]Measured by GPC in THF, relative to polystyrene standards. [b]Calculated from ^{1}H NMR. [c]Measured by SAXS.

APPENDIX B

Image analysis

The procedure employed to construct Voronoi diagrams or pair-distribution functions from experimental images, obtained from for example AFM or SEM, is as follows.

The images were filtered to reduce noise, by using an optical transfer function and filter in the desired fast fourier transform range. From the filtered image, the domains were recognized by offsetting the pixel brightness. To each recognized domain a x- en y-coordinate was attributed. The coordinates were used for calculating the Voronoi diagrams and the pair distribution function. In the following sections, the procedures are briefly explained and the MATLAB sequencing used is given.

B.1 Filtering

The image is loaded and the edges of the image are smoothed. A fast 2D fourier transform (FFT) is performed (Figure B.1) and the optical result is shown in Figure B.2 (left).

The 2D FFT is used in conjunction with an optical transform function (OTF) (Figure B.2, right). The width and center of the frequency band is defined with the parameters 'sigma2' and 'rho max', respectively. The band is optically fitted to cover the (first) ring in the FFT. The OTF is superimposed on the FFT and the values under the band are used for the inverse FFT transform, which gives the filtered image. The MATLAB sequence is shown in Figure B.3, and the resulting filtered image is shown in Figure B.4.

The pixels are screened for the brightest pixel with respect to the 4 or 8 neighboring pixels (we used 8 for the sharpest result). When the OTF was

```
close all   % close all figure windows
clear all   % clear all variables

afm = double(imread(afm_file','tif'));   % read the image and convert it to double
figure(1);
imshow(afm,[]);
title('original');

%--------------- filter the image  ---------------------------------

% window the image to make it smooth near the edges:
r = 0.1;                                % relative distance from the edge
sz = size(afm);                         % size of image
w = tukeywin(sz(1),r);                  % create a tukey window (line)
w_hor= w*ones(1,sz(2));                 % horizontally
afm = afm.*w_hor;                       % window the image
w = tukeywin(sz(2),0.1);                % create a tukey window (line)
w_ver= ones(sz(1),1)*w';                % vertically
afm = afm.*w_ver;                       % window the image
imshow(afm,[]);                         % show it

Fafm = fft2(afm);                       % perform 2D fourier transform
figure(2);
imshow(log(abs(fftshift(Fafm))+1e+3),[]);   % show the amplitudespectrum (logarithmic)
title('Fourier tranform of input image');
```

Figure B.1: MATLAB operation sequence for the 2D fourier transform.

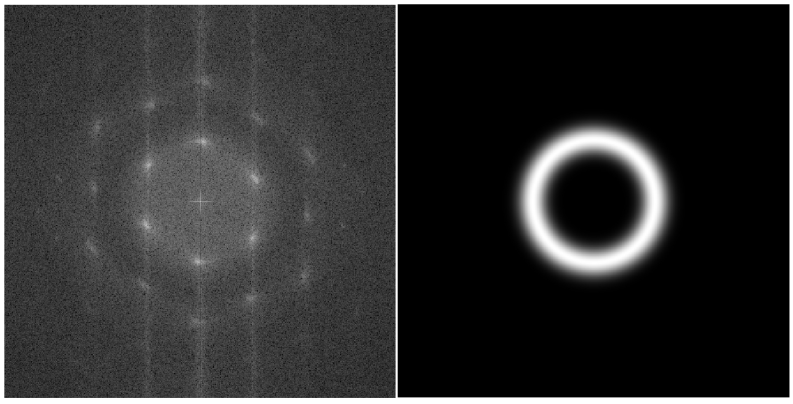

Figure B.2: The 2D Fourier Transform (left), and the corresponding *optical transfer function* (right).

well-chosen, and the filtered image gave a satisfying result, each brightest pixel out of 8 corresponded to a domain and was awarded with x- and y-coordinates (See Figure B.5). To each pair of (x,y) coordinates a red dot was awarded (see Figure B.9), and the set of dots was superimposed on the original image for a visual screening of the match.

```
% create a rotationally symmetric transfer function
sigma2 = 150;                    % width of frequency band squared
rho_max = 80;                    % centre of frequency band

H=zeros(sz(1),sz(2));
for u= 1-sz(1)/2 : sz(1)/2
   n = mod(u,sz(1))+1;
   v = -sz(2)/2 : sz(2)/2-1;
   rho = (u.^2+v.^2).^0.5;
   H(n,:) = fftshift(exp(-0.5*(rho-rho_max).^2/sigma2));
end
figure(3);
imshow(fftshift(H),[]);
title('Optical transfer function');

% filtering in the Fourier domain
Fafm_filtered = H.*Fafm;

% inverse transform
afm_filt=real(ifft2(Fafm_filtered));
figure(4);
imshow(afm_filt,[]);
title('filtered image');
```

Figure B.3: MATLAB operation for filtering in the 2D FFT regime, using an optical transfer function.

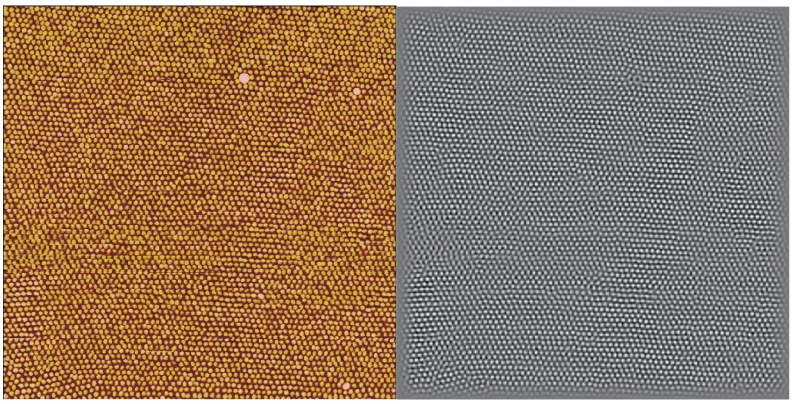

Figure B.4: The original image (see 4.3) (left), and the filtered image (right).

B.2 Voronoi diagrams

The MATLAB sequence used to calculate the Voronoi diagrams, using the set of (x,y) coordinates obtained from the filtered image, is shown in Figure B.6. Colors are awarded to the polyhedrons, depending on the number of neighbors. The result was either superimposed on the original image, or plotted separately, with colored polyhedrons denoting the number of neighbors.

```
%---------- finding the local maxima ----------

afmmax = imregionalmax(afm_filt,8);        % use second parameter for sharper result
figure(5);
title('local maxima');
imshow(afmmax,[]);
[y,x] = find(afmmax);
figure(1); hold on;
plot(x,y,'r.');

%-------------------------make a two column data set 'data' from afmmax---------

[i,j]=find(afmmax);
data=[j,i];
data=[x,y];
```

Figure B.5: MATLAB operation sequence for finding the local maxima, using the filtered image.

(Examples can be found in Chapter 4.)

```
%this draws a voronoi diagram of a 2 column data set called 'data' in the workspace
%it will create a 8 column vector called 'sides' where sides(1)-sides(8) contains the number
%of voronoi cells with that many sides.

figure(7)
[V,C] = voronoin(data);
X = data(:,1);
Y = data(:,2);
w=1.5;
x1=w/-0.003;
count=0;
clear sides
for n=1:8
   sides(n)=0;
end

voronoi(X,Y);
h=voronoi(X,Y);
set(h,'MarkerSize',.1,'MarkerFaceColor', 'black')

for i = 1:length(data)
   if ((X(i)>x1) & (X(i)<(w-x1)) & (Y(i)>x1) & (Y(i)<(w-x1)))
      count=count+1;
      F = C{i,:};
      if length(F) == 6
         patch('Vertices',V,'Faces',F,'FaceColor','w','MarkerSize',.2,'MarkerFaceColor', 'black')
         sides(6)=sides(6)+1;
      elseif length(F) ==5
         patch('Vertices',V,'Faces',F,'FaceColor',[1,0,1],'MarkerSize',.2,'MarkerFaceColor',
'black')
         sides(5)=sides(5)+1;
      elseif length(F) == 7
         patch('Vertices',V,'Faces',F,'FaceColor','blue','MarkerSize',.2,'MarkerFaceColor',
'black')
         sides(7)=sides(7)+1;
      elseif length(F) == 4
         patch('Vertices',V,'Faces',F,'FaceColor','y','MarkerSize',.2,'MarkerFaceColor', 'black')
         sides(4)=sides(4)+1;
      elseif length(F) == 8
         patch('Vertices',V,'Faces',F,'FaceColor','green','MarkerSize',.2,'MarkerFaceColor',
'black')
         sides(8)=sides(8)+1;
      end
   end
end

%------------------plot empty voronoi diagram on original image----------------------------------------
%figure(1); hold on;
%voronoi(X,Y);
%h=voronoi(X,Y);
%set(h,'MarkerSize',.1,'MarkerFaceColor', 'black')
```

Figure B.6: MATLAB operation sequence to calculate the Voronoi diagrams, using the data set of local maxima obtained previously.

B.3 Pair distribution function

For a detailed description on how to compute the pair-distribution function (PDF) $g(r)$, see Allen and Thomas.[52] We used the MATLAB sequence given in Figure B.7 and Figure B.8. First we define a box in the image. The function $g(r)$ is to be computed for all domains that are located within the box. This is done by determining all the distances from every single domain in the box to all other domains. The distances are sorted, after which a value for $d(r)$ is chosen. The number of distances that are located within each $d(r)$ is given as a function of r, which results in the function $g(r)$. The parameters influencing the roughness of $g(r)$ are z, which determines the size of the box and therefore the number of domains over which $g(r)$ is averaged, and the size of $d(r)$.

Figure B.9 shows the original image in gray scale. The domains are marked by red dots, obtained through the filtering procedure. In the center of the image, green marks denote the box. The domains within the box marked with blue dots were used for the PDF, which is shown in Chapter 4

```
%------------------find center image and define box-------------------------
mid=sz.*0.5
z=20;
X1=mid(:,1)-z;
X2=mid(:,2)+z;
Y1=mid(:,1)-z;
Y2=mid(:,2)+z;

%show points in image
figure(1);, hold on;
plot(X1,Y1,'g+');
plot(X1,Y2,'g+');
plot(X2,Y1,'g+');
plot(X2,Y2,'g+');

m=0;

%-------data points within box are kept, others empty---------------%
for i=1:length(data)
   if ((data(i,1) > X1) & (data(i,1) < X2) & (data(i,2) > Y1) & (data(i,2)<Y2))
      box(i,1)=data(i,1);
      box(i,2)=data(i,2);
   else box(i,1)=0;
      box(i,2)=0;
   end
end
%empty entrees are removed from data set, the coordinates of the
%domains within the box remain: a two-column data set called 'box2'

for j=1:length(box)
     if box(j,1)==0
     B2(j,1)=box(j,1);
     B2(j,2)=box(j,2);
     else
     m=m+1;
     box2(m,1)=box(j,1);
     box2(m,2)=box(j,2);
  end
end

figure(1); hold on;
plot(box2(:,1),box2(:,2),'b.');

%For all values from data: find the corresponding row numbers of the points in the defined
%box
for i=1:length(data)
   if ((data(i,1) > X1) & (data(i,1) < X2) & (data(i,2) > Y1) & (data(i,2)<Y2))
      k(i,:)=i;
   end
end

%Calculate the mutual distances and show in a matrix
C=pdist(data);
Distdata=squareform(C);
```

Figure B.7: MATLAB operation sequence for the definition of a box of particles in the middle. For each data point in this box, the distances to all other data points are calculated.

```
%-----------------------calculate 2R0 within box, called Ro2---------------------------

Distbox=sort(squareform(pdist(box2))); % geeft de onderlinge afstanden binnen de box
min_rij=Distbox(2,:); %1e rij altijd zeros (afstand tot eigen deeltje)
Rbox=min(min_rij)*0.5 % berekend minimale afstand (=2R0) voor deeltjes in box

%----------calculate particle density--------------

densbox=length(box2)/((X2-X1)*(Y2-Y1))  %density from box

%-----------------count no. Of distances for each dr

dr=0.001*(max(kolom)-min(kolom))
r=min(kolom):dr:max(kolom);
szr=size(r);
a=zeros(szr(2),1);


for i=1:length(kolom)
      for j=2:szr(2)
      if ((kolom(i) >= r(j-1)) & (kolom(i) <= r(j)))
         a(j)=a(j)+1;
      else a(j)=a(j);
      end
   end
end

actual_size=1000;              % input the size of the image in nm
pixel_size=1000/sz(1);
actual_distance=Rbox*pixel_size

%---PDF: calculate  y=g(r) and x=r---------------------------------
k=0;
for j=2:szr(2)
   k=k+1 ;
   g(k,1)=(((0.5*(r(j)^2-r(j-1)^2))/dr)/Rbox)*actual_distance;
   g(k,2)=(a(j)/(length(box2)))/(densbox*2*pi*0.5*(r(j)^2-r(j-1)^2));
end

figure(9);
plot(g(:,1),g(:,2))
```

Figure B.8: MATLAB operation sequence for the calculation of the pair-distribution function (PDF) for each data point in the box. The PDF's of the data points in the box are averaged for statistical evaluation.

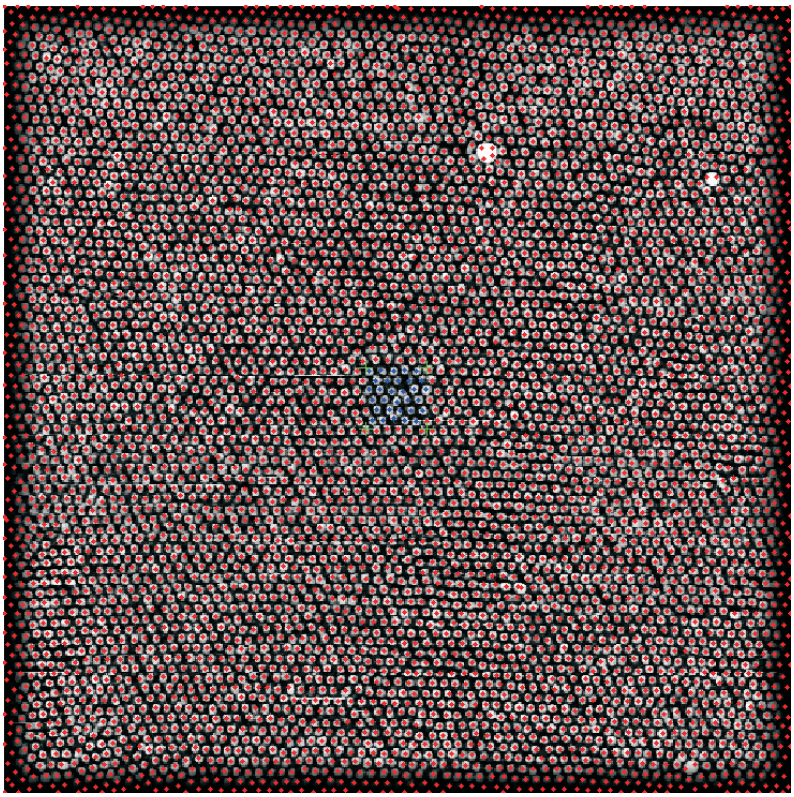

Figure B.9: The original image with the block copolymer domains marked (red dots). In the center, a square marked by green brackets denotes the box. The particles in the box (blue dots) are used for the calculation of the PDF. See also Figure C.13.

APPENDIX C

Color Figures

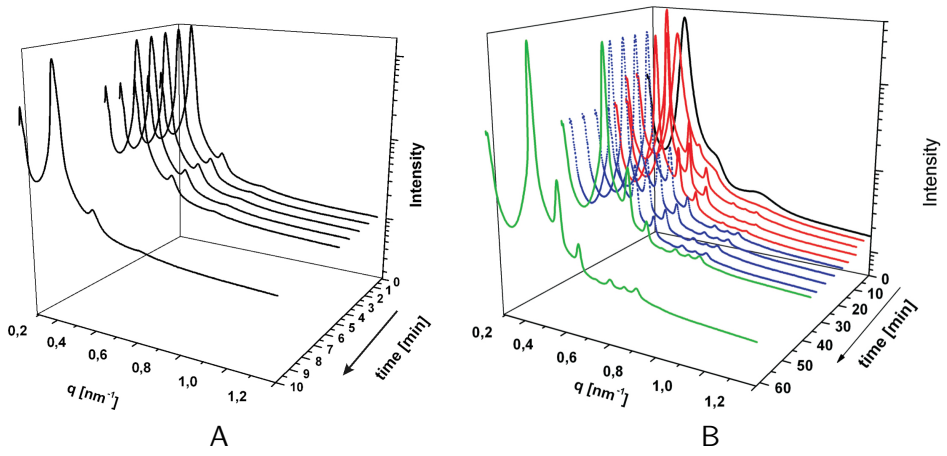

Figure C.1: Time-resolved SAXS patterns of IF30/15EM38 at 200 °C (A) and time-resolved SAXS patterns of IF34/11EM52 in an annealing cycle: unannealed (black, solid line), 130 °C (red, solid lines), cooling down to 60 °C in 3.5 min (blue, dotted lines) and room temperature (green, solid lines)(B).

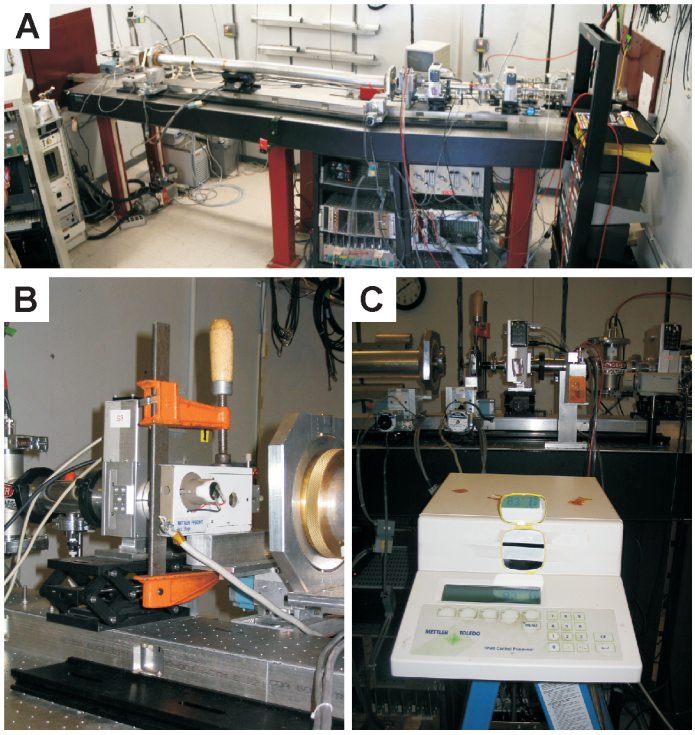

Figure C.2: G1 Line at the Cornell High Energy Synchrotron Source, used for SAXS measurements. A) Table setup. B,C) The hot stage setup used for temperature-dependent measurements.

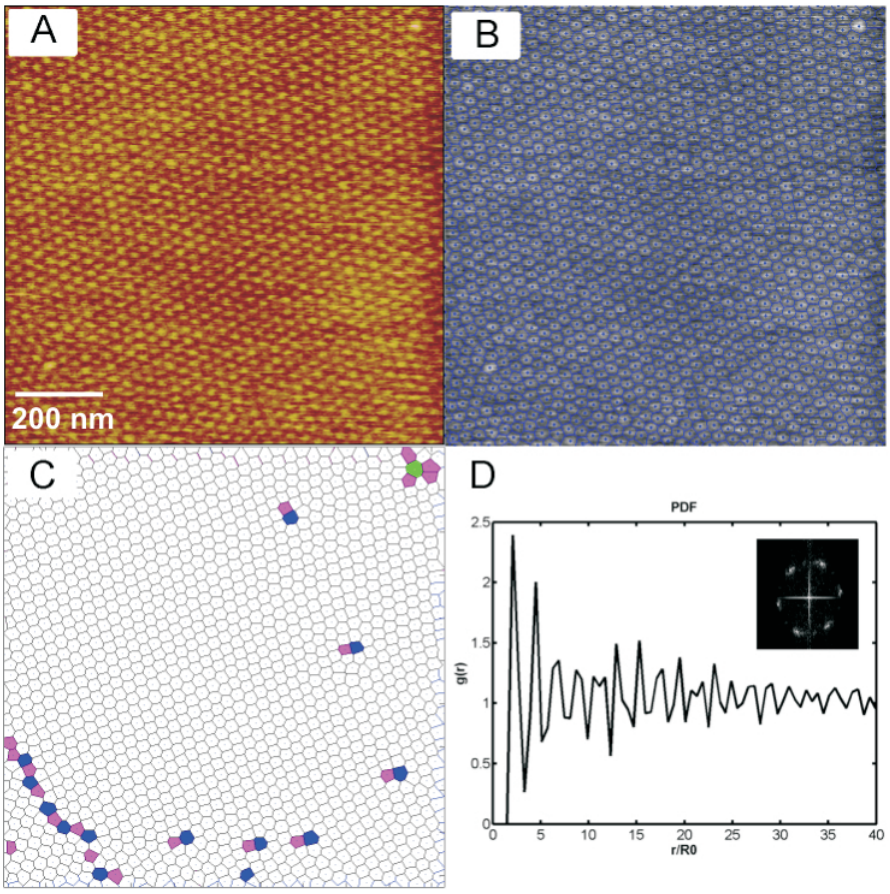

Figure C.3: AFM-TM height image (z-range is 10 nm) of a 35 nm film of PI-*b*-PFS (A). A sphere-finding algorithm was used to construct a representation with Voronoi diagrams (B,C) and a pair-distribution function (D).

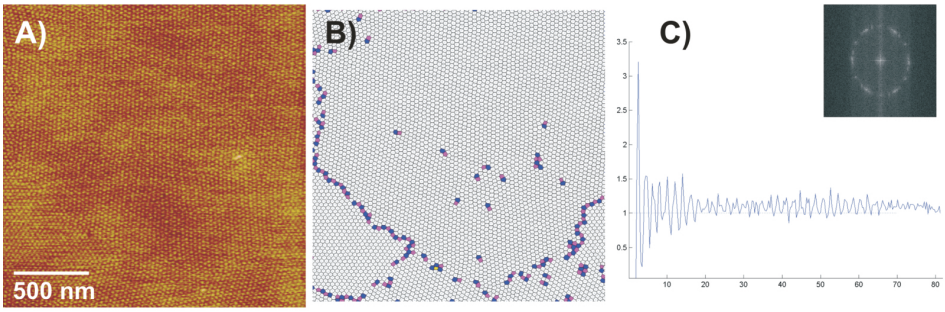

Figure C.4: A) AFM-TM height image (z-range is 10 nm) of a PI-*b*-PFS film (thickness 35 nm), its Voronoi representation (B) and pair-distribution function, with the FFT shown in the inset (C). The film was annealed overnight at room temperature.

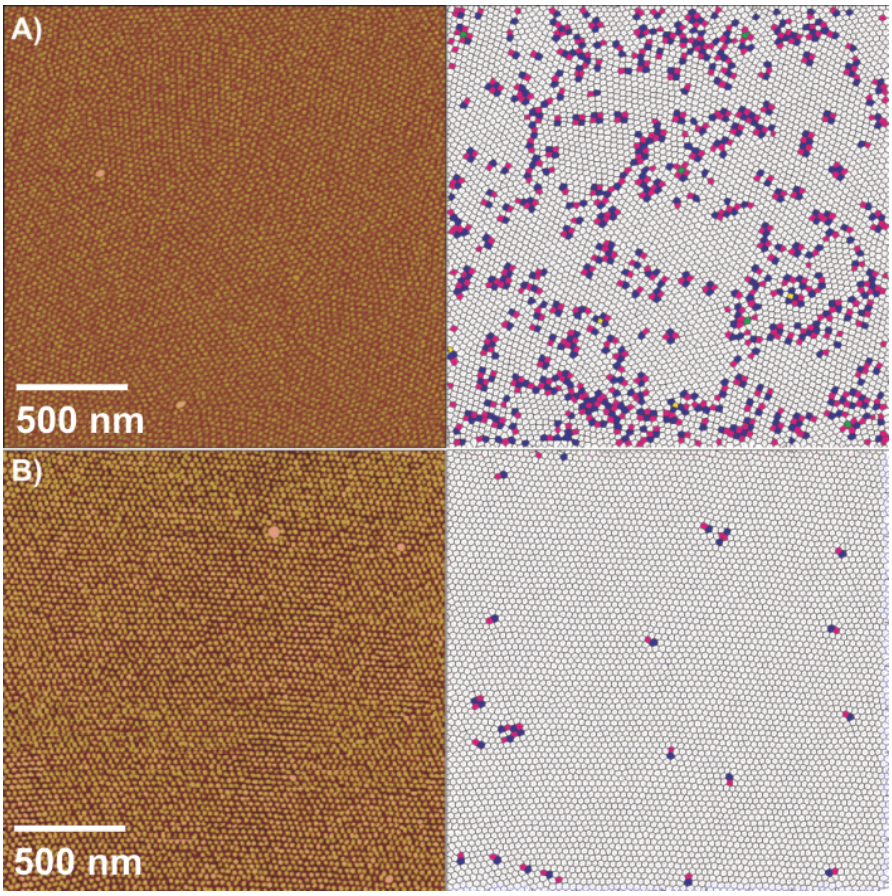

Figure C.5: AFM-TM height image (z-range is 10 nm) of a thin film of PI-*b*-PFS after O_2-RIE exposure and their Voronoi diagram representations, annealed for 5 hours (A), and annealed for 24 hours (B).

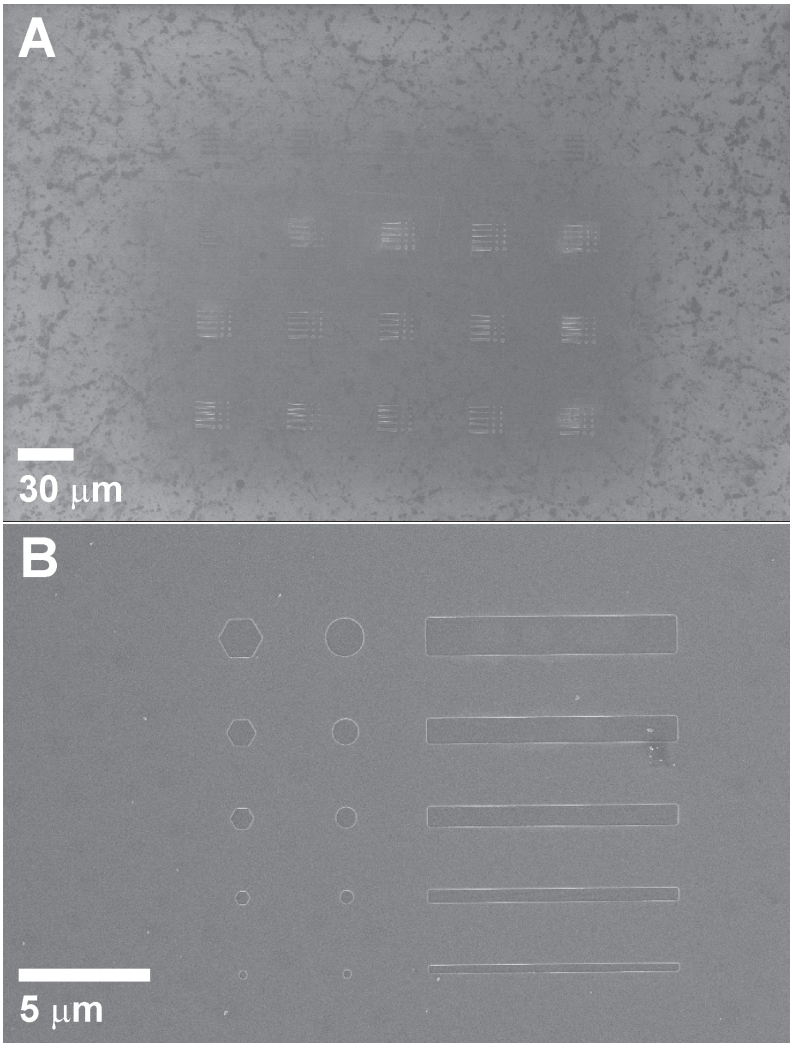

Figure C.6: Typical substrate patterned by E-beam lithography. A pattern (right image) consisting of circles, hexagons and lines with different dimensions is written 10 or more times (left image) on a resistive resin layer and subsequently developed and etched into a silicon wafer. The groove widths are typically around 300 nm, 500 nm, 800 nm, 1 μm and 1.5 μm.

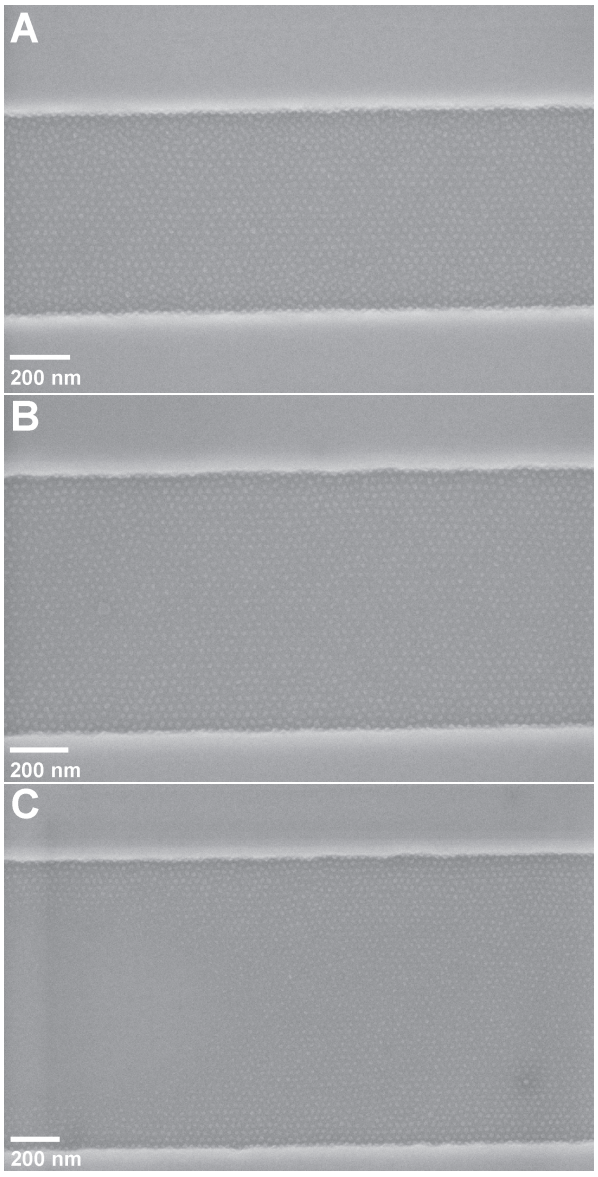

Figure C.7: SEM images of PI-*b*-PFS block copolymer in linear grooves of 800 nm (top), 1 μm (middle) and 1.3 μm (bottom) width. The films were exposed to an O_2-RIE plasma before imaging.

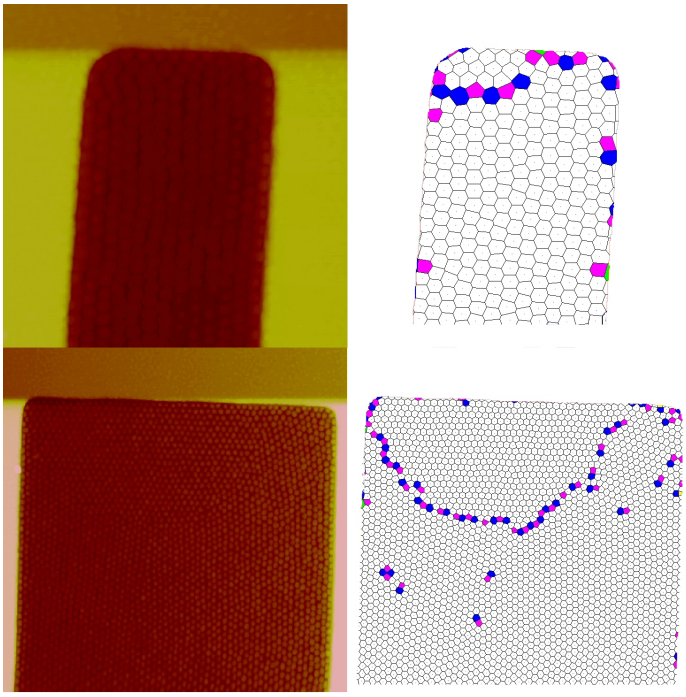

Figure C.8: TM-AFM height images (z-range is 20 nm) of the alignment of PFS domains in square corners of grooves with widths of 300 nm and 1.3 μm. The films were exposed to an O_2-RIE plasma before imaging. The corresponding Voronoi representations are shown at the right.

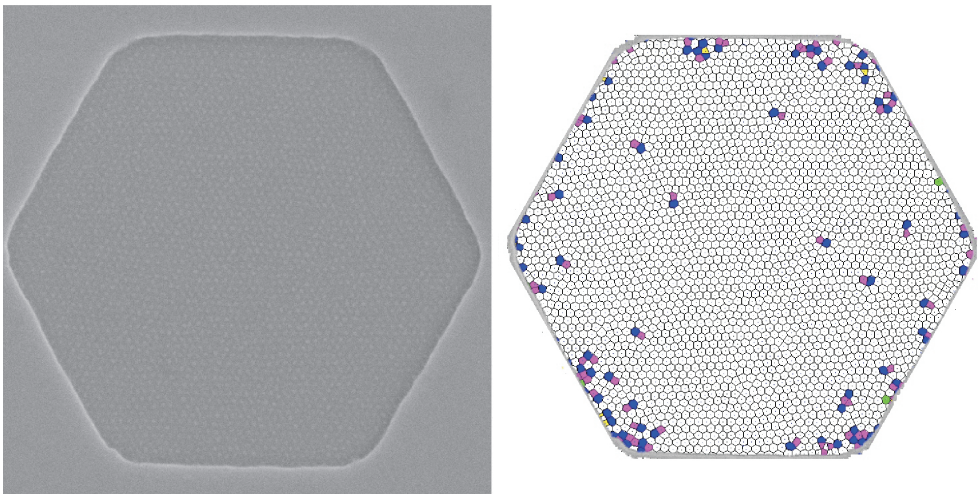

Figure C.9: SEM image of PI-*b*-PFS block copolymer in a 1.3 μm wide hexagonal groove, and a Voronoi representation of the domains. The film was exposed to an O_2-RIE plasma before imaging.

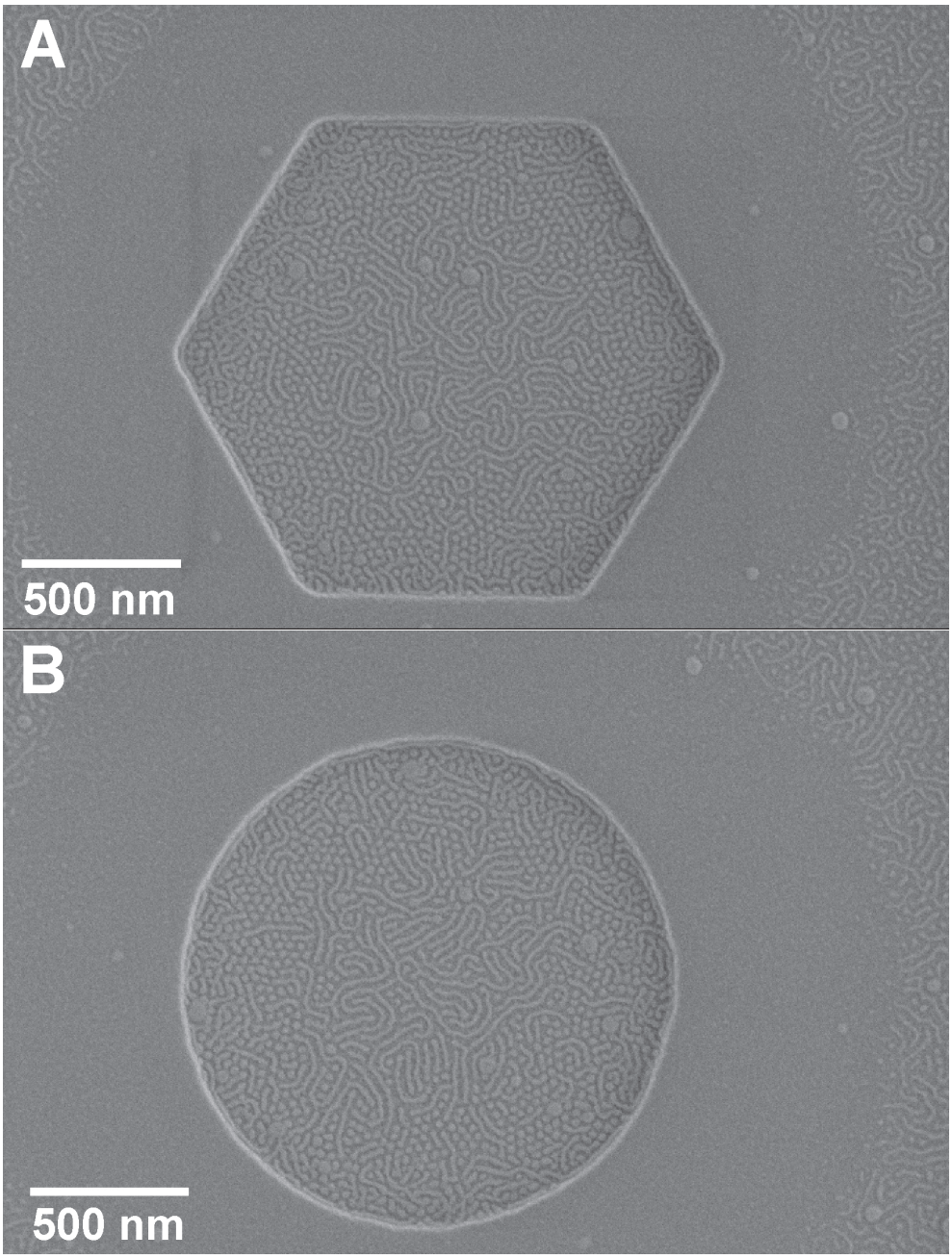

Figure C.10: SEM images of PI-*b*-PFS block copolymer in hexagonal and circular pits on silica substrates. The films were exposed to an O_2-RIE plasma before imaging.

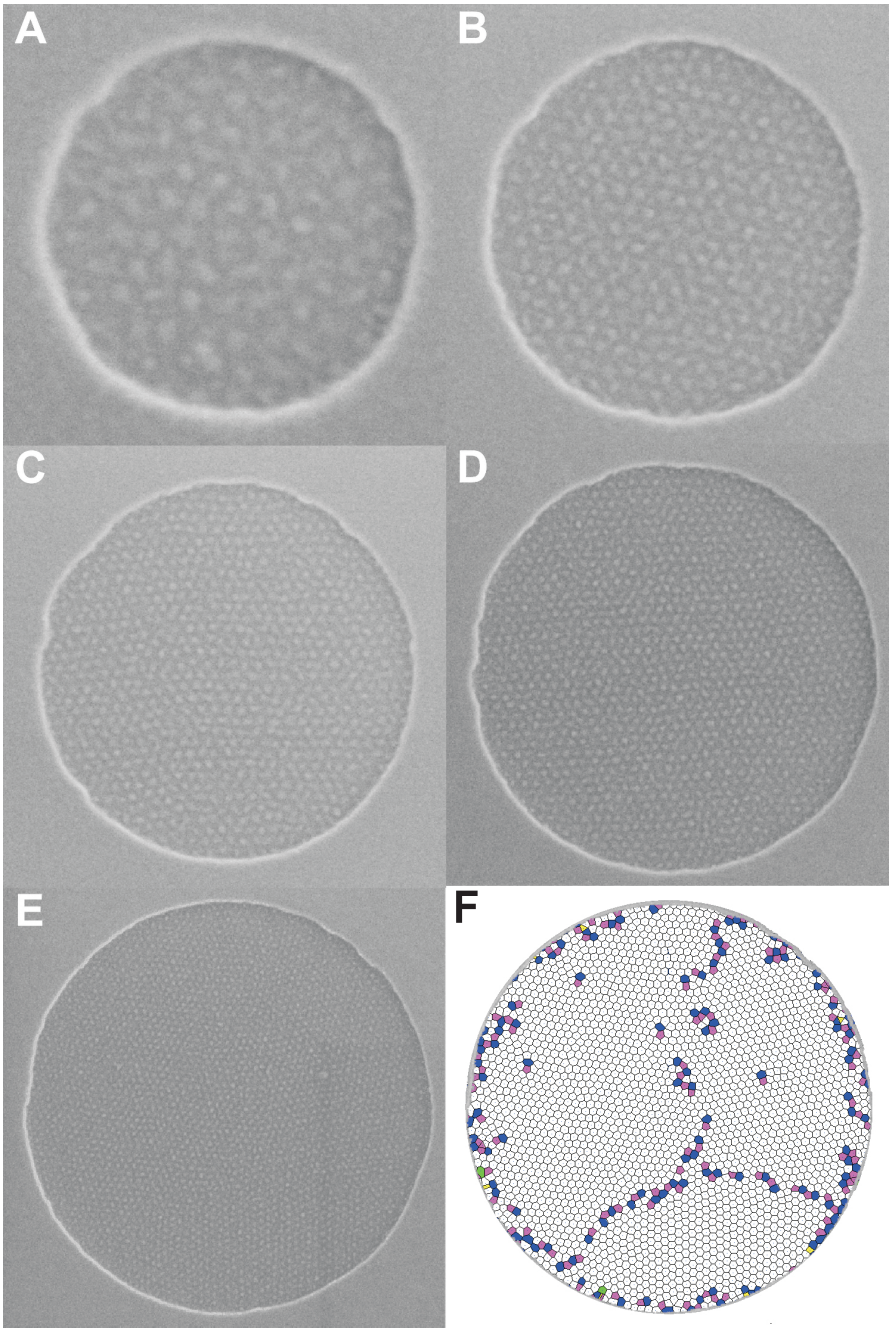

Figure C.11: Series of circular pits with diameters of A) 300 nm, B) 500 nm, C) 800 nm, D), 1 μm and E) 1.3 μm and its Voronoi representation (F). The films were exposed to an O_2-RIE plasma before imaging.

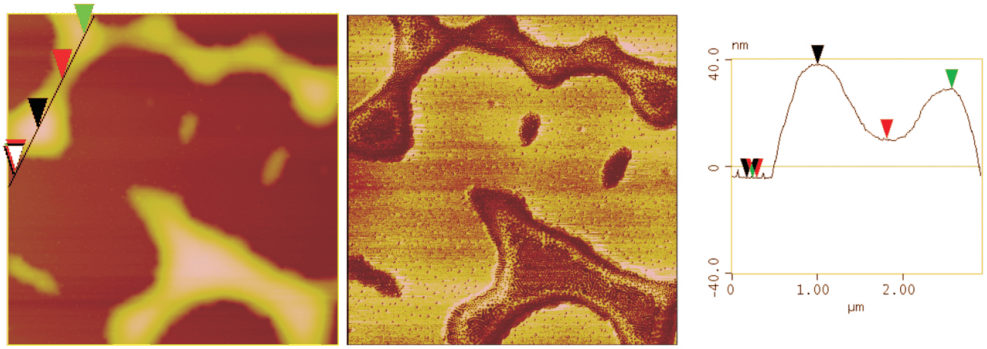

Figure C.12: AFM-TM height (z-range is 80 nm) and phase (z-range is 10°) images of a dewetted FL8/34 thin film on mica, showing step heights of 14.7 nm (red), 33.3 nm (green), and 42.3 nm (black).

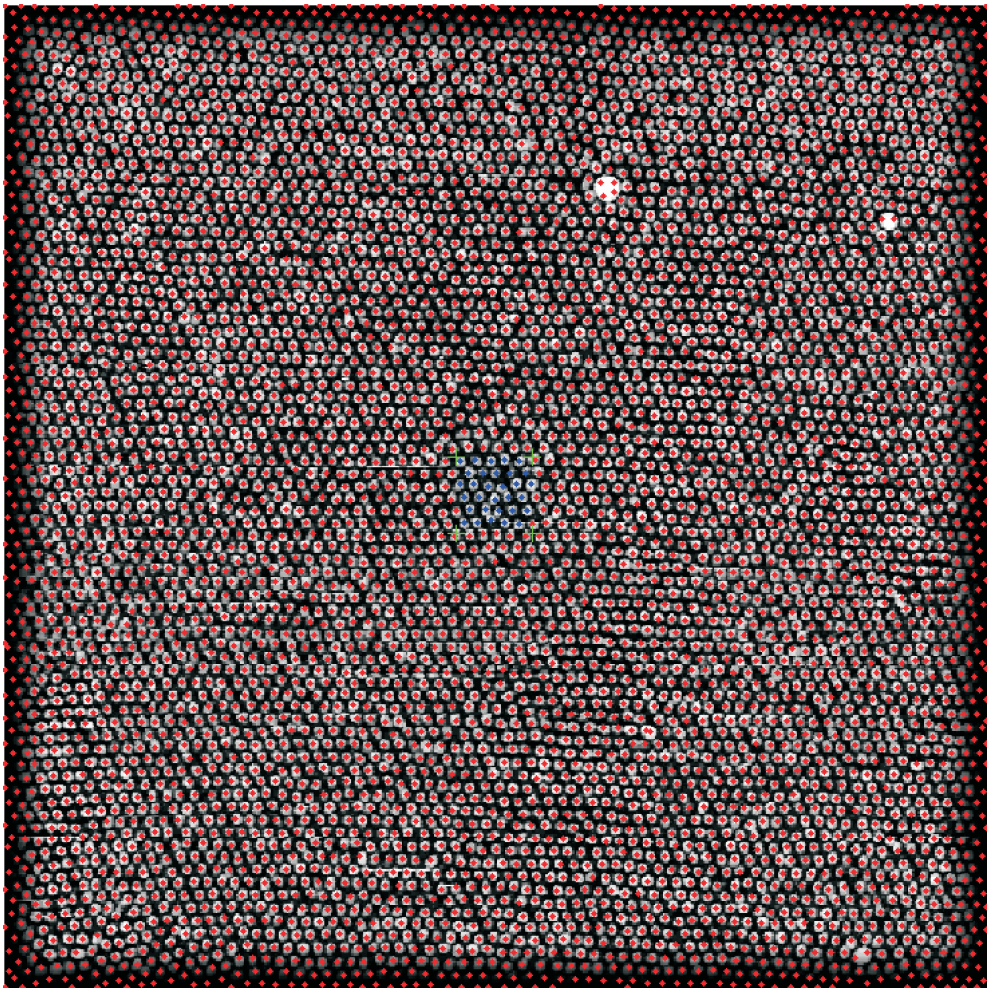

Figure C.13: The original image with the block copolymer domains marked (red dots). In the center, a square marked by green brackets denotes the box. The particles in the box (blue dots) are used for the calculation of the PDF.

Biography

Monique Roerdink was born on 19 September 1979 in Groningen, The Netherlands. After graduating from secondary school (Comenius College, Leeuwarden), she continued her studies at the University of Groningen. She studied chemistry, with a major in polymer chemistry. The master research was performed in the group of Professor Ullrich Steiner, on thermal instabilities of thin polymer films. As a part of her study, she spent three months in the group of Professor Thomas P. Russell at the University of Massachusetts, Amherst (US). After graduating in 2002, she started pursuing a Ph.D. degree in the group of Professor G. Julius Vancso at the University of Twente, which resulted in this dissertation. During her Ph. D. research, she twice visited the Cornell High Energy Synchrotron Source at Cornell University, Ithaca N.Y. (US), where she performed small-angle X-ray studies on block copolymers. She joins the group of Prof. Marc Hillmyer at the University of Minnesota, Minneapolis (US) as a postdoctoral researcher, starting from May 2007.